ABSTRACT

Title of Thesis: COMPUTATIONAL FLUID DYNAMICS SIMULATIONS OF AN IN-LINE SLOT AND TOOTH ROTOR-STATOR MIXER

Author: Derrick I. Ko
Master of Science, 2013

Directed by: Professor Richard V. Calabrese
Department of Chemical and Biomolecular Engineering

Unlike conventional stirred tanks, rotor-stator mixers provide high deformation rates to a relatively limited volume, resulting in a region in which intensive mixing, milling, and/or dispersion operations can occur. FLUENT was used to conduct three-dimensional CFD simulations of the IKA prototype mixer, an in-line slot and tooth rotor-stator device, for a low-speed low-flow condition and a high-speed high-flow condition. The working fluid was water. Turbulence was modelled with the RANS equations, realizable k-ε turbulence model, and non-equilibrium wall functions. The main objective of this project was to develop an enhanced CFD model of the IKA prototype mixer with the necessary refinement in the shear gap to accurately resolve these high shear values.

The grid independence study showed that the required mesh depended on the operating scenario. For the low operating scenario (N = 300 rpm and Q = 0.315 L/s), grid independence was demonstrated for the 10 million cell mesh (with 20 cells across the shear gap). With this mesh, flow field convergence in the shear gap only is reached with about 12 revolutions of the rotor. About 20 revolutions would be needed to also reach convergence in the stator slots. It was demonstrated that the convergence of flow in the

larger, more open stator slots was slower than in the highly-confined shear gap regions, thus accounting for the need for additional revolutions to reach convergence in the stator slots. For the high operating scenario (N = 1800 rpm and Q = 2.54 L/s), grid independence was not demonstrated at the most refined mesh tested (24 cells across the shear gap and 24 million cells overall). The model could not be further refined due to limits in the available computational resources. Flow field convergence in the shear gap requires about 16 revolutions, while convergence of the flow in the stator slots requires about 24 revolutions. A higher number of revolutions are required for the high operating scenario because of the greater intensity of turbulence.

Velocity and total deformation fields were investigated in the stator slots and the shear gap for both operating scenarios. Some qualitative differences were observed in the flow solutions. When a stator slot is blocked by a rotor tooth, the high operating scenario showed a jetting phenomenon near the volute cover, while the flow was a circulation loop in the low operating scenario. Within the shear gap, the high operating scenario showed greater axial and radial velocities (normalized to rotor tip speed). The variation in total deformation rate on the stator teeth was also greater in the high operating scenario.

It is recommended that the model be validated using PIV experiments. In addition, if further work with the low operating scenario is desired, additional study will be needed to determine whether the flow within the shear gap is laminar. If laminar flow is found, a technique for accounting for laminar flow in a specific region of a model should be developed.

COMPUTATIONAL FLUID DYNAMICS SIMULATIONS OF AN IN-LINE SLOT AND TOOTH ROTOR-STATOR MIXER

By
Derrick I. Ko

Thesis submitted to the Faculty of the Graduate School of the
University of Maryland, College Park in partial fulfillment
of the requirements for the degree of
Master of Science
2013

Advisory Committee:
Professor Richard V. Calabrese, Chair
Professor Kenneth Kiger
Professor Bao Yang

Acknowledgements

First and foremost, I would like to thank Dr. Richard V. Calabrese for the opportunity to work in his research group and for his mentorship, guidance, and patience during this project. I am looking forward to continuing research in this group for my doctoral studies.

I also appreciate the help and advice of the members of this research group: Dr. Justin Walker, Paul Rueger, Emily Chimiak, Kanan Ghaderzadeh, and Daniel Williams. Conversations within the group have helped to clarify and focus many elements of my research.

Finally, I would like to acknowledge my friends and family for their support of this endeavour. Thanks are due to my mother, father, Justin, Samantha, and Sydney for their encouragement throughout the last three years. To my girlfriend You-shin, thank you for your constant caring, listening, and advice.

Table of Contents

List of Figures

.

List of Tables

1. Introduction

Rotor-stator mixers are devices intended to provide more intensive mixing than can be achieved with conventional stirred tanks. These mixers dissipate a great deal of power in the volumes around the mixing head, resulting in regions of high local deformation rates that are conducive to high-intensity mixing. Currently, rotor-stator mixers are designed based on experience and experimentation because fundamental understanding of flow patterns and deformation rates within rotor-stator mixers is poor.

Simulation of fluid behaviour in a simple rotor-stator mixer using computational fluid dynamics (CFD) is a useful tool to develop better fundamental knowledge. One simple in-line device is the IKA prototype mixer, a single-stage slot and tooth rotor-stator mixer. In addition to its geometric simplicity, the IKA prototype mixer is attractive to study because of existing experimental data (to validate the CFD results) and previously conducted CFD simulations. Results of two-dimensional CFD simulations were reported by Kevala (2001). He also created a preliminary three-dimensional model that provided an initial view into flows through the stator slots, but grid independence and other aspects of the flow behaviour were not investigated.

The current work seeks to improve the fundamental understanding of fluid behaviour in rotor-stator mixers by further developing the three-dimensional CFD model of the IKA prototype mixer originally developed by Kevala to a state in which the results can be confidently compared to previously-collected experimental measurements. This first involves evaluating the effect of the improving grid resolution in the shear gap, where the velocity gradients and deformation rates are highest and accuracy most critical. The models for which grid-independent solutions are achieved are then examined in more detail to show various characteristics of the flow behaviour.

1.1. Mixing Processes

The Handbook of Industrial Mixing defines mixing as “the reduction of inhomogeneity in order to achieve a desired process result” (Atiemo-Obeng & Calabrese, 2004). In other words, the intent of mixing processes is to reduce the variation in particular properties, which may include concentration, phase, temperature, and other quantities of interest. Mixing is a common operation in everyday life; the following examples illustrate mixing and the properties of interest to control:

- The revolving drum for transporting concrete on a truck serves to agitate the concrete inside and prevent it from solidifying.
- Building heating, ventilation, and cooling systems use both forced and natural convection to keep internal air at a comfortable oxygen level and temperature.
- Stirring of food while frying seeks to heat food evenly on all surfaces and thereby prevent burning.

The study of mixing is a multi-disciplinary field, including material science, thermodynamics, transport phenomena, and reaction kinetics.

Mixing processes play important roles in a wide variety of industries, and improper design of mixing devices can have a significant impact on an organization’s capital and/or operational costs. For example, consider an inefficient design for a continuous stirred-tank reactor (CSTR) in the pharmaceutical industry. To achieve the desired product quality and output, an inefficient design may need to be larger and thus more expensive from a capital cost perspective. It might also need to have more recirculation to increase the residence time for the chemical reactions, requiring more potentially more power per unit of product. On the other hand, the optimal device for a mixing process will produce the desired product as much material, energy, and temporal efficiency as possible.

1.2. Rotor-Stator Mixers

In general, rotor-stator mixers are a category of mixing devices that consist of a high-speed rotating element (the *rotor*) and a stationary element (the *stator*). Figure 1.1 shows these elements in the IKA prototype mixer. The rotor and stator, both of slot (opening) and tooth configuration, are separated by the *shear gap*, a space between the outer surface of the rotor and the inner surface of the stator that is usually less than a millimetre in width. When the IKA prototype mixer is in operation, the working fluid enters the mixer from an inlet pipe that is coaxial with the rotor. After the fluid enters the mixer, it flows radially outward until it meets the rotor teeth, which impart a strong tangential velocity. As the fluid passes through the rotor slots, shear gap, and stator slots, it is exposed to the high shear field in these regions. Once past the stator slots, the fluid is collected in the volute and discharged through the outlet.

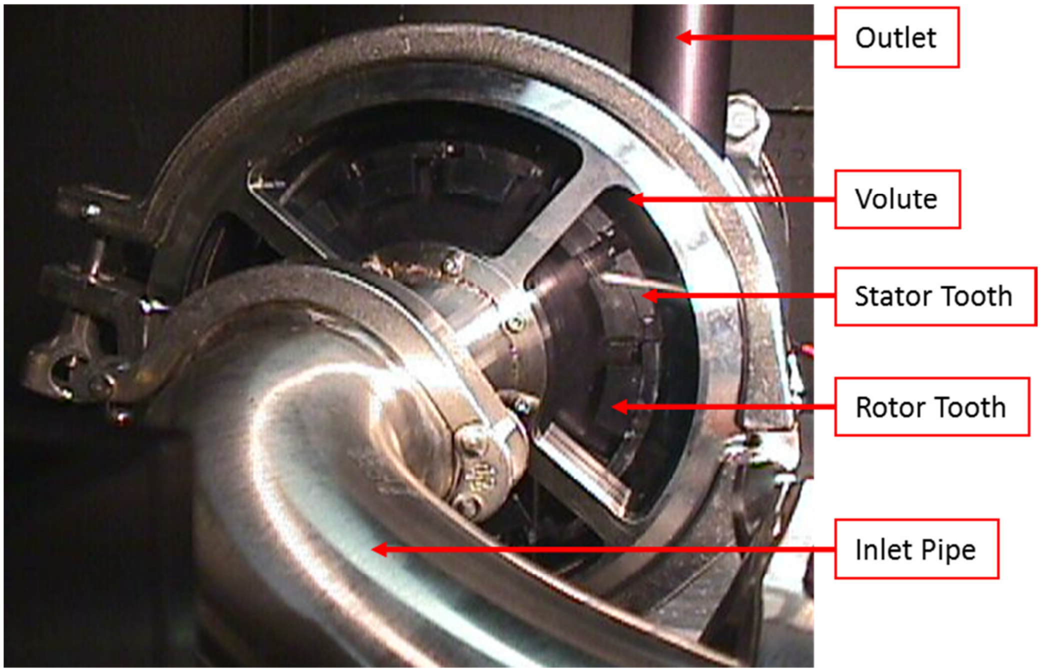

Figure 1.1: Elements of the IKA prototype rotor-stator mixer.

The rotor typically rotates at a speed much higher than the impeller in a conventional stirred tank. A rotor-stator mixer thus consumes a comparatively high amount of power, but produces higher local shear fields and energy dissipation levels that are conducive to more intensive mixing. These devices can have a variety of geometries and multiple process stages, and they may be used in inline, semi-batch, and batch arrangements.

A number of industries make use of rotor-stator mixers for shearing, emulsification, dispersion, and milling. Consumer products such as lotions, creams, and shampoos consist of immiscible components that must be dispersed into the continuous phase as very fine drops in order for the mixture or emulsion to be stable (i.e., to prevent separation over time). The pharmaceutical industry use rotor-stator mixers for wet milling, a process in which active pharmaceutical ingredients (APIs) are milled or ground into smaller crystalline particles within a liquid medium that absorbs some of the generated heat. Unlike conventional dry milling, liquid media are more effective at keeping the APIs within their thermal limits.

1.3. Detailed Geometry of the IKA Prototype Mixer

Figure 1.2 shows a simplified schematic of the IKA prototype mixer labelled with characteristic dimensions (in mm). The rotor rotates in the clockwise direction. There are twelve slots in the rotor and fourteen slots in the stator. The plan view diagram shows that each rotor and stator slot has a uniform width of 10 mm. The rotor slots and stator slots are 11.5 mm and 6 mm long, respectively. The inlet pipe has an internal diameter of 60 mm, while the outlet pipe has an internal diameter of 34 mm.

The Section A cut-away diagram provides additional information. The convention for direction is illustrated in the upper right corner. Note that the axial coordinate z is equal to zero at the volute cover and negative within the all of the shear gap. Since most of the model volume resides below the volute cover, an additional coordinate variable for depth $D_z = -z$ is also defined. Using this convention, the rotor slots are shown to be 10 mm deep, with an additional 0.25 mm clearance between the rotor teeth and the volute cover. The stator slots are 12 mm deep, but the stator teeth have no clearance. The 0.5 mm wide shear gap is highlighted in yellow. Note there is a volume of fluid behind the rotor that is exposed in the Section A view but hidden in the main plan view.

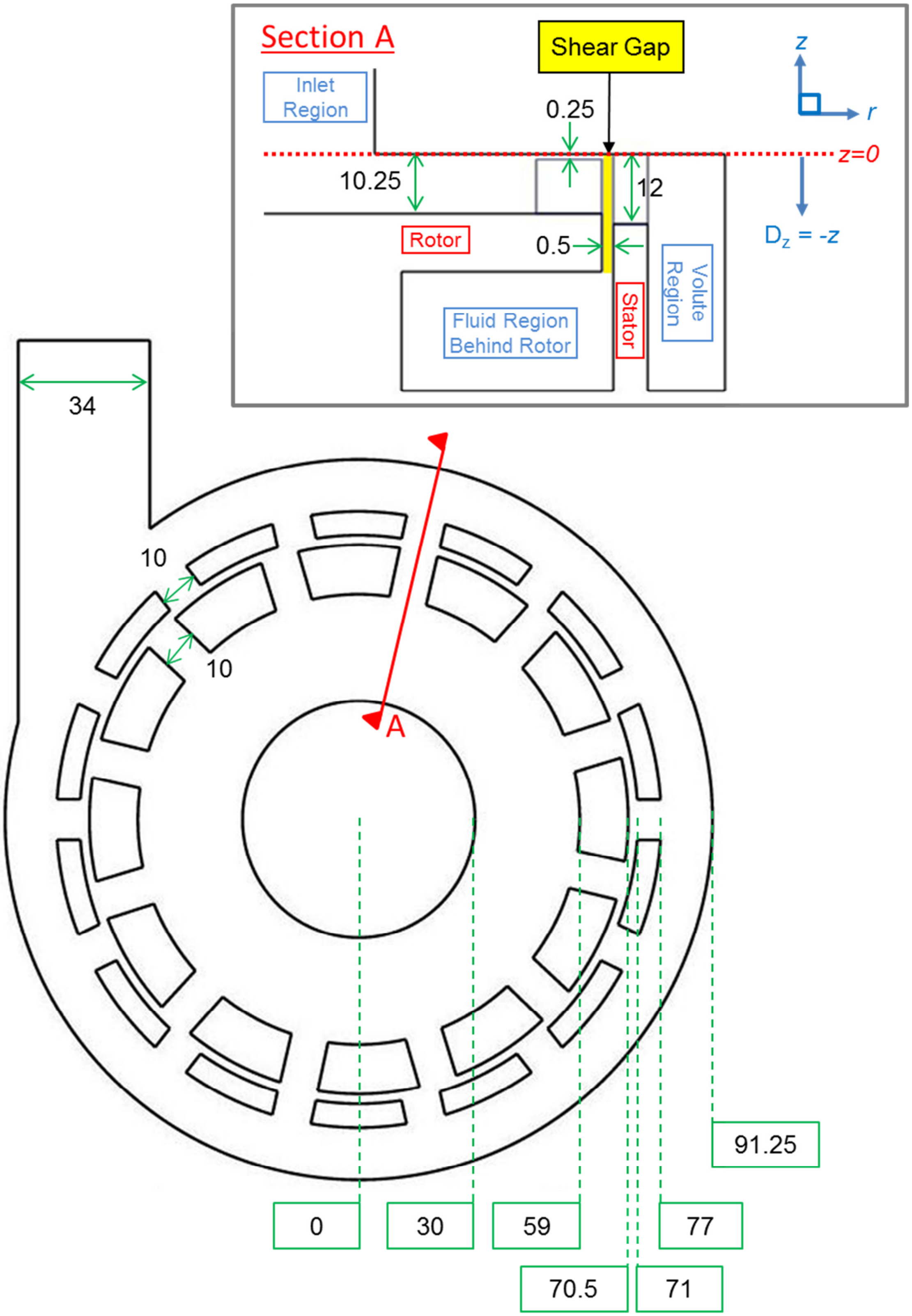

Figure 1.2: Representative plan and section views of the IKA prototype mixer. This schematic is intended to illustrate various dimensions of the mixer; the width of the shear gap has been exaggerated for illustration only. All measures are given in millimetres.

1.4. Previous Work with the IKA Prototype Mixer

An extensive amount of work was done by Kevala (2001) on two-dimensional sliding-mesh simulations of the IKA prototype mixer. The goal of this study was to quantify the flow fields for IKA prototype mixer with two different rotor heads and compare the results to experimental measurements. These rotor heads had the same slot geometry but differed in their outer diameter, creating different shear gap widths. Some of the key findings are summarized in Section 3.1. One important conclusion was that the flow field was three-dimensional and thus was not well-modelled with two-dimensional simulation.

Following the 2001 publication, Kevala conducted preliminary computational modelling and detailed experimental studies of the IKA prototype mixer. Computational studies undertaken with both RANS and large-eddy simulation (LES) focused on discovering general flow behaviour within the IKA prototype mixer. The experimental studies involved measuring the instantaneous velocity fields in the stator slots using particle image velocimetry (PIV) and time-averaged velocity fields with laser Doppler anemometry (LDA), with the goal of understanding the underlying physics and validating the computational results.

Figure 1.3 is an example of the PIV measurements. PIV measurements allow for a fine resolution of the flow field, and many small details such as the stator tooth vortex can be resolved. Because of the limitations in computational power during this previous study, examination of the grid independence of the solution was not included in the scope of work, and development of the CFD model was therefore not developed beyond the preliminary form. However, from the PIV data, it appears that the shear gap and immediately adjacent vicinities in particular experience large velocity gradients and thus would benefit from increased grid resolution.

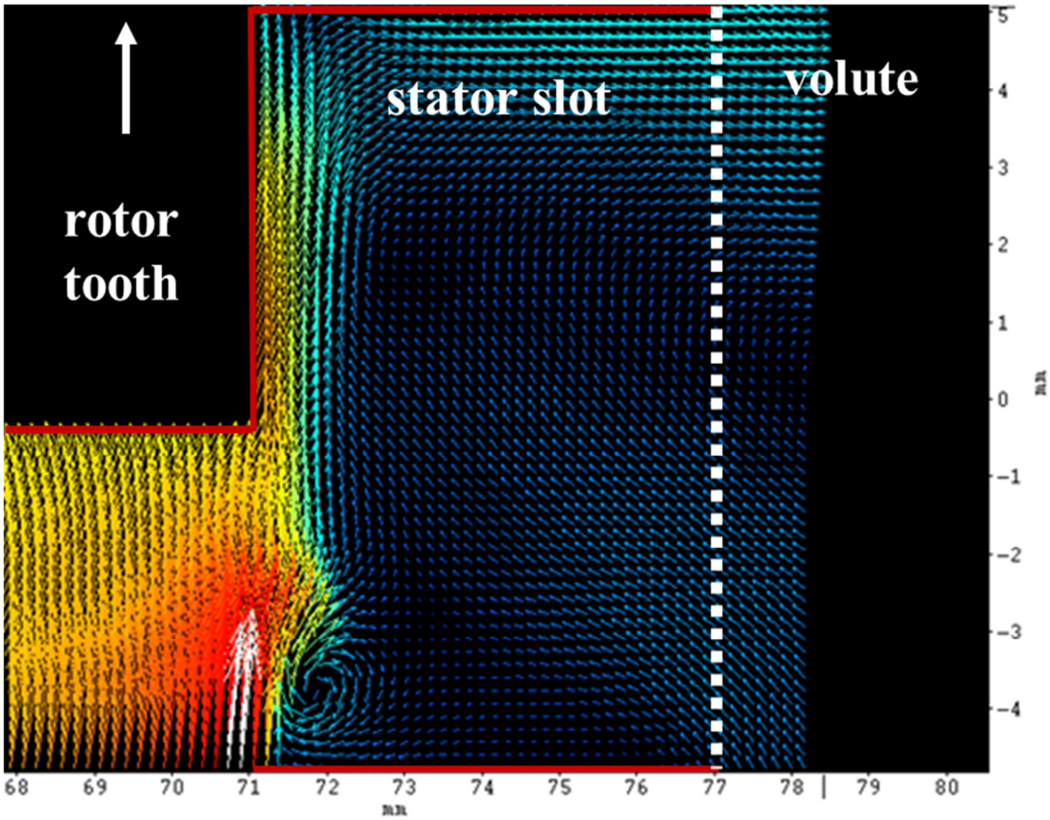

Figure 1.3: Example of PIV output. The angular speed of the rotor is 1200 rpm. The inlet volumetric flow rate is 1.29 L/s.

1.5. Objective of Current Project

While aspects of the flow behavior in rotor-stator mixers have been studied (Kevala [2001], Doucet et al. [2005], Barailler [2006], Pacek et al. [2007], Utomo et al. [2009], Yang [2011]), to the best of the author's knowledge, the flow characteristics in the shear gap have not been extensively explored using computational fluid dynamics. This region is of interest because it possesses the highest shear forces, but the narrowness of the shear gap makes it difficult to meet recommended meshing guidelines for cell aspect ratio (discussed in Section 4.3). Poor quality mesh in the shear gap can result in errors in the prediction of these high shear values that propagate to the rest of the model; therefore, it is important to model this region well.

The current work focuses on developing an enhanced CFD model of the IKA prototype mixer, with focus on improving the overall flow solution by increasing grid resolution in the shear gap. The ultimate goal is to produce a computational model that can be confidently compared to experimental measurements. The following steps are required to achieve this goal:

- conduct transient three-dimensional sliding-mesh CFD simulations of the IKA prototype mixer using the software package ANSYS FLUENT at a variety of grid sizes,
- identify the level of grid refinement needed to provide a grid-independent flow solution, and
- investigate the predicted fluid behaviour, particularly within the shear gap, for each operating scenario.

1.6. Layout of Thesis

The following is a list of items discussed in this thesis.

- Chapter 1 introduces the purpose of this study, general information about mixing and rotor-stator mixers, detailed description and dimensions of the IKA prototype mixer, and justification of the scope and approach.
- Chapter 2 reviews theoretical concepts related to useful metrics for rotor-stator mixers, turbulent transport phenomena, and computational techniques.
- Chapter 3 provides a literature review and summarizes the current state of knowledge with respect to investigation of mixing devices, with particular focus on rotor-stator mixers and the computational simulation of their behaviour.
- Chapter 4 provides details on the operating scenarios and computational model, including mesh configuration, surfaces investigated, and convergence criteria.
- Chapter 5 discusses the results of the grid independence study, including demonstration of simulation convergence and comparison of flow features between different levels of mesh refinement.
- Chapter 6 presents simulation results for the low operating scenario (300 rpm) in terms of velocities within the stator slot and shear gap, total deformation rate on stator teeth, and energy dissipation rates.
- Chapter 7 presents simulation results for the high operating scenario (1800 rpm) in terms of velocities within the stator slot and shear gap, total deformation rate on stator teeth, and energy dissipation rates.
- Chapter 8 concludes this thesis with a presentation of the main findings and discussion on future work.

2. Theoretical Background

This chapter provides additional details for some of the fluid dynamics concepts that are mentioned in previous chapters. Sections 2.1 to 2.3 define key measures with which the fluid behaviour and rotor-stator mixers are assessed. Sections 2.4 to 2.6 describe the fundamental transport equations (the Navier-Stokes equations) and the modelling of turbulent quantities. The remaining sections discuss numerical methodologies as implemented in ANSYS FLUENT (hereafter referred to as FLUENT for brevity) regarding the solution methods used in this work (summarized in Section 4.6).

2.1. Characteristic Metrics in Rotor-Stator Mixers

Flows through rotor-stator mixers have a number of metrics with which to characterize flow behaviour. The most basic metric is the *nominal shear rate* $\dot{\gamma}_{nom}$ (Equation 2.1-1). Assuming the flow in the shear gap behaved like simple plane Couette flow, the velocity profile across the gap would be linear, with a uniform nominal shear rate given by the speed of the rotor tip V_{tip} (i.e., the moving surface) divided by the width of the shear gap $\delta_{gap} = 0.5$ mm. This metric can also be thought of as the average velocity gradient across the shear gap. The corresponding *nominal shear stress* τ_{nom} (Equation 2.1-2) is the nominal shear rate multiplied by the dynamic viscosity of the fluid μ.

$$\dot{\gamma}_{nom} = \frac{V_{tip}}{\delta_{gap}} \tag{2.1-1}$$

$$\tau_{nom} = \mu \dot{\gamma}_{nom} \tag{2.1-2}$$

A metric for the flow regime (laminar, transition, or turbulent) is the *Reynolds number*. For flow through closed ducts and pipes, Reynolds numbers are generally less than 2,300 for laminar flows and greater than 4,000 for turbulent flows. Between these thresholds, the flow is in the transitional regime. Note that these thresholds are for fully-developed flows in straight conduits and are considered as ideal upper limits for the transition thresholds in this work; due to the constant disturbance of the flow by the rotor, transition of flow regimes likely occurs at lower Reynolds numbers.

The Reynolds numbers in the stator slot (Re_{slot}) and in the shear gap (Re_{gap}) are defined in Equations 2.1-3 and 2.1-4, respectively. In both cases, the Reynolds number is a product of the characteristic velocity, hydraulic diameter, and inverse of kinematic viscosity v. For the stator slot Reynolds number, the characteristic velocity is the average fluid velocity through the slots V_{slot}, defined as the total volumetric inlet flow Q divided by the total stator slot area A_{slot}. Based on the slot dimensions (see Figure 1.2), the hydraulic diameter is $D_{H,slot}$ = 10.91 mm. For the shear gap Reynolds number, the characteristic velocity is the average fluid velocity ($V_{tip}/2$, assuming plane Couette flow) and the hydraulic diameter is $2\delta_{gap}$.

$$Re_{slot} = \frac{V_{slot} D_{H,slot}}{\nu} \tag{2.1-3}$$

$$Re_{gap} = \frac{V_{tip} \delta_{gap}}{\nu} \tag{2.1-4}$$

Another metric is the *shearing number, N_{sh}*. This metric, calculated with Equation 2.1-5, is the ratio of the rotor tip velocity to the average fluid velocity through the stator slots. Substituting the velocities for Reynolds number using Equations 2.1-3 and 2.1-4, the shearing number can be expressed as being proportional to the ratio of shear gap Reynolds number to stator slot Reynolds number.

$$N_{sh} = \frac{V_{tip}}{V_{slot}} = 21.82 \frac{Re_{gap}}{Re_{slot}} \tag{2.1-5}$$

Since the shearing number for both operating scenarios is approximately 10, the stator slot Reynolds number is a factor of about 2 larger than the shear gap Reynolds number. This introduces a potential simulation problem for simulating low to moderate rotor speeds. The low operating scenario, as summarized in Table 4.1, is an example. The shear gap has a laminar Reynolds number of 1,100, while the stator slot Reynolds number is a borderline value of 2,040 that could represent transitional or even turbulent flow in the IKA prototype mixer. It is thus possible for two different zones of the mixer to be in different flow regimes. FLUENT does not permit a simulation to include both laminar and turbulent flows; the impact of this limitation is discussed in Section 6.4.

2.2. Strain Rate Tensor and Total Deformation Rate

Deformation rates describe how a fluid element is being compressed (or stretched) and sheared (or skewed). Because mixing is caused by fluid and interface deformation, quantifying deformation rates are useful as a measure the intensity of a mixing operation.

Deformation rates can be quantified with the strain rate tensor, given by Equation 2.2-1. Note that the strain rate tensor is symmetric. The elements along the diagonal describe the velocity gradients that cause normal strain and thus compression or elongation. The off-diagonal elements are the shear rates that cause angular deformation in a fluid element. Because a large part of this work focuses on the shear gap, it is convenient to write the strain rate tensor in cylindrical coordinates (radial coordinate *r*, angular coordinate *θ*, and the depth coordinate *z*).

$$\boldsymbol{\Delta} = \begin{bmatrix} 2\frac{\partial v_r}{\partial r} & \frac{1}{r}\frac{\partial v_r}{\partial \theta} + r\frac{\partial}{\partial r}\left(\frac{v_\theta}{r}\right) & \frac{\partial v_r}{\partial z} + \frac{\partial v_z}{\partial r} \\ \frac{1}{r}\frac{\partial v_r}{\partial \theta} + r\frac{\partial}{\partial r}\left(\frac{v_\theta}{r}\right) & 2\left(\frac{1}{r}\frac{\partial v_\theta}{\partial \theta} + \frac{v_r}{r}\right) & \frac{1}{r}\frac{\partial v_z}{\partial \theta} + \frac{\partial v_\theta}{\partial z} \\ \frac{\partial v_r}{\partial z} + \frac{\partial v_z}{\partial r} & \frac{1}{r}\frac{\partial v_z}{\partial \theta} + \frac{\partial v_\theta}{\partial z} & 2\frac{\partial u_z}{\partial z} \end{bmatrix} \qquad (2.2\text{-}1)$$

The *total rate of deformation* is the magnitude of the strain rate tensor, as shown in Equation 2.2-2. The total deformation rate is based on the second moment of the rate of deformation tensor and is independent of the applied coordinate system.

$$\dot{\gamma} = \sqrt{\frac{1}{2}\boldsymbol{\Delta} : \boldsymbol{\Delta}} \qquad (2.2\text{-}2)$$

FLUENT can report velocities in Cartesian or cylindrical form, but the velocity gradients are reported only in Cartesian form. Because the total deformation rate is independent of coordinate system, it serves as a useful overall measure of deformation and mixing. However, evaluating velocity gradients (or tensor components) separately can be useful to gauge the relative importance of each element. In this work, these gradients were primarily calculated using central finite difference approximation. As an example, consider evaluating velocity gradients at the stator wall using velocity information from the adjacent cell. This cell is at a general location (r_i,θ_j,z_k), where i, j, and k are integer indices, and the mesh spacing is uniform (i.e., Δr, $\Delta\theta$, and Δz are constant). The analytical derivative of an arbitrary velocity component ϕ with respect to θ and z at (r_i,θ_j,z_k) can be expressed as the central difference approximations shown in Equation 2.2-3.

$$\left.\frac{\partial\phi}{\partial\theta}\right|_{i,j,k} = \frac{\phi_{i,j+1,k} - \phi_{i,j-1,k}}{2\,\Delta\theta}$$

$$\left.\frac{\partial\phi}{\partial z}\right|_{i,j,k} = \frac{\phi_{i,j,k+1} - \phi_{i,j,k-1}}{2\,\Delta z} \qquad (2.2\text{-}3)$$

Because the cell is bounded in the radial direction by the stator wall, the finite difference approximation of the radial gradients are instead expressed as Equation 2.2-4. Because the no-slip boundary condition is applied to all surfaces, velocity components at the stator wall are zero.

$$\left.\frac{\partial\phi}{\partial r}\right|_{i,j,k} = \frac{0 - \phi_{i,j,k}}{0.077 - r_i} \qquad (2.2\text{-}4)$$

2.3. Rotor Torque, Power Number, and Energy Dissipation

From an operational perspective, the torque requirements and power numbers are important parameters in specifying rotor-stator mixers. Pressure and viscous forces act on each point of the moving rotor surface and thereby exert moments along the centreline of the rotor axis. The rotor torque T is the integral (or sum) of the total moments across the moving surfaces of the rotor. The corresponding power consumed P is calculated with Equation 2.3-1 (Jaworski et al., 1997), where N is the angular speed of the rotor in revolutions per second.

$$P = 2\pi NT \tag{2.3-1}$$

The *power number* N_{Po} is defined in Equation 2.3-2, where ρ is the fluid density and r is the radius of the rotor. The power number is the ratio of the resistance forces to inertial forces.

$$N_{Po} = \frac{P}{\rho N^3 (2r)^5} \tag{2.3-2}$$

Within the fluid, energy is dissipated due to friction between fluid molecules. Equation 2.3-3 shows that, in this work, the total dissipated energy ε_{total} will be defined based on two quantities: 1) dissipation due to mean velocity gradients, and 2) dissipation due to turbulent eddies, called the turbulence dissipation rate ε. These two quantities are the first and second terms, respectively, on the right hand side of Equation 2.3-3.

$$\varepsilon_{total} = \mu\dot{\gamma}^2 + \rho\varepsilon \tag{2.3-3}$$

2.4. Navier-Stokes Equations – Mass and Momentum Conservation

The general motion of any fluid element is described using partial differential equations that conserve two principal quantities. The first quantity is mass, and its conservation law is known as the *continuity* equation. Equation 2.4-1 is the continuity equation for incompressible Newtonian flows using j as a summation index for the three Cartesian spatial dimensions. The velocity component in the j^{th} direction is denoted as v_j.

$$\frac{\partial v_j}{\partial x_j} = 0 \tag{2.4-1}$$

The second quantity is momentum, governed by the *Navier-Stokes* equations. Momentum is a vector quantity, so each spatial direction x_i has a corresponding equation that balances the forces acting on a fluid element against the fluid element's change in x_i-momentum in both space and time. Net forces in direction i result in a change in the velocity component v_i. Equation 2.4-2 is the Navier-Stokes equations in Cartesian coordinates for incompressible Newtonian flows in the absence of body forces, where ρ is the density and μ is the dynamic viscosity (i and j are free and summation indices, respectively).

$$\rho\left(\frac{\partial v_i}{\partial t} + v_j\frac{\partial v_i}{\partial x_j}\right) = -\frac{\partial P}{\partial x_i} + \mu\frac{\partial}{\partial x_j}\left(\frac{\partial v_i}{\partial x_j}\right) \tag{2.4-2}$$

In most real-world flow scenarios, the Navier-Stokes equations cannot be solved analytically. CFD solvers such as FLUENT can yield insight into complicated flows by solving the Navier-Stokes equations and other transport equations using finite difference approximations.

2.5. Reynolds Averaged Navier-Stokes Equations for Turbulence

Equations 2.4-1 and 2.4-2 describe the instantaneous state of any flow exactly. However, in the case of turbulent flows, velocity fluctuations and turbulent eddies increase the computational complexity. This means that from a practical perspective, using only equations 2.4-1 and 2.4-2 to simulate fluid flow is more suitable for laminar systems. Solving turbulent systems requires either calculation of turbulent quantities or additional equations to model the turbulent behaviour.

The approach used in this project is based on a time- or ensemble-averaged version of the Navier-Stokes equations. By substituting the instantaneous flow variables with mean and fluctuating components (denoted with overbars and apostrophes, respectively) and averaging the continuity and momentum equations over time, the *Reynolds Averaged Navier-Stokes (RANS)* equations were developed. These equations as applied to incompressible flows are shown as Equations 2.5-1 and 2.5-2.

$$\frac{\partial \overline{v_i}}{\partial x_j} = 0 \tag{2.5-1}$$

$$\rho\left(\frac{\partial \overline{v_i}}{\partial t} + \overline{v_j}\frac{\partial \overline{v_i}}{\partial x_j}\right) = -\frac{\partial \overline{P}}{\partial x_i} + \mu\frac{\partial}{\partial x_j}\left(\frac{\partial \overline{v_i}}{\partial x_j}\right) - \rho\frac{\partial \overline{u_i' u_j'}}{\partial x_j} \tag{2.5-2}$$

Note that the RANS equations, which are essentially ensemble-averaged continuity and Navier-Stokes equations, are nearly identical to the instantaneous forms (Equations 2.4-1 and 2.4-2) discussed in the previous section. The difference is that the RANS equations contain additional terms called Reynolds stresses that account for turbulent fluctuations. Since the Reynolds stresses are additional variables in the RANS equations, additional equations are required to solve the flow problem.

There are two approaches that can be considered. The first and most detailed approach is to solve transport equations for each of six Reynolds stresses (for three-dimensional flow). An additional transport equation for scaling, such as turbulence dissipation, is also needed. These seven extra transport equations significantly add to the computational expense of a CFD simulation. A second and more approximate approach is to model the Reynolds stresses. One common approach was developed by Joseph Boussinesq in 1887, shown in Equation 2.5-3 for incompressible flow. He proposed evaluating the Reynolds stress as proportional to the gradients of mean velocity, similar to a shear stress. The parameter of proportionality μ_t is a scalar called the *turbulent or eddy viscosity*. The turbulent viscosity is modelled as an isotropic variable (i.e., a variable that not dependent on direction), but it has been found that in many cases, the Boussinesq approximation results in good simulation performance.

$$-\rho\overline{u_i'u_j'} = \mu_t\left(\frac{\partial\overline{v_i}}{\partial x_j}+\frac{\partial\overline{v_j}}{\partial x_i}\right) \tag{2.5-3}$$

With the Boussinesq approximation, the momentum conservation equations become as shown in Equation 2.5-4. Note that this expression assumes constant density and dynamic viscosity. The turbulent viscosity is isotropic (i.e., independent of direction) but a function of the flow field.

$$\rho\left(\frac{\partial\overline{v_i}}{\partial t}+\overline{v_j}\frac{\partial\overline{v_i}}{\partial x_j}\right)=-\frac{\partial\overline{P}}{\partial x_i}+\frac{\partial}{\partial x_j}\left[(\mu+\mu_t)\left(\frac{\partial\overline{v_i}}{\partial x_j}\right)\right] \tag{2.5-4}$$

2.6. Modelling Turbulent Viscosity with the k-ε Model

As discussed in the previous section, use of the Boussinesq approximation requires additional equations to model the turbulent viscosity μ_t. A number of models with a wide range of complexity exist today. The simplest models, the zero-equation models, can calculate the turbulent viscosity algebraically from the flow variables, but their application tends to be limited to simple flow geometries. 1-equation models, such as Prandtl's model, utilize a single partial differential equation (PDE) to solve turbulent viscosity and are thus more computationally intensive than the 0-equation models.

Most turbulent viscosity models are 2-equation models, requiring two transport equations to calculate turbulent viscosity. This project utilized a category of semi-empirical models referred to as k-ε models, originally developed by Launder and Spalding (1974). As shown in Equation 2.6-1, turbulent viscosity is calculated from two transport properties: *turbulent kinetic energy k* and *turbulence dissipation ε*. In the standard k-ε model, the constant $C_\mu = 0.09$.

$$\mu_t=\rho C_\mu\frac{k^2}{\varepsilon} \tag{2.6-1}$$

k-ε turbulence models are popular for a wide range of industrial applications, and as they have been used and tested, modifications have been introduced to account for discovered weaknesses. One improved version of the standard k-ε model is known as the realizable k-ε model. It attempts to correct two deficiencies in the standard k-ε model. First, when strain rates are large, the standard k-ε model can produce non-physical normal and shear stresses. This is addressed by allowing the turbulent viscosity parameter C_μ to vary, instead of remaining constant as in the standard k-ε model. Second, the standard k-ε model utilizes an empirical transport equation for turbulence dissipation that is believed to be the cause of poor spreading rate predictions for laminar jets. The realizable k-ε model replaces the empirical ε equation with a new model based on vorticity fluctuation.

Equation 2.6-2 describes the transport of the turbulent kinetic energy with the realizable k-ε model. The fluid is taken to be incompressible in this equation. The second term on the right-hand side of the equation is the generation of turbulence from velocity gradients. The third term on the right-hand side is the dissipation of turbulence. Buoyancy and compressibility can also generate turbulence, but these terms are neglected in Equation 2.6-2 because their effects are not significant in the current project.

$$\rho\left(\frac{\partial k}{\partial t}+\frac{\partial(kv_j)}{\partial x_j}\right)=\frac{\partial}{\partial x_j}\left[\left(\mu+\frac{\mu_t}{\sigma_k}\right)\frac{\partial k}{\partial x_j}\right]+\mu_t\dot{\gamma}^2-\rho\varepsilon \qquad (2.6\text{-}2)$$

Equation 2.6-3 is the transport equation for turbulence dissipation, again for incompressible flow. C_2, σ_k, and σ_ε are model constants; their default values optimize performance of the model for benchmark scenarios ($C_2 = 1.9,\ \sigma_k = 1.0,\ \sigma_\varepsilon = 1.2$).

$$\rho\frac{\partial\varepsilon}{\partial t}+\rho\frac{\partial\left(\varepsilon v_j\right)}{\partial x_j}=\frac{\partial}{\partial x_j}\left[\left(\mu+\frac{\mu_t}{\sigma_\varepsilon}\right)\frac{\partial\varepsilon}{\partial x_j}\right]+\rho C_1\dot{\gamma}\varepsilon-\rho C_2\frac{\varepsilon^2}{k+\sqrt{\upsilon\varepsilon}}$$

$$C_1=\max\left[0.43,\frac{\eta}{\eta+5}\right],\eta=\dot{\gamma}\frac{k}{\varepsilon} \tag{2.6-3}$$

2.7. Flow Simulation in ANSYS FLUENT

To solve the previously discussed transport equations, the commercial software package ANSYS FLUENT Version 13 was used. FLUENT converts the continuous transport equations presented above into discretized forms around each computational volume or cell. Balance of the transport equations in each cell implies overall conservation within the model.

FLUENT uses a co-located scheme to store flow field variables, in which all flow data associated with a cell is stored at the coordinates of the cell's centroid. This technique allows for simple storage of flow data, but then requires interpolation to calculate flux values at cell faces. In contrast, a staggered grid has a different mesh for each flow variable. A mesh of this can be more difficult to construct, but strategic placing of the cells can reduce interpolation errors. For example, centering a pressure centroid on the boundary of momentum cell eliminates the need to interpolate pressure at the cell face.

This project utilized the pressure-based solver, the more commonly applied solver for incompressible flows, to develop the flow field. Because the transport equations are coupled but are solved sequentially, iteration is needed to reach a converged solution at each time step. The following steps are conducted at each iteration.

1. Flow-field dependent properties are updated. In this project, only turbulent viscosity must be updated at this step, since density and viscosity are constant.
2. Momentum equations are solved sequentially.
3. Pressure correction for pressure-velocity coupling is determined.
4. Mass flux, pressure, and velocities at the cell faces are corrected based on the pressure correction.
5. Turbulent kinetic energy and turbulence dissipation equations are solved sequentially.
6. Residuals are compared to convergence criteria. If convergence criteria are met, proceed to the next time step.

2.8. Fluid Zones, Reference Frames, and Sliding Meshes

In FLUENT, a modeller is permitted to define different fluid zones. Each fluid zone includes the cells of a specified region of the model, and all cells in the model must belong to a fluid zone. Fluid zones are necessarily established between mesh volumes that have a non-conformal interface, for which there is not a one-to-one connection between cells across the interface. A common example occurs at the outlet to the IKA prototype mixer. The complex geometry of the outlet is meshed with tetrahedral elements, while the rest of the model is meshed with hexahedral elements. The cells at the interface between these two volumes cannot have a one-to-one correspondence because of their vastly different shape. Another more important reason to define fluid zones is to establish regions where different frames of reference will be used. This is often needed to model flow around rotating equipment, such as a rotor or impeller in mixing equipment. Reference frames for modelling fluid flow around rotating bodies are discussed in more detail below.

The simplest method to solve the flow field around a rotor or other rotating body is to utilize a *single reference frame* (SRF). The frame of reference is taken to be stationary with the rotor, and the wall is then defined as a moving surface (relative to the rotor). The mesh geometry does not change with time. The SRF technique is better employed in cases where there is little interaction between the rotating part and the wall, such as an impeller in the center of an unbaffled tank.

The second method is to use *multiple reference frames* (MRF). The model must have at least two fluid zones; for example, the CFD model of the IKA prototype mixer has separate fluid zones for the rotor and the stator (see Section 4.2 for more details). With the MRF technique, the rotor zone is solved in its own rotating reference frame, while the stator zone is solved in a stationary reference frame. A transformation of the flow variables at interface cells is required to calculate fluxes. While the expected tangential velocities would be imparted by the rotor due to the rotating reference frame, the MRF technique cannot capture any transient effects caused by changes in geometry, such as the opening and closing of the stator slots in a rotor-stator mixer, because the mesh geometry does not change. The MRF technique is thus poorly suited to model flow through rotor-stator mixers, although it is commonly used to develop an initial flow solution for a sliding mesh simulation.

For rotor-stator mixers, the *sliding mesh* technique is the most common method for evaluating the transient flow field, and was thus applied to the IKA prototype mixer in this work. Similar to the MRF technique, the CFD model must be separated into at least two fluid zones. At each time step, the cell zones rotate and/or translate with respect to each other in one discrete stage. This adds two additional aspects to the simulation at each time step. First, the location of each of the cells in the moving zone(s) must be updated. Second, and more importantly, the relationship between cells at the interface must be broken and re-formed because such an interface is necessarily non-conformal. This makes the sliding mesh technique more computationally-intensive than the SRF and MRF techniques, but sliding meshes are necessary to accurately resolve the time-periodic flow features of rotor-stator mixers.

2.9. Finite Volume Equations and Discretization Technique

As a finite volume solver, FLUENT solves the transport equations for mass, momentum, turbulent kinetic energy, and turbulence dissipation rate over discrete control volumes. For a flow variable ϕ, the discrete conservation equation is expressed in Equation 2.9-1, where V is the cell volume, N is the total number of faces, ϕ_f is the value of the flow variable at face f, $\vec{v}_f$ is the velocity at face f, $\vec{A}_f$ is the area vector of face f, Γ_ϕ is the diffusion coefficient, and S_ϕ is the source of the flow variable per unit volume.

$$\rho \frac{\partial \phi}{\partial t} V + \rho \sum_{f}^{N} \vec{v}_f \phi_f \cdot \vec{A}_f = \sum_{f}^{N} \Gamma_\phi \nabla \phi_f \cdot \vec{A}_f + S_\phi V \tag{2.9-1}$$

Cell-centre gradients, face gradients, and fluxes at the cell boundaries must be calculated to solve the finite volume forms of the transport equations. The time-marching technique must also be established. The methods used in this project are discussed in greater detail in the following subsections.

2.9.1. Numerical Evaluation of Cell-Centre Gradients

Cell-centre gradients are calculated using the Gauss theorem. This theorem states that integral of a scalar value ϕ over the cell surface *S* is equal to the integral of the gradient of the scalar over the cell volume *V*. The continuous form of this theorem is presented in Equation 2.9-2.

$$\int_S \phi \, \hat{n} \, dS = \int_V \nabla \phi \, dV \tag{2.9-2}$$

For a discrete system, this theorem can be used to numerically approximate the gradient at the centre of a computational cell ($\overline{\nabla \phi}_{cell}$) by summing the product of the scalar value and face area around the cell ($\overline{\phi}_f$and $\overline{A}_f$, respectively) and dividing by the cell volume *V*, as shown in Equation 2.9-3.

$$\overline{\nabla \phi}_{cell} = \frac{1}{V} \sum_{f} \overline{\phi}_f \overline{A}_f \tag{2.9-3}$$

Using this method requires estimation for the value of the scalar at the face between each pair of cells. With the Green-Gauss cell-based derivative evaluation option in FLUENT, $\overline{\phi}_f$ is calculated as the arithmetic average of the pair of cell-centre scalar values. Note that while this approximation is simple and easily calculable, it is a source of error when the cell centers are not equidistant from the face. This can occur if neighbouring cells have differing aspect ratios, skew, and/or volumes. The errors are more significant in areas with higher gradients. As a metric for assessing mesh quality, FLUENT recommends that the volume ratio between two adjacent cells not exceed a factor of 1.2.

2.9.2. Discretization in Space

The convection terms that describe the rate at which a flow quantity is brought into the cell require evaluation of flow field variables at the cell faces. Because central differencing of face values can result in non-physical upstream propagation of downstream effects in flow problems, the face fluxes are commonly evaluated using only information from cells upwind of the face. In principle, for systems in which convection is the sole method of transport, these upwind schemes result in data travelling only in the downstream direction. Note that the diffusion terms are always calculated using central-differencing; therefore, information can still travel upstream through the diffusion effects.

The most basic method of evaluating the face flux is to assume that the cell-centre scalar value φ is uniform throughout the cell, including its faces. The estimated value of the scalar at each face is then the cell-centre value of the upwind cell. This first-order approximation is simple in that calculating the face value requires only the identification of the upwind cell based on the direction of flow. However, gradients between cells will cause errors in the face values. This first-order upwind scheme is therefore ill-suited to model flow through a rotor-stator mixer.

A more accurate method of evaluating scalar quantities at a cell face is to use a second-order upwind scheme. In FLUENT, the second-order upwind scheme estimates the face value by using Equation 2.9-4. Each face value is calculated as cell-centre scalar value ϕ of the upwind cell modified by the scalar product of the upwind cell-centre gradient $\nabla\phi$ and the unit vector $\vec{r}$ connecting the cell-centre centroid to the face centroid. Note that the gradient in Equation 2.9-4 is limited such that the estimated face value is between the maximum and minimum values of the adjacent cells. The intent of this restriction is to prevent the numerical oscillations that would otherwise be produced near sharp gradients.

$$\phi_f \cong \phi + \nabla\phi \cdot \vec{r} \qquad (2.9\text{-}4)$$

2.9.3. Discretization in Time

To advance the flow solution in time, the temporal partial derivative must be discretized. Conceptually, this can be done by re-arranging the transport equations to the form shown in Equation 2.9-5. The left-hand side of the equation is the exact change of a flow variable ϕ in time, while the right-hand side is the remainder of the equation, including the spatial discretization and any source and sink terms.

$$\frac{\partial \phi}{\partial t} = F(\phi) \tag{2.9-5}$$

For this project, a backward-differenced 2nd-order accurate time discretization was chosen (see Equation 2.9-6) to approximate the partial derivative in time. The scheme utilizes the flow variable values at two previous known states (*n* and *n-1*) to calculate the flow variable at the unknown new state (*n+1*).

$$\frac{\partial \phi}{\partial t} \cong \frac{3\phi^{(n+1)} - 4\phi^{(n)} + \phi^{(n-1)}}{2\Delta t} \tag{2.9-6}$$

On the right-hand side of Equation 2.9-5, the time level at which to evaluate *F* can also be selected. Two of the most basic methods are to evaluate *F* at either the most recent known state (*n*) or the next state being calculated (*n+1*). The former, referred to as explicit time-marching, is computationally inexpensive per time step because the new state is calculated directly from the previous state. However, to maintain numerical stability, the time step size must be relatively small. The second method is referred to as implicit time-marching. In this method, both sides of the equation depend on the unknown state of the system at *n+1*, so an iterative scheme is needed to solve the system. Despite its higher computational cost, this work utilized the implicit method because it is unconditionally stable with respect to the size of the time step.

Combining the 2nd-order time discretization with the implicit method creates Equation 2.9-7. At each time step, this equation is solved iteratively at every computational cell until the solution has converged.

$$\phi^{(n+1)} = \frac{4\phi^{(n)} - \phi^{(n-1)} + 2\Delta t \cdot F(\phi^{(n+1)})}{3} \tag{2.9-7}$$

2.10. Wall Functions versus Near-Wall Modeling

The finite volume equations at each time step essentially represent a boundary value problem, so the treatment of fluid boundary layers at model surfaces is of critical importance in CFD simulations. This is particularly important in the current work because the shear gap, one of the primary regions of interest, is strongly affected by boundary conditions.

Experimental data for boundary layers show three distinct fluid zones or layers near the wall. The layer closest to the wall is the viscous sublayer. The viscosity of the fluid and the physical restriction imposed by the wall dampen velocity fluctuations in the fluid, resulting in laminar behaviour very close to the wall. On the other hand, the layer furthest from the wall (i.e., closest to the bulk fluid zone) is dominated by turbulent shear. Between these two layers, both viscosity and turbulent shear play significant roles.

Because a significant amount of turbulence in generated at the walls, one of the critical factors in the accuracy of a turbulent flow simulation is the evaluation of fluid behaviour near walls. There are two general categories of approaches. The first is to use a semi-empirical formula, called a *wall function*, to model the fluid behaviour near the wall. The advantage of wall functions is that they tend to be less computationally intensive because a relatively fine level of discretization is not required. The second method is to refine the grid to resolve the viscous sublayer; this method is known as *near-*

wall modelling. Because the domain is gridded into the viscous sublayer, it is not necessary to rely on the semi-empirical correlations that primarily account for center and outer layers of the near-wall region.

FLUENT has a number of alternatives for wall functions. The default technique is the *standard wall function* developed by Launder and Spalding (1974) relates the mean velocity to the distance from the wall using a law-of-the-wall formula. Production of turbulent kinetic energy and the rate of dissipation in the cells adjacent to the wall are considered to be equal, based on the local equilibrium hypothesis.

One of the alternate methods is the *non-equilibrium wall function*, which is based on the work of Kim and Choudhury (1995). The mean velocity log-law is modified to include the effect of pressure gradients, and the formulas used to calculate the turbulent quantities at cells adjacent to the wall depend on whether the cell is in the viscous sublayer. Non-equilibrium wall functions are useful when fluids experience high pressure gradients, separation, and impingement on surfaces. These conditions are frequently encountered in CFD simulations of rotor-stator mixers, so non-equilibrium wall functions were applied in the current project.

One of the weaknesses of the wall function approach is that correlations were developed for specific volume geometries and flow conditions. In practice, the wall functions are often used for a wide variety of complicated flows in the absence of better models, but it is important for the engineer to be aware of the error potential in using wall functions. As an alternative, the grid cells near the wall can be refined into the viscous sublayer in a technique referred to as near-wall modelling. The advantage of near-wall modelling is that the velocities at the grid cells adjacent to the wall are derived from the equation for wall shear stress. This can be expressed by the laminar stress-strain relationship shown in Equation 2.10-1, where y and v are the position and mean fluid velocity at the near-wall cell, respectively. When the laminar stress-strain relationship is applicable, the calculation of the near-wall velocity gradients using finite differences is more accurate (see Section 2.2).

$$\frac{v C_\mu^{0.25}\, k^{0.5}}{\tau_w/\rho} = v^* = y^* = \frac{\rho\, C_\mu^{0.25}\, k^{0.5}\, y}{\mu} \tag{2.10-1}$$

The disadvantage of near-wall modelling is that a substantially larger number of cells are required to create the near-wall grid, which increases computational time.

2.11. Pressure-Velocity Coupling

One of the challenges with using the continuity and Navier-Stokes equations is that the four equations (one mass and three momentum balances) are not written in terms of all of the four field variables (pressure and three velocity components). Because the Navier-Stokes equations are used to solve for the velocity field, ideally the continuity equation could be directly used to solve for the pressure field. However, the velocity field based on an intermediate pressure field does not result in face mass fluxes that satisfy continuity. Because pressure does not appear in the continuity equation, this equation cannot be directly used to correct the pressure field based on the imbalance in the mass fluxes.

To address this problem, the continuity equation can be reformatted to include all field variables by defining the mass flux at each face as a function of pressure and velocity. This coupling of pressure and velocity fields in the continuity equation leads to an equation with which pressure field can be solved iteratively.

One of the most commonly used methods is the Semi-Implicit Method for Pressure-Linked Equations (SIMPLE) algorithm, developed by Patankar (1980). Patankar proposed that the pressure correction can be calculated from a linearized scalar transport equation. This pressure correction results in the summation of the mass fluxes for each cell that satisfies the continuity equation.

One of the weaknesses of the SIMPLE algorithm is that the momentum equations are no longer satisfied after the pressure field is adjusted. Solution to the flow field then requires an increased number of iterations, which is unfavourable from a computational perspective. The Pressure-Implicit with Splitting of Operators (PISO) algorithm, used in the current project, is an evolution of the SIMPLE algorithm that has two additional corrections to address the imbalance in momentum. The first correction, referred to as neighbour correction, adjusts the velocity field to satisfy both continuity and momentum equations. While this results in more computational time per iteration, it often decreases the number of iterations required to reach convergence. The second correction is known as skewness correction. The calculation of pressure correction term is approximate and generally very rough for highly skewed cells. The skewness correction recalculates the pressure correction to account for the irregular cell geometry and generally reduces divergence caused by cell distortion. These corrections can be coupled to the same pressure correction equation, but this approach can be less robust than applying neighbour and skewness corrections sequentially.

2.12. Measures of Convergence

In the modelling of periodic flows, there are two convergence types that need to be fulfilled to have a good flow solution. The first type is the iteration convergence. This is intended to evaluate how well the current solution agrees with the finite volume equations discussed in Section 2.9. The second type of convergence is flow field convergence. Ideally, the flow solution at steady state will be perfectly periodic in 30° intervals because the rotor consists of twelve regularly spaced teeth. In other words, there should be no difference in flow field at every point in the domain after one rotor period of 30°. The flow field convergence quantifies the difference between two flow solutions as a measure of closeness to the quasi-steady state solution. The following discussion details how these convergences were applied to the current work.

For iteration convergence, FLUENT tests the numerical convergence of each flow field variable by evaluating the residual of its transport equation. Consider the general discrete transport equation for a scalar variable ϕ, shown in Equation 2.12-1. Subscripts P and nb denote the centre and neighbouring cells, respectively. Equation 2.12-1 is essentially a generic form of the finite volume Equation 2.9-1, expressing the value of ϕ at the centre cell as a function of the neighbouring scalar values (weighted by coefficients a) and a source term b.

$$a_P \phi_P = \sum_{nb} (a_{nb} \phi_{nb}) + b \tag{2.12-1}$$

Ideally, Equation 2.12-1 is satisfied exactly. However, the iterative solution methods employed to solve the non-linear partial differential equations in FLUENT generally result in an imbalance in the transport equation. The sum of the magnitude of imbalances for all cells in the model is called the *unscaled residual*. Note that the unscaled residual potentially increases with the number of cells in the model and is therefore not generally used as a measure of convergence. This project instead evaluates convergence based on the *scaled residual* R^{ϕ} shown in Equation 2.12-2. The unscaled residual, in the numerator, is scaled by the sum of the scalar values ϕ for all cells in the model.

$$R^{\phi} = \frac{\sum_P \left| \sum_{nb} (a_{nb} \phi_{nb}) + b - a_P \phi_P \right|}{\sum_P \left| a_P \phi_P \right|} \tag{2.12-2}$$

The residual of the continuity equation is also defined as the unscaled residual divided by the scaling factor, but the calculation of these components differs. The unscaled residual is the sum of the magnitude of mass creation terms over all terms at the current iteration. The scaling factor is the largest unscaled residual from the first five iterations.

In this work, the residual monitor was set to advance to the next time step when residuals became less than 10^{-4} for continuity and 10^{-5} for momentum, turbulent kinetic energy, and turbulence dissipation rate. In practice, turbulence dissipation rate needed the most iteration to meet its residual target. Continuity, momentum, and turbulent kinetic energy residuals were significantly less than targeted thresholds prior to proceeding to the next time step.

The second type of convergence, flow field convergence, is reached when the profile of all flow field variables as a function of rotor position (or equivalently time) is the same over successive periods. In other words, when two successive periods have flow fields that are within a particular level of tolerance convergence has been reached. The relative change equation, shown as Equation 2.12-3, quantifies the difference between the scalar variable ϕ_1 at an earlier State 1 and ϕ_2 at a later State 2 (with the same geometric configuration as State 1 and thus identical flows under perfectly periodic conditions). The relative change is normalized to ϕ_1.

$$\Delta\phi_{rel} = \frac{\phi_2 - \phi_1}{\phi_1} \qquad (2.12\text{-}3)$$

To characterize flow field convergence, the relative change of representative velocity and total deformation profiles were quantified. The investigated profiles are discussed in more detail in Section 4.4. The flow field was considered converged if the maximum magnitude of the relative change in the profile was less than 1%.

3. Literature Review

This chapter summarizes the current state of knowledge, as available in open literature, regarding fluid behaviour in mixing devices with respect to two general subjects. The first section will deal specifically with studies involving rotor-stator mixers, based on both laboratory experiments and computational simulations. The second section covers the behaviour of fluids in conventional stirred vessels. A wide range of literature is available on different aspects of fluid flow in stirred tanks, but the articles presented will deal primarily with comparisons between computational simulations and experimental results.

3.1. Rotor-Stator Mixers – Current Works

One of the earliest publications regarding the use of computational fluid dynamics to model a rotor-stator mixer was authored by Le Clair (1995). He conducted a two-dimensional simulation of the KADY Model 4C mill with working fluid similar to light paint (dynamic viscosity of 5000 cP and specific gravity of 1.3). No geometry- or mesh-related details were specified. At the time, it was common to analyze fluid flow through rotor-stator mixers analytically with velocity vector analysis of a free rotor. Le Clair argued that this technique was not adequate and highlighted a number of flow patterns that could not have been identified without CFD, such as impingement of flow onto the stator teeth and that part of the fluid exiting the rotor slot turns to go in the direction opposite of the rotation. Le Clair mentions that a high shear rate is observed in the shear gap, but does not provide any details.

Kevala (2001) conducted two-dimensional simulations of the IKA inline rotor-stator mixer used in the present work. A typical shear gap of 0.5 mm and a wider gap of 4 mm were considered. The standard k-ε turbulence model was used with standard wall functions. The work primarily focused on comparisons in the slot and volute between the RANS computational simulations and laser Doppler anemometry (LDA) measurements. Regarding the slots and volute, it was found that the RANS simulation results provided a good qualitative estimate of the velocity field at mid-plane. Quantitatively, however, the RANS results over-predicted velocities and turbulent kinetic energy compared to the LDA measurements. Kevala also found that, in the bulk of the shear gap, the shear rates were lower than the nominal shear rate. The shear rates near the rotor and stator walls were not discussed. He concluded that the shear rate in the shear gap was not a significant contributor to dispersion, but that a narrow shear gap was necessary increase the increase the strength of the impingement on the stator teeth. Kevala suggested that future increases in computational power would help to improve results by making more practical the use of more sophisticated and time-intensive models, elimination of wall functions, and three-dimensional geometry and flow.

Doucet et al. (2005) experimentally studied the behaviour of viscous fluids in batch rotor-stator mixers, based on a rotor-stator assembly manufactured by VMI-Rayneri consisting of a four-bladed impeller and slotted stator head, separated by a 1.5 mm shear gap. Both Newtonian and non-Newtonian fluids were examined. Doucet et al. focused on visualizing and quantifying hydrodynamic properties in the laminar and transition regimes. The pseudo-cavern phenomenon, associated the change in viscosity and consequent segregation of a non-Newtonian, shear-thinning fluid due to an open impeller, was shown to also exist for Newtonian fluids. The pseudo-caverns for Newtonian fluids scaled with the Reynolds number, while the pseudo-caverns of non-Newtonian fluids scaled with Re_y, the ratio of inertial forces of fluid motion to fluid yield stress. Power curves for the VMI-Rayneri assembly were also presented.

The Newtonian portion of the work of Doucet et al. was extended with transient three-dimensional CFD simulations by Barailler et al. In this study, the shear gap was 1.04 mm in width. Using POLY3D (enhanced with in-house features), torques, shear stresses, flow rates, and velocity fields were predicted for a number of low-rpm laminar cases. The existence of pseudo-caverns in the numerical simulation was confirmed. The shear stress was quantified as a function of rotor angle. It was found that the maximum shear stress, located at the rotor tip, agreed closely with the nominal shear stress.

Pacek et al. (2007) studied a Silverson L4RT rotor-stator mixer with a standard disintegrating head in an unbaffled tank using both FLUENT and LDA. The width of the shear gap was 0.175 mm, and the rotor speed was between 2,000 and 4,000 rpm. The FLUENT simulation was a three-dimensional model with sliding mesh interface. They examined the velocities and turbulence dissipation rates, and found that the radial velocity of the jets and the flow through the stator slots are proportional to rotor speed. LDA velocity measurements generally agree with the CFD predictions. For both rotor speeds, it was found that of 50% was of the total energy dissipation occurred within the swept area of the rotor, and only 7.5% is dissipated at the leading edge of the stator holes. For the 2,000 rpm case, 5.4% of the energy dissipation occurs in the shear gap, while for the 4,000 rpm case, the shear gap is responsible for 10.8% of the energy dissipation rate.

The greatest energy dissipation does occur at the leading edge of the stator holes, but only periodically when the rotor blade is closing with the leading edges.

The effect of stator geometry on flow patterns and energy dissipation rates was studied by Utomo et al. (2009). Utilizing the RANS equations, standard k-ε model, and enhanced wall functions, a Silverson L4RT rotor-stator mixer with three stator geometries (disintegrating head, slotted head, and square hole head) were simulated in FLUENT. The flow pattern in the stator holes was similar in that the fluid jet impinged onto the stator teeth and a circulation loop was created behind the jet. Larger holes resulted in longer jets. As holes became narrower, the circulation loops bent the jets and the energy dissipation rate became more uniform. It was also shown that power number was proportional to flow rate, which was proportional to the cross-sectional area of the stator holes. Predicted power numbers were approximately 10% and 20% lower than experimental values for hole head (disintegrating and square) and slot head, respectively.

The work of Yang (2011) focused on RANS simulations of rotor-stator mixers at different scales. A batch Silverson L4R mixer in an unbaffled tank was simulated using a novel hybrid technique that combined a sliding mesh simulation in the volume around the rotor with a steady multiple-reference frame simulation in the bulk volume of the tank. This greatly reduced computational time by eliminating the transient calculations in the volume of the tank for which the flow field is not periodic. Particle image velocimetry (PIV) measurements were used to validate the CFD results. The grid independence tests found that increasing the grid resolution across the 0.203 mm shear gap from 2 to 4 cells altered the velocity fields in the tank.

Yang (2011) also compared CFD simulations of three scales of inline rotor-stator mixers to investigate scale-up effects. Rotor tip speed and nominal shear rate were used as scale-up parameters because they are generally accepted to be the most critical scaling parameters. The three mixers simulated were of Silverson design: 1) inline L4R for bench scale, 2) 450LS for pilot scale, and 3) 600LS for plant scale. Flow fields, turbulent fields, and mean deformation fields were reported. It was found that the pilot- and plant-scale mixers, being of similar geometry, scaled reasonably with tip speed and nominal shear rate as scaling parameters. However, because the geometry of the L4R mixer was different than the larger mixers, scaling bench scale results to larger scales based on tip speed and nominal shear rate only could not be generally recommended. Volumetric flow rate per stator slot and power per slot were suggested as additional scaling parameters to consider in the scale-up process.

3.2. Stirred Tanks – Simulation and Experimentation

Bakker et al. (1997) simulated laminar flow within a stirred tank using the sliding mesh technique in FLUENT. Experimental measurement was also conducted using LDA. At low Reynolds numbers, simulation results and LDA data showed good agreement in the velocity fields and pumping number. It was observed that convergence of the flow field was fastest near the impeller and slowest in the rest of the tank. Convergence was also faster at lower Reynolds numbers.

Ng et al. (1998) compared sliding mesh results to LDA measurements in a baffled tank stirred by a six-blade Rushton impeller. LDA measurements were taken in the plane halfway between baffles in 1° intervals for one period of 60°. The sliding mesh simulations were conducted with the commercial package STAR-CD using the standard k-ε model and logarithmic wall functions. Half of the vessel was modelled, under the assumption that there would be repeated flow in 180°. It was found that agreement in the velocities and turbulent kinetic energies was good in most of the compared domain. However, the turbulent kinetic energy near the impeller blades was not well predicted. Given that this region is where much of the mixing was expected to take place, Ng recommended that additional improvements to the CFD model were needed.

A Chemineer P-4 impeller in a baffled tank was studied by Sheng et al. (1998). For the computational simulations with FLUENT, both the RNG k-ε and Reynolds Stress Model were used. A methodology for comparing CFD results to PIV data was presented. The use of PIV and LDA data to establish boundary conditions at the impeller (in terms of velocity, turbulent kinetic energy, and dissipation rate) was also investigated. It was concluded that correct boundary conditions were critical to the performance of the k-ε and RSM models. Mean velocity fields were well-predicted. Kinetic energy and turbulent energy dissipation were reasonably predicted at the impeller but under-predicted elsewhere.

Hartmann et al. (2004) used LES (with Smagorinsky and Voke subgrid-scale models) and RANS (with shear-stress-transport turbulence model) to simulate a baffled tank. The simulation results were compared to LDA measurements that were taken over the entire tank. The RANS simulations were found to yield a reasonably accurate flow field, but under-predicted turbulent kinetic energy near the impeller and in the discharge regions. LES better predicts the turbulent kinetic energy and also accounts for the anisotropic turbulence found in regions of high local shear.

A more extensive comparison between LDA and three numerical models (standard k-ε, Reynolds Stress Model, and Large Eddy Simulation as implemented in FLUENT 6.2) was conducted by Murthy & Joshi (2008) on a baffled vessel stirred by five impeller designs: a disc turbine, three pitched blade downflow turbines (60°, 45°, and 30°), and a hydrofoil impeller. It was found that results from the LES best matched the LDA measurements for all five turbines. RSM did not well-predict turbulent kinetic energy near impellers. The k-ε model also performed relatively poorly for four of the five impellers, suggested to be due to the overestimation of the eddy viscosity. The impeller with the lowest swirl, the hydrofoil impeller, achieved a satisfactory match with the LDA data for all three numerical schemes. Murthy & Joshi also reported on other observations from their work not directly related to their comparison of CFD models.

4. Operating Parameters and Computational Model

This section provides information about the operating scenarios and computational model. The operating parameters, fluid zones, reference frames, computational mesh, areas of investigation, convergence criteria, solution methods, and computational times associated with this work will be discussed.

4.1. Operating Scenarios

The two operating scenarios simulated in this study are summarized in Table 4.1. These variables are defined in Section 2.1. The first scenario is the *low operating scenario*, which has a relatively low rotor speed and inlet flow rate. The second scenario, referred to as the *high operating scenario*, is based on typical industry rotor speeds and process flow rates for similarly-sized rotor-stator mixers, and is more comparable to the experimental data previously acquired for the IKA prototype mixer. In both cases, the operating fluid was liquid water with constant density (ρ = 998.2 kg/m^3) and constant dynamic viscosity (μ = 1.003 cP). Note that the shearing numbers are of similar magnitude despite the different rotor speeds and flow rates.

Also, note that the low operating scenario has a shear gap Reynolds number of 1,100, which would be considered within the laminar regime in a simple channel flow. However, because of the periodic disruption of the flow pattern by the rotor, the flow in the shear gap may not be laminar at this Reynolds number. This is discussed in more detail in Chapter 6.

Table 4.1: Summary of Operating Scenarios

Variable	Description	Operating Scenario	
		Low	**High**
N	Rotor Angular Speed	300 rpm	1800 rpm
V_{tip}	Rotor Tip Speed	2.21 m/s	13.3 m/s
Q	Inlet Flow Rate	0.315 L/s	2.54 L/s
$\dot{\gamma}_{nom}$	Nominal Shear Rate	4,430 s^{-1}	26,600 s^{-1}
τ_{nom}	Nominal Wall Shear Stress	4.56 N/m^2	27.4 N/m^2
Re_{gap}	Shear Gap Reynolds Number	1,100	6,610
Re_{slot}	Stator Slot Reynolds Number	2,040	16,400
N_{sh}	Shearing Number	11.8	8.77

4.2. Fluid Zones and Interfaces

The model volume has three primary zones, referred to as the rotor, stator, and outlet zones. Each of these zones has properties that require a different meshing strategy and/or frame of reference. The zone definitions are illustrated in Figure 4.1.

The innermost zone is the rotor zone. It is comprised of the inlet pipe, all of the volume between the face of the rotor and the volute cover, and half of the shear gap. Hexahedral meshing was used exclusively in this zone. Using the sliding mesh technique to simulate the rotation of the rotor, the mesh rotates 0.5° per time step.

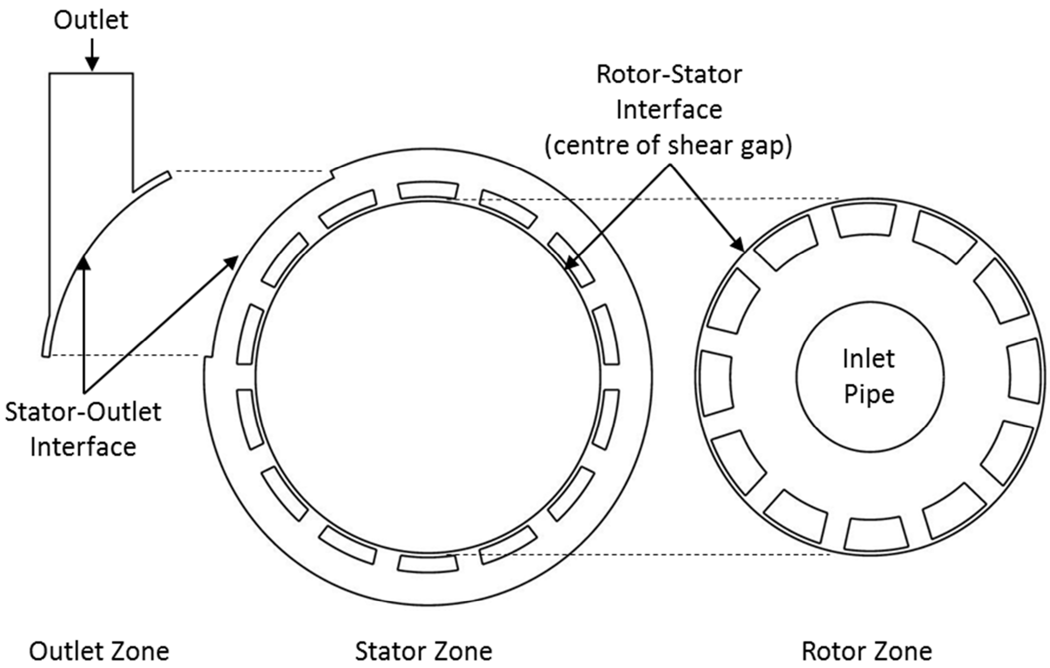

Figure 4.1: Exploded view schematic diagram of the IKA prototype mixer. Shown are the three primary fluid zones and their relative location in the computational model.

The stator zone includes half the volume of the shear gap, the volute, and the volume behind the rotor. This fluid zone was also meshed using hexahedrons only, but unlike the rotor, the stator zone is in a stationary reference frame.

The outlet zone includes the outlet pipe and a slice of the volute with which to create a rectangular interface area. The outlet zone is also in a stationary reference frame. Because of its complicated geometry, it was meshed with tetrahedral elements.

The interface between each zone is non-conformal, meaning that a direct one-to-one relationship between interface cells of the adjacent zones does not exist. This requires FLUENT to use an interpolation algorithm to calculate flow across the interface. Because of the rotation of the rotor zone, the relationship between rotor cells and stator cells at the interface must be re-evaluated at each time step.

4.3. Computational Grid

The computational grid was developed using ANSYS Workbench Meshing (Version 13). Because this study focuses on resolving the fluid behaviour in the shear gap, the grid was characterized primarily by the number and geometry of cells across the shear gap. This in turn is a significant influence on the total number of cells in the model because it is generally desired that the aspect ratio of cells (i.e., the ratio between the length of the longest side and the length of the shortest side) not exceed 10:1. As a result, when the number of cells within the shear gap is refined, this refinement propagates into the rest of the mesh.

Three levels of mesh refinement were studied for both of the operational scenarios in this project. The Level 1 mesh was considered as the baseline simulation in this project. It features eight cells across the shear gap (four cells in the rotor zone and four cells in the stator zone), providing the same degree of numerical resolution in the shear gap as previous rotor-stator mixer CFD simulations conducted by Kevala (2001) and Yang (2011). The Level 1 mesh contains a total of 2.8 million cells.

The Level 2 and 3 geometries were developed by applying the FLUENT's mesh adaption tool on the Level 1 mesh. The adaption tool splits each selected hexahedral cell into eight cells. FLUENT provides a number of methods to select cells for adaption, including distance from surfaces, value of gradients, and user-specified volumes. This technique was used to locally refine meshes near the rotor and stator walls.

The Level 2 mesh involved two stages of adaption. First, three-quarters of the cells in the shear gap were adapted, nearly doubling the number of cells across the shear gap. Second, an additional stage of adaption was applied to the three layers of cells closest to the rotor and stator walls, where the gradients were expected to be highest. The Level 2 mesh has 20 cells across the shear gap and a total of 10 million cells throughout the entire model. The Level 3 mesh has a third stage of refinement over the two layers of cells closest to the walls, resulting in 24 cells across the shear gap and a total of 24 million cells in the model.

Figure 4.2 presents schematics of the shear gap in the Level 1, Level 2, and Level 3 meshes for comparison. With the computing resources available to this project, the Level 3 mesh was the largest model that could be practically built, loaded, and run in FLUENT.

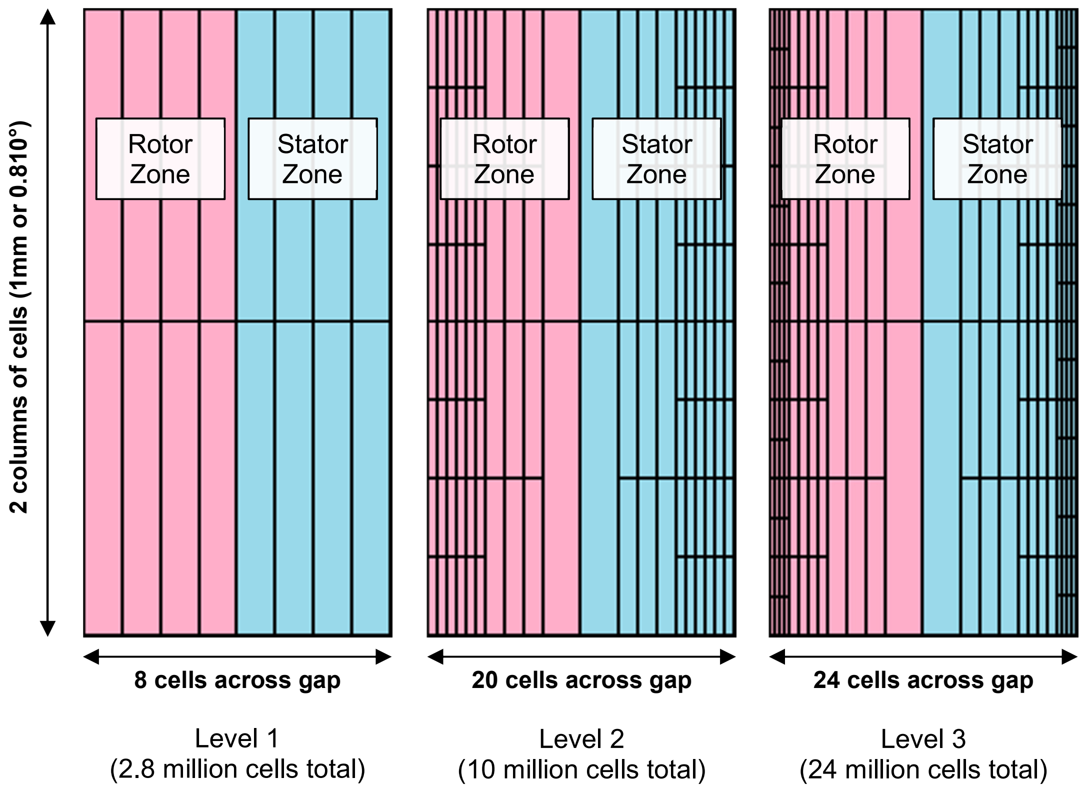

Figure 4.2: Schematics of mesh geometry across shear gap. The total number of cells in each simulation level is given in parentheses.

4.4. Areas of Investigation

Because the shear gap is a region of confined flow, the flow field in the shear gap was expected to depend on strongly on the rotor position and weakly on the physical position relative to the outlet. If these expectations hold true, then any surface within the shear gap can be considered as a representative condition. In this project, flow variables in two general regions "A" and "B", shown in Figure 4.3, were quantified. These regions were selected to complement an experimental study to evaluate a new sensor for the measurement of wall-shear stress, but this experimental work was cancelled.

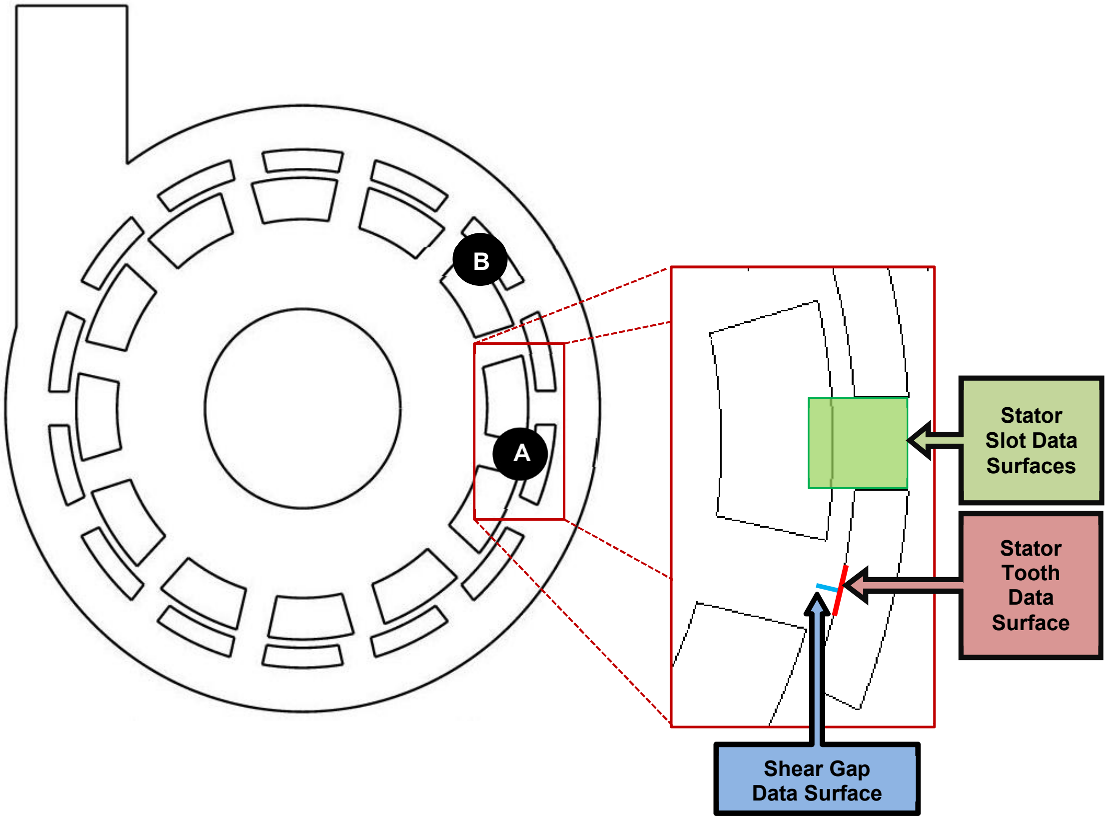

Figure 4.3: Location of interrogation surfaces in the IKA prototype model. The width of the shear gap has been exaggerated for illustration only.

At each region, four data surfaces were defined. These surfaces are illustrated in the inset diagram of Figure 4.3. An additional elevation view in Figure 4.4 shows both stator slot data surfaces and their relationship to the stator. The first two surfaces, in green in both figures, are planes through the stator slot at 1 mm and 7 mm depth. They extend from a radius of 67.5 mm (3 mm within the rotor slot) to 77 mm (the outer radius of the stator slot). Data surfaces were created at these depths for comparison to existing PIV measurements. The third surface, shown in blue in Figure 4.3 only, is a cross-section of the shear gap across its width (0.5 mm wide). The shear gap data surface extends to a depth of 18 mm. The fourth surface, the red region on the inner stator tooth surface in both figures, was used to collect near-wall flow properties. This surface is 6 mm x 6 mm.

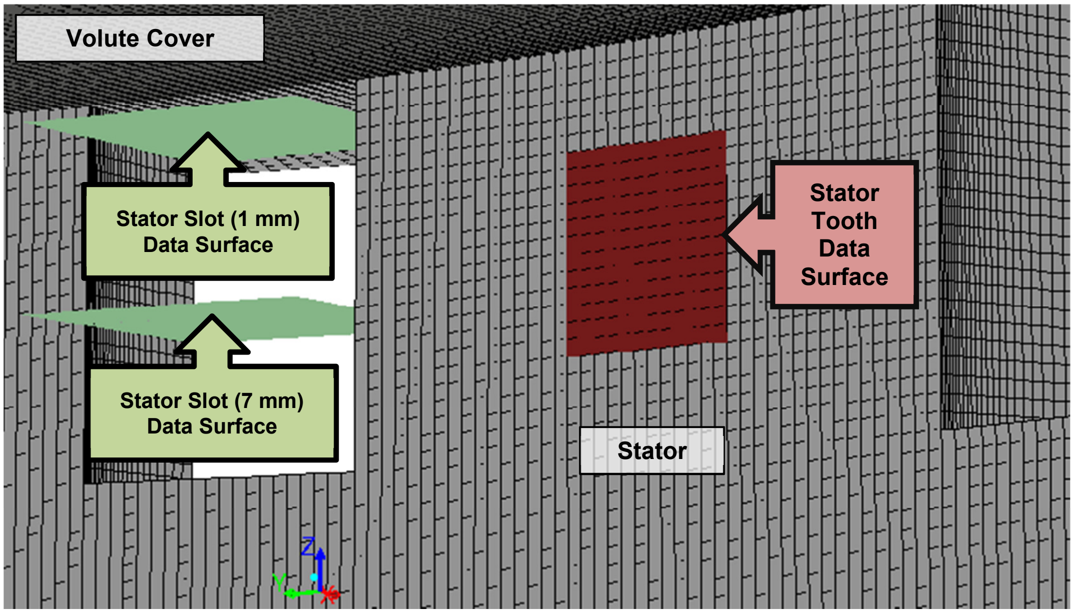

Figure 4.4: Image of stator slot and stator tooth data collection surfaces from the FLUENT model. View is from the inside the stator, with the rotor removed for clarity. The shear gap data surface is not shown.

The *stator slot data surfaces* were used to visualize flow behaviour in the slot via velocity vector diagrams and to quantify velocity profiles. The velocity profiles are defined by four parameters: the flow field property of interest, the depth of the profile, the displacement from the centreline, and the rotor position. In terms of flow field variables, velocity components (radial, tangential, and axial) and velocity magnitude were assessed. In terms of displacement from centerline and depth, velocity profiles were evaluated at the slot centreline and 3 mm to either side at depths of 1 mm and 7 mm, as shown in Figure 4.5. As noted previously, these depths were selected for comparison to existing PIV data.

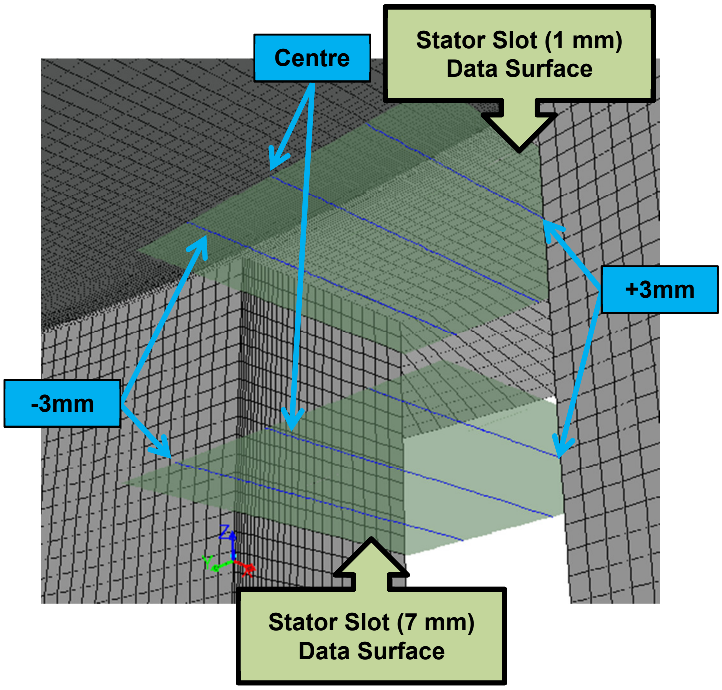

Figure 4.5: Magnified view of stator slot data surface from the FLUENT model. View is from the inside the stator, with the rotor removed for clarity.

The simulation results in the stator slots were examined for a mixture of rotor positions, with the rotor slot both open and closed; these rotor positions are illustrated in Figure 4.6. Rotor positions are identified by their deviation from the reference point 0°, in which the rotor slot is centered over the *shear gap data surface*. For example, +10° would indicate that the center of the rotor slot has rotated 10° clockwise (the direction of rotation). Because of there are twelve evenly-spaced rotor slots (i.e., a 30° period of rotation), converged flow solutions are time periodic and values at +10° and -20° should thus be identical.

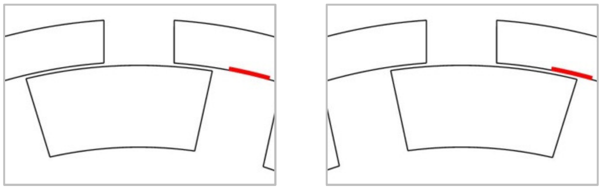

0° +5°

(a) Stator Slot Closed to Rotor Slot

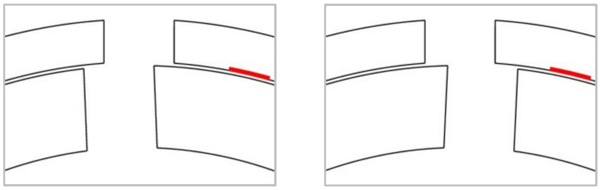

+15° (-15°) +20° (-10°)

(b) Stator Slot Open to Rotor Slot

Figure 4.6: Rotor positions for which velocities in the stator slots were examined. The stator tooth data surface is marked in the illustration for reference.

Instead of considering all of the velocity data from the shear gap data surface, the velocity field was quantified at specific depths and rotor positions. Velocity profiles on the shear gap data surface are defined by three parameters: the flow field variable of interest, the depth of the profile, and the position of the rotor. For the first parameter, radial, tangential, and axial velocity components, as well as the velocity magnitude were considered.

For the second parameter, five values of the depth from the volute cover (D_z) were examined: 3, 6, 9, 12, and 15 mm. These values were selected to span the shear gap data surface. For comparison, the stator slot is 12 mm deep, while the rotor slot is 10 mm deep with an additional 0.25 mm clearance between the volute cover and the top of the rotor (see Figure 1.2). Profiles at 3, 6, and 9 mm depths therefore experience strong periodic disturbances from the rotation of the rotor. At the lower two depths (12 and 15 mm), the shear gap is always bounded on one side by the moving surface of the rotor and on the other by the stator.

The third parameter is the rotor position. To evaluate the position-based periodicity of the flow, the six rotor positions shown in Figure 4.7 were examined. Three positions at +10°, +15°, and +20° (-10°) measure the velocity profile when the shear gap is confined by both the stationary stator wall and the moving rotor wall at all heights. The remaining three positions at -1.5°, 0°, and +2° quantify velocity profiles in which the shear gap (at depths down to 10.25 mm) is not confined by the rotor tooth. Note that the location of the shear gap data surface is indicated by the downward pointing angle on each illustration.

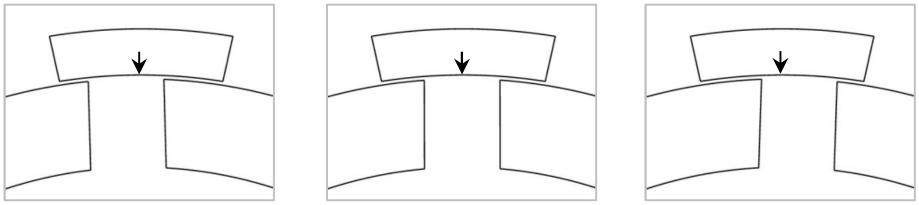

-1.5° **0°** **+2°**

(a) Shear Gap Unconfined by Rotor Tooth (down to 10.25 mm)

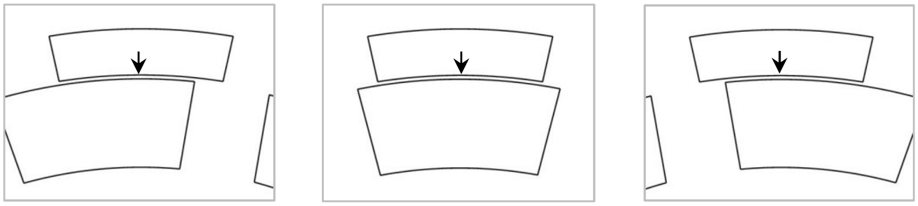

+10° (-20°) **+15° (-15°)** **+20° (-10°)**

(b) Shear Gap Confined by Rotor Tooth

Figure 4.7: Rotor positions for which velocity profiles in the shear gap were examined. The location of the shear gap data surface on the stator tooth is marked with an arrow.

With three velocity components and velocity magnitude, five depths, and six rotor positions, one hundred twenty different shear gap velocity profiles were examined at each region ("A" and "B") and operating scenario. When plots of velocity profile across the shear gap are presented, the left side of the plot will represent the inner side of the shear gap (i.e., the outer radius of the rotor at r = 70.5 mm). The right side of the plot will represent the outer side of the shear gap (i.e., the inner surface of the stator at r = 71 mm). Reported velocities are normalized to the rotor tip speed. This convention, as applied to the Level 2 mesh, is illustrated in Figure 4.8.

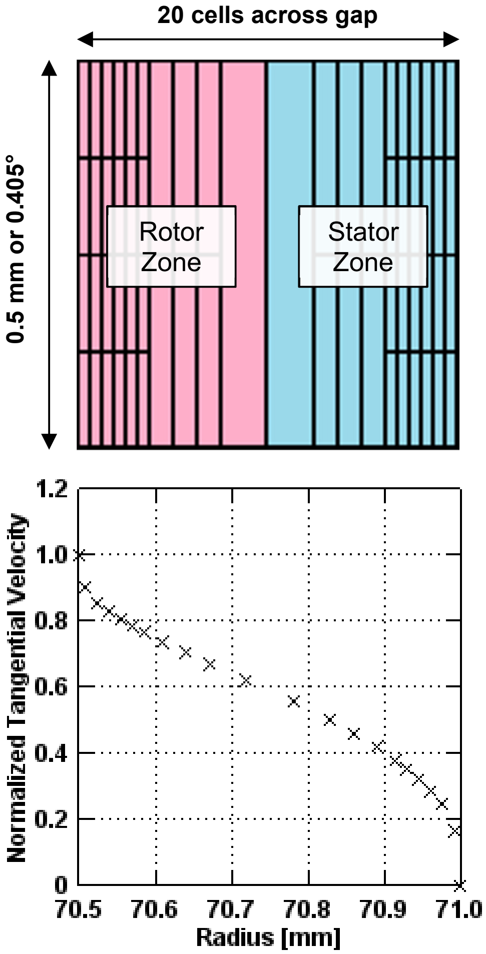

Figure 4.8: Sample velocity plot to illustrate plot conventions.

In addition to the specific surfaces discussed above, the energy dissipation rates were quantified for each fluid zone (see Figure 4.1). These are based on the volume integrals of the square of total deformation rate and the turbulence dissipation rate reported directly by FLUENT.

Note that numerical data from the shear gap at region "B" was found to be similar in magnitude and trend to the data from region "A"; therefore, this work presents results from Region "A" only. A sample comparison of the tangential velocity profile on the shear gap data surfaces (Figure 4.3 shows the location of the region "A" shear gap data surface) is presented in Figure 4.9. For the 15° (right-side plots), the velocity profiles are nearly identical for both scenarios. At 0°, the velocity profiles follow similar trends, although there are some minor differences in the values. This data provides some support for the claim that the flow field in the shear gap is not strongly location-dependent.

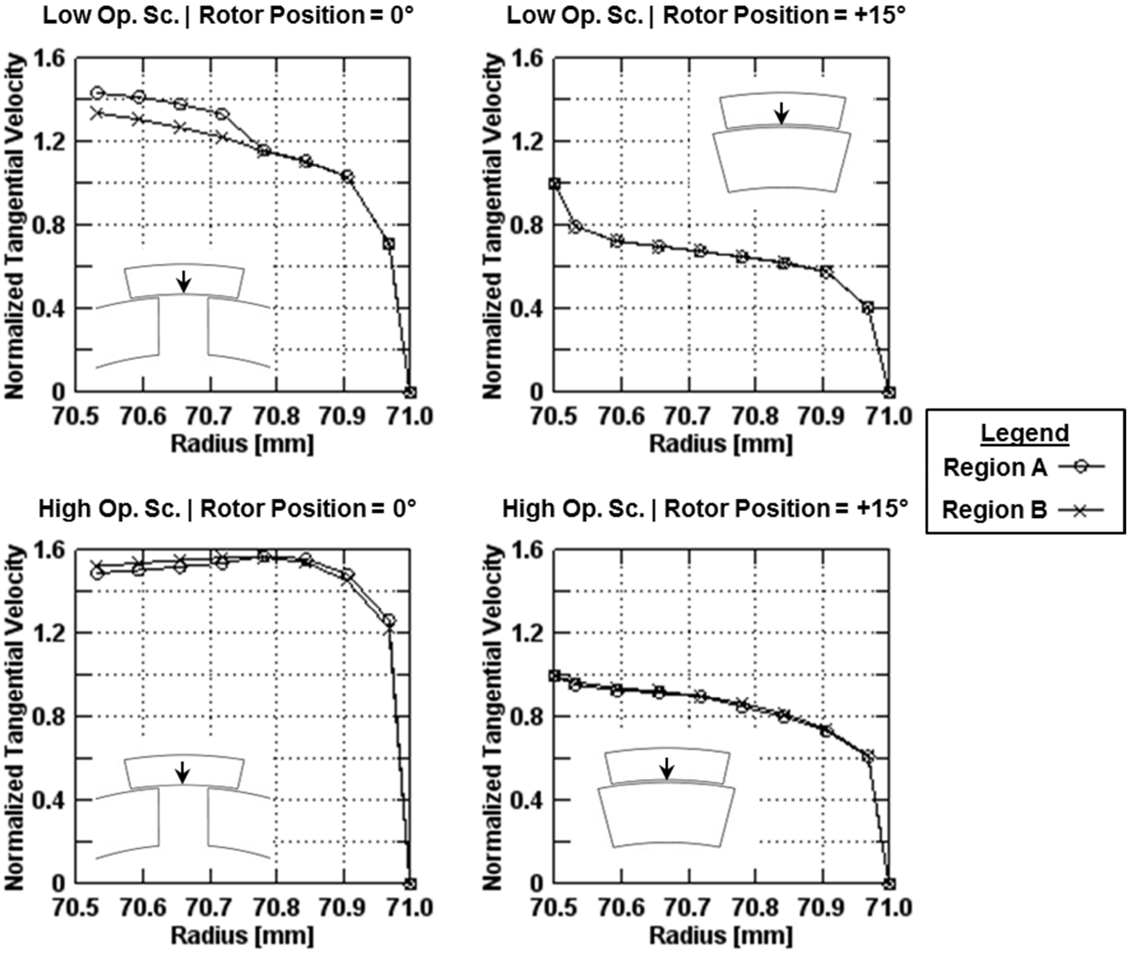

Figure 4.9: Comparison of sample velocity profiles from Regions "A" and "B" at $D_z = 6$ mm for low operating scenario ($N = 300$ rpm, $Q = 0.315$ L/s) and high operating scenario ($N = 1800$ rpm, $Q = 2.54$ L/s) with Level 1 mesh.

4.5. Initialization and Convergence

The initial flow solution, with which the Level 1 mesh was started, was developed in two stages. First, a steady-state, multiple-reference-frame (MRF) simulation (see Section 2.8 for more information) was conducted on a coarse preliminary mesh. This technique yields a reasonable first approximation for the flow field in areas away from the high shear region. In the second stage, the sliding mesh was activated. In this work, 20 rotor revolutions were simulated on this coarse grid for each operating scenario, after which a majority of the flow field appeared to have reached convergence. Generally, the flow field in regions that are tightly confined (such as the shear gap) and regions closest to the inlet converge the most quickly, while the outlet zone flow field converges more slowly.

The output from the coarse preliminary mesh was read into the Level 1 mesh to initialize the flow field for this baseline simulation. Each more sophisticated level of model was initialized with the converged flow field from the model immediately prior. In other words, the Level 2 mesh was initialized with the Level 1 converged solution and the Level 3 mesh was initialized with the Level 2 converged solution. Successively transferring the solution from coarser to more refined meshes reduces the overall computational time while maintaining the quality of the final solution.

The numerical measures of convergence are discussed in detail in Section 2.12. As a brief summary, two types of convergence were considered in this project. First, the iteration convergence at each time step is quantified by the residual of each transport equation. The solver proceeds to the next time step with the residual of the continuity equation is less than 10^{-4} and the residuals for the remaining transport equations (momentum, turbulent kinetic energy, and turbulence dissipation rate) are less than 10^{-5}. Second, the flow field convergence is achieved when the flow field becomes periodic with rotor position. In this project, the flow field convergence was gauged by quantifying the relative change (Equation 2.12-3) of velocity and deformation rate profiles between two periods. Convergence was considered to be achieved when the maximum relative change was less than 0.01 or 1% between two successive periods.

4.6. Summary of Solution Methods

Below is a summary of the models used in all simulations, as provided and implemented in FLUENT. These are described in more detail in Chapter 2.

- Realizable k-ε turbulence model with non-equilibrium wall functions
- Green-Gauss cell-based gradient evaluation
- Second order discretization for pressure
- Second order upwind discretization for momentum, turbulent kinetic energy, and turbulence dissipation rate.
- Second order implicit for time
- PISO pressure-velocity coupling scheme with uncoupled neighbour and skewness correction.

4.7. Computing Resources and Computational Time

The IKA prototype mixer was simulated on 16 nodes, primarily on a cluster powered by four Intel Xeon E5620 processors. The Xeon E5620 is a quad-core processor with each core operating at 2.40 GHz, with 8 GB of RAM available to each core.

Table 4.2 summarizes the mesh characteristics and their approximate computational time per revolution.

Table 4.2: Summary of Mesh Sizes and Computational Times

Mesh Level	Mesh Size Metrics		Approximate Iterations per Time Step	Approximate Computational Time [hr/rev]
	Cells Across Shear Gap	Total Number of Cells		
1	8	2.8 million	50	32
2	20	10 million	70	200
3	24	24 million	100	720

4.8. Reporting Results and Revolution Naming Conventions

The results of the grid independence study are discussed in Chapter 5. For each operating scenario, velocities and deformation rates on the data surfaces described in Section 4.4 will be investigated at all three mesh levels. The intent of this study is to determine at which mesh level the flow solution becomes grid independent.

Chapters 6 and 7 present detailed results of the low and high operating scenarios, respectively. The results are from the smallest grid for which grid independence can be established, as determined in Chapter 5.

Particularly when discussing flow field convergence (see Sections 2.12 and 4.5), there is a need to establish a naming convention to identify the source of the data in terms of time. With twelve evenly-spaced rotor teeth, it is convenient to separate data into discrete sets based on revolutions and periods. Considering that the rotor is rotated 0.5° each time step, a data set for a complete 30° period is 60 time steps. The initial condition (i.e., when the flow field is read into the mesh) will be referred to as "Revolution 1, Period 1”, with a shorthand notation of “R1-P1”. The first 60 time steps are stored in a data set labelled “R1-P1”, the second 60 time steps are stored as “R1-P2”, etc. Since flow field convergence is only evaluated between periods of the same mesh level, this counter is reset for each mesh level.

5. Grid Independence Study

A primary objective of this project is to establish the level of mesh refinement needed to resolve important flow features and produce a grid-independent solution. Both the low (N = 300 rpm, Q = 0.315 L/s) and high (N = 1800 rpm, Q = 2.54 L/s) operating scenarios for three mesh levels. The baseline Level 1 consists of 8 uniform cells across the shear gap and has a total of 2.8 million cells in the model. The Level 2 mesh has a total of 10 million cells in the model, and it featured 20 cells across the shear gap, with cells closer to the wall being smaller than cells near the center of the shear gap. The Level 3 gap had even greater refinement in the near-wall regions, with 24 cells across the shear gap and 24 million cells in the entire simulation.

Before comparing the simulation results from different mesh levels, the flow field convergence is assessed separately for each combination of operating scenario and mesh level. To quantify flow field convergence, the relative change (Equation 2.12-3) of velocity profiles in the stator slot and shear gap as well as total deformation rate profiles on the stator tooth surface are evaluated at representative locations for different revolutions and periods (see Figure 4.3 for the location of the data surfaces and Section 4.8 for convention for revolution-period notation). The flow field is considered to be converged when the maximum relative change between two successive periods is less than 1%.

To identify grid independence, aspects of the converged flow field for the three levels of increasing mesh refinement are examined at representative locations. A flow solution is considered grid independent when further refinement of the mesh does not change the flow field variables. This change (or difference) is again quantified as relative change (Equation 2.12-3). The final models, from which the results in Chapters 6 and 7 are developed, are selected based on the observed degree of change in the flow field with increasing grid resolution and the required simulation time.

5.1. Convergence of Low Operating Scenario

The convergence of the flow field in the stator slots was quantified by examining the velocity components, velocity magnitude, and total deformation at the six data lines illustrated in Figure 4.5. The locations of the stator slot data surfaces are shown in Figure 4.3. The rotor is at the 0° position in all profiles, in which the stator slot is blocked by a rotor tooth (see Figure 4.6).

Figure 5.1 presents a comparison of selected velocity magnitude profiles for the R3-P1 and R3-P7 periods of the baseline Level 1 simulation for the low operating scenario. Each line represents the velocity magnitude (normalized to rotor tip speed) through the centreline of the stator slot between the outer radius of the rotor (r = 70.5 mm) and the outer radius of the stator slot (r = 77 mm). The velocity magnitude profiles at a depth of 1 mm (near the volute cover) for R3-P1 and R3-P7 are shown with square and cross markers, respectively. The corresponding profiles at 7 mm depth (near the midplane of the stator slot) for R3-P1 and R3-P7 are shown with circle and 'X' markers. Figure 5.1 shows that the velocity profiles are qualitatively similar.

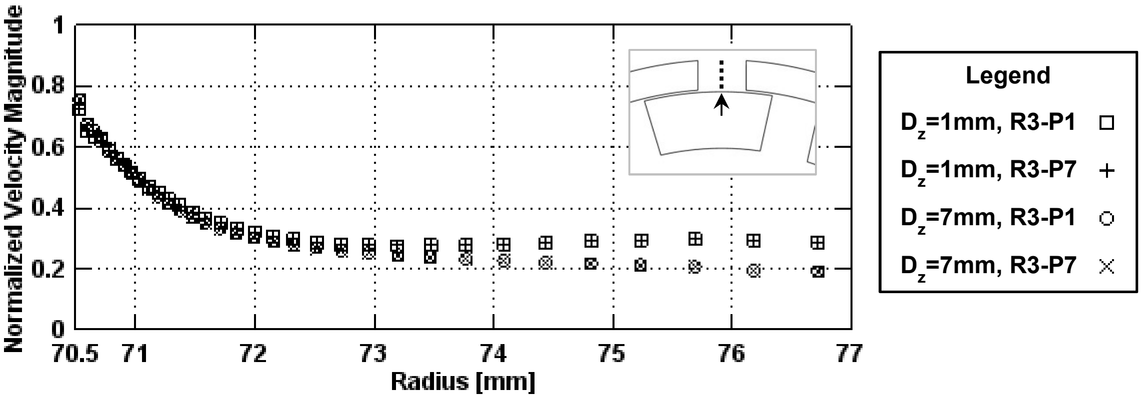

Figure 5.1: Velocity magnitude profiles in the stator slot for the low operating scenario ($N = 300$ rpm, $Q = 0.315$ L/s) with the Level 1 mesh. The arrow and dotted line indicate the location of the profiles. Velocity profiles for both periods are qualitatively similar.

The quantitative difference in the Level 1 velocity magnitude profiles between R3-P1 and R3-P7, expressed as relative change, is shown in Figure 5.2. The corresponding relative change plots for the Level 2 and Level 3 meshes are also shown. In all cases, the relative change in velocity magnitude from the first period to the second is less than 1%, so the flow in the stator slot is judged to be converged for all simulations.

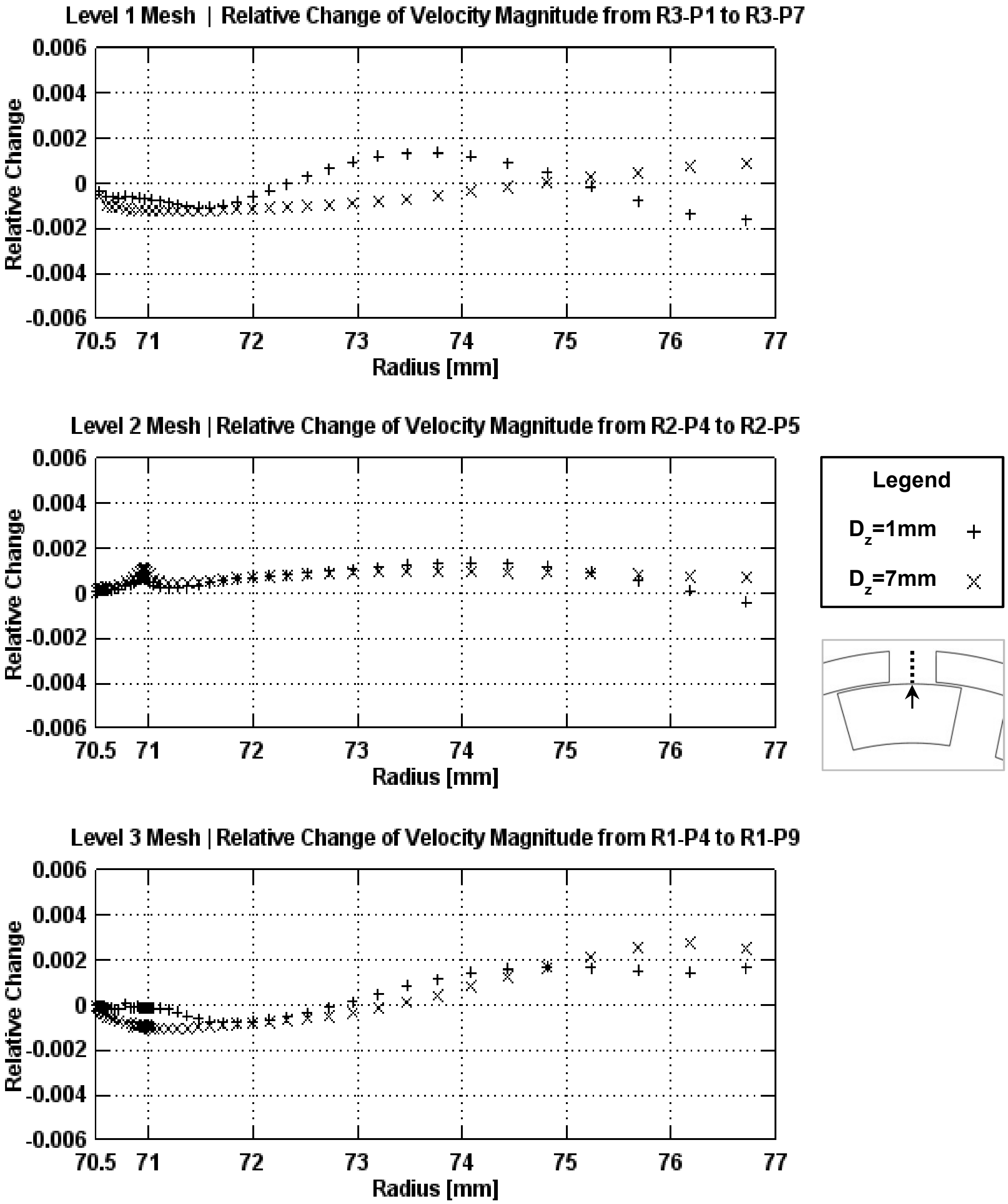

Figure 5.2: Relative change in velocity magnitude in the stator slot for the low operating scenario ($N = 300$ rpm, $Q = 0.315$ L/s) with the Level 1, 2, and 3 meshes. The arrow and dotted line indicate the location of the profiles.

The tangential velocity profiles within the shear gap at selected depths and rotor positions are shown in Figure 5.3 for the low operating condition with Level 1 mesh. The location of the data surface is indicated by the arrow in the inset (see Figure 4.3 for more details) The first plot reports four tangential velocity profiles (normalized to the rotor tip speed) across the shear gap for R3-P1: 1) rotor position of 0° and depth of 6 mm (midplane of the stator slot), 2) rotor position of 0° and depth of 15 mm, 3) rotor position of 15° and depth of 6 mm, and 4) rotor position of 15° and depth of 15 mm. The second plot shows the velocity profiles of the same four configurations at R3-P7, half a revolution later. As with the stator slot velocity profiles shown in Figure 5.1, the tangential velocities are observed to be qualitatively similar.

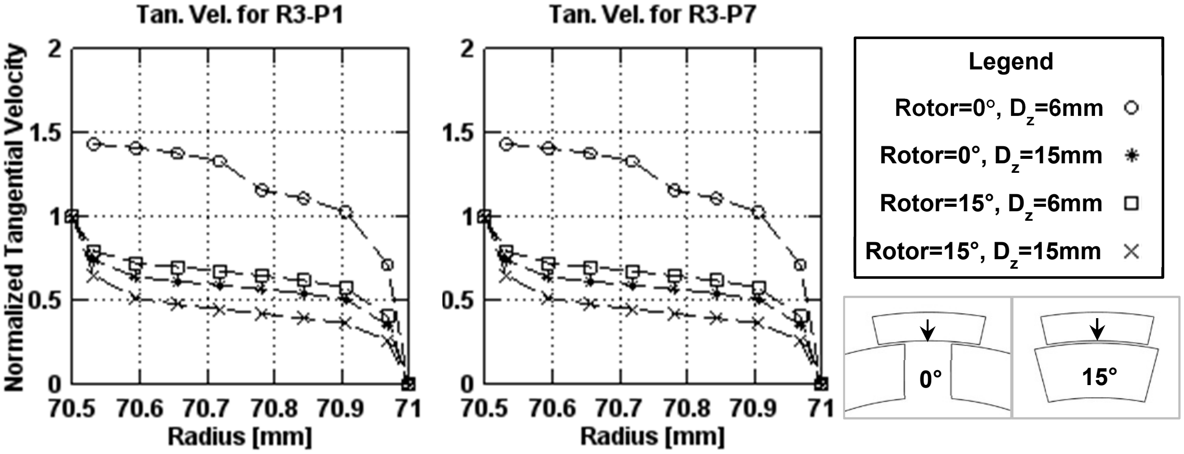

Figure 5.3: Tangential velocity profiles in the shear gap for the low operating scenario (N = 300 rpm, Q = 0.315 L/s) with the Level 1 mesh. The arrow indicates the location of the profiles.

Figure 5.4 shows the relative change in each of the four velocity profiles discussed above for all three mesh levels. The relative changes are on the order of 0.001 (0.1%) over a number of periods, much less than the 1% flow field convergence threshold. The maximum relative changes (as absolute values) are 0.041%, 0.060%, and 0.055% for the Level 1, 2, and 3 meshes. By comparison, consider the relative changes in the stator slot (see Figure 5.2). For the stator slot velocity profiles, maximum relative changes (as absolute values) of 0.16%, 0.14% and 0.27% are observed for the Level 1, 2, and 3 meshes, respectively. The higher relative changes in the stator slot are expected to be due to the larger width of the stator slot (compared to the shear gap) and the connection to the much-larger volute. It can be concluded that the flow larger less-confined regions converge more slowly than fluid in strongly-directed regions like the shear gap.

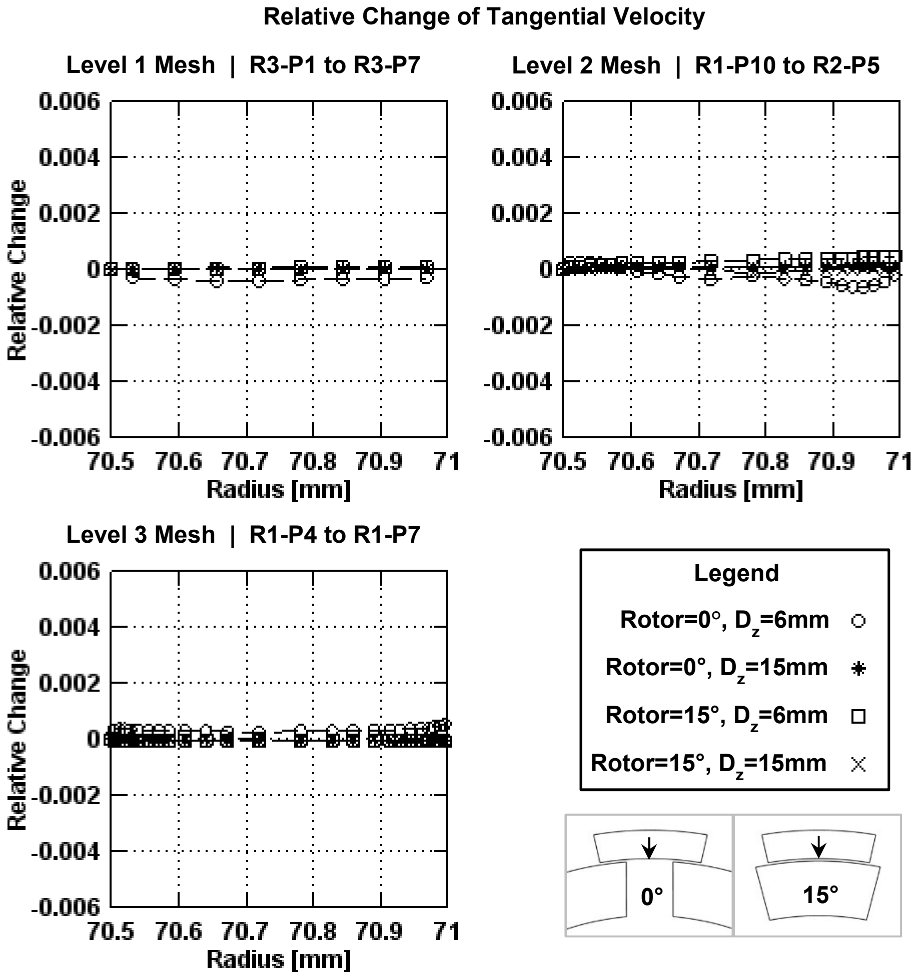

Figure 5.4: Relative change in tangential velocity in the shear gap for the low operating scenario (N = 300 rpm, Q = 0.315 L/s) with the Level 1, 2, and 3 meshes. The arrow indicates the location of the profiles.

Figure 5.5 compares total deformation on the Level 1 mesh of the low operating scenario for two periods (R3-P1 and R3-P7). The stator tooth data surface, located in the centre of the stator tooth (as shown in Figure 4.3), is comprised of 144, 2304, and 9216 cells for the Level 1, 2, and 3 meshes, respectively. Unlike the velocity profiles discussed previously, the convergence of total deformation rates is evaluated with respect to rotor position (or equivalently time). The dotted line indicates the mean total deformation rate based on all data surface cells, while the dashed lines represent the maximum and minimum predicted total deformation rates for any one data surface cell.

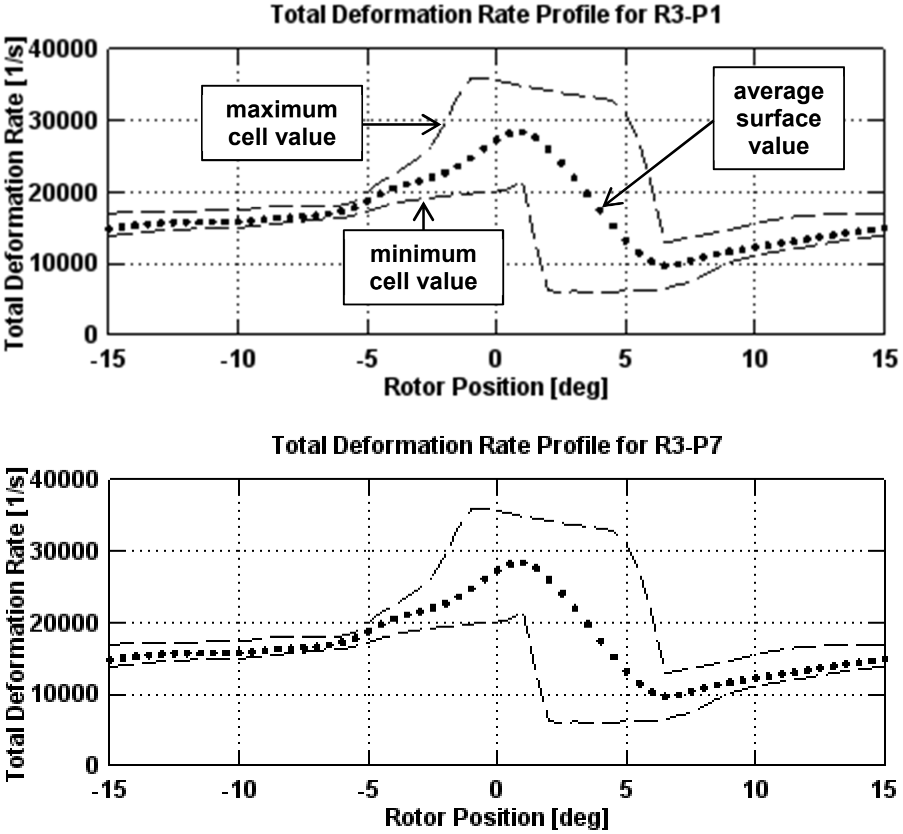

Figure 5.5: Total deformation rate profiles on the stator tooth for the low operating scenario (N = 300 rpm, Q = 0.315 L/s, $\dot{\gamma}$ = 4,430 s^{-1}) with the Level 1 mesh.

The relative change of the total deformation rate profiles shown in Figure 5.5, as well as for corresponding total deformation rate profiles for the Level 2 and 3 meshes, are presented in Figure 5.6. For all three mesh levels, the maximum relative change is less than the 1% flow field convergence threshold, indicating that the total deformation rate at the shear gap walls has reached a periodic steady state.

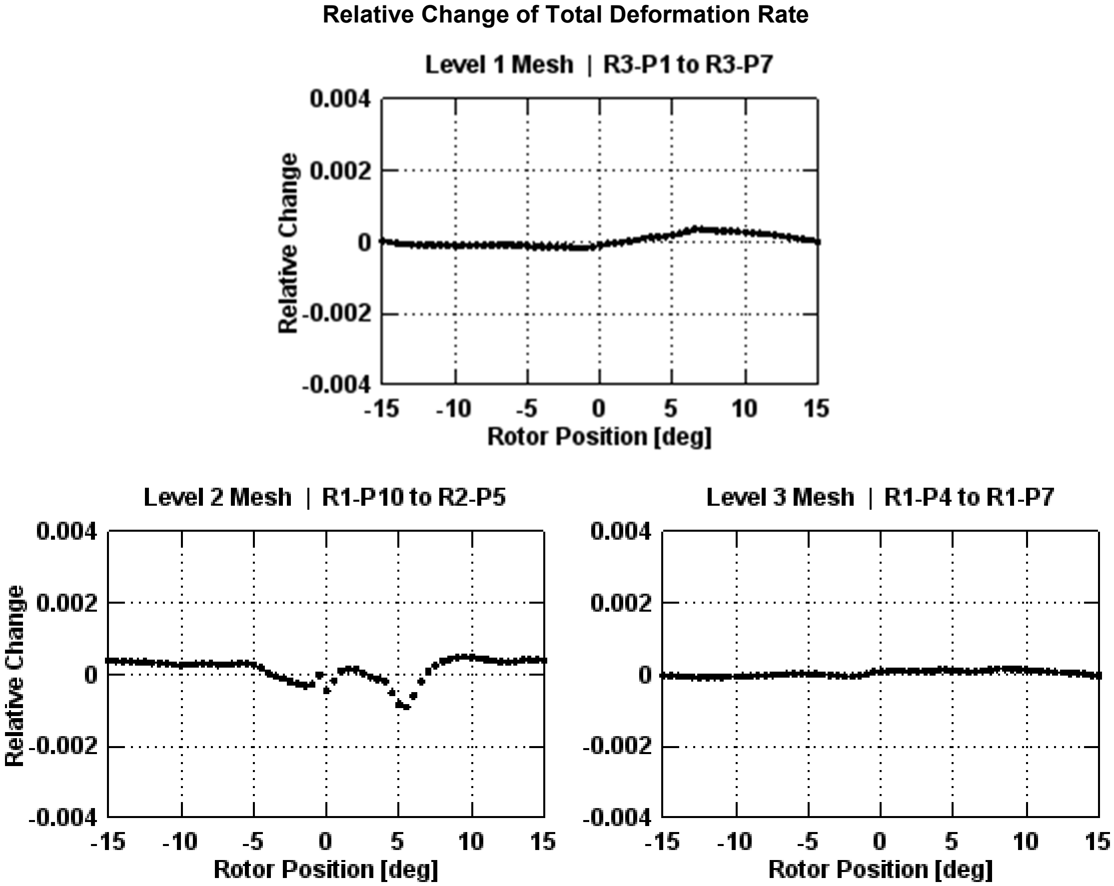

Figure 5.6: Relative change in total deformation on the stator tooth for the low operating scenario (N = 300 rpm, Q = 0.315 L/s, $\dot{\gamma}$ = 4,430 s^{-1}) with the Level 1, 2, and 3 meshes.

In summary, the simulations of the low operating scenario for all three mesh levels meet the flow field convergence criterion and are therefore judged to be converged. The relative changes of the shear gap velocity and total deformation rate profiles are generally lower than the relative changes calculated for the stator slot velocity profiles, from which it can be concluded that more-confined regions, such as the shear gap, reach convergence more quickly than less-confined regions.

5.2. Grid Independence for Low Operating Scenario

Qualitatively, grid independence in the stator slot was established by looking at plots of velocity vectors at the stator slot data surfaces. As shown in Figure 4.5, the stator slot data surfaces are located at depths of 1 mm and 7 mm. The rotor is at the 0° position (see Figure 4.6). Each fixed-length vector in the vector plot originates at a computational cell and points in the direction of the predicted flow. The colour of the vector is based on the velocity magnitude, as per the scales. The rotation direction of the rotor is clockwise.

The velocity fields for the different mesh levels are compared at a depth of 1 mm in Figure 5.7 and a depth of 7 mm in Figure 5.8 for the low operating scenario. The fluid behaviour does not appear to be qualitatively dependent on the refinement of the mesh in and near the shear gap.

Figure 5.9 provides a quantitative comparison of the velocity magnitude profiles at the centre line of both stator slot data surfaces (see Figure 4.5) between each mesh level for the low operating scenario. Level 1, 2, and 3 profiles are denoted with square, cross, and circle markers, respectively. The plots show that the velocity profiles do not depend significantly on the mesh refinement.

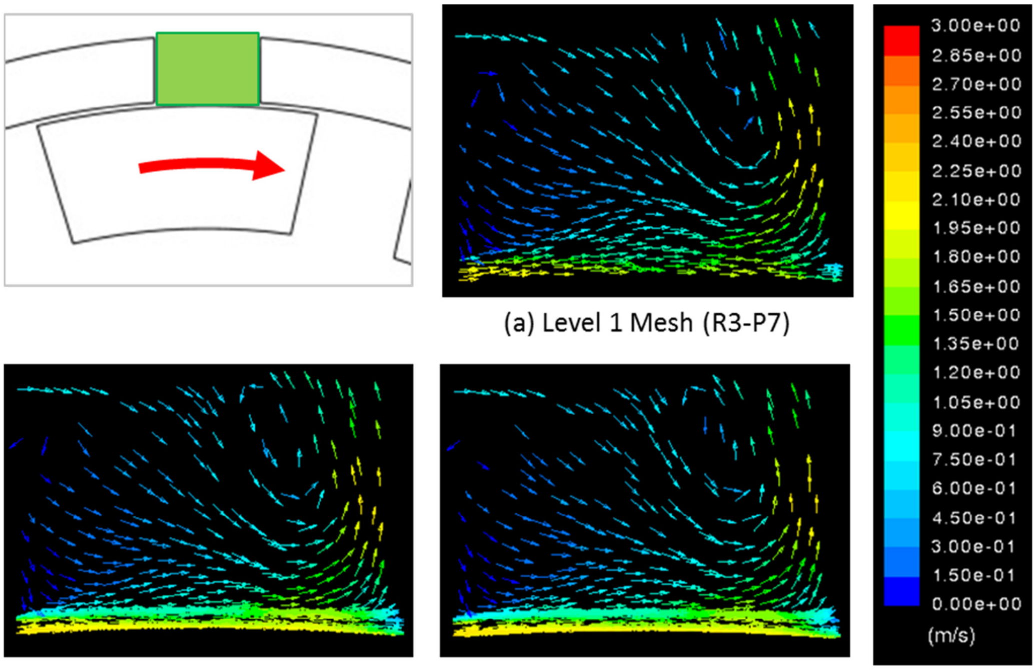

(a) Level 1 Mesh (R3-P7)

(b) Level 2 Mesh (R2-P5)

(c) Level 3 Mesh (R1-P9)

Figure 5.7: Comparison of velocity vectors in stator slot for Level 1, Level 2, and Level 3 meshes at depth of 1 mm for low operating scenario (N = 300 rpm, Q = 0.315 L/s).

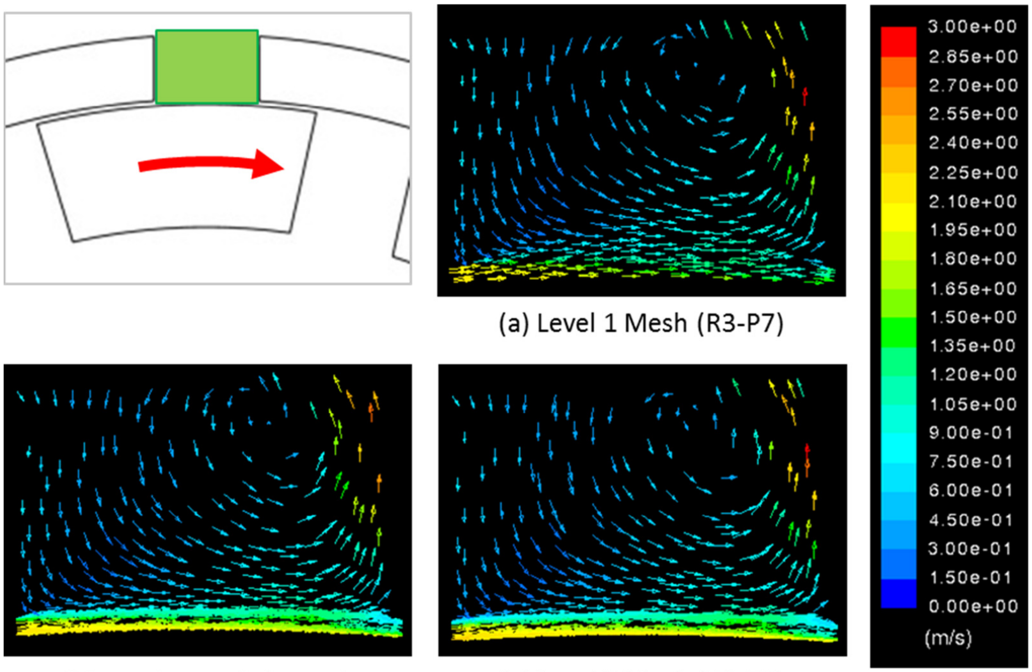

(a) Level 1 Mesh (R3-P7)

(b) Level 2 Mesh (R2-P5)

(c) Level 3 Mesh (R1-P9)

Figure 5.8: Comparison of velocity vectors in stator slot for Level 1, Level 2, and Level 3 meshes at depth of 7 mm for low operating scenario (N = 300 rpm, Q = 0.315 L/s).

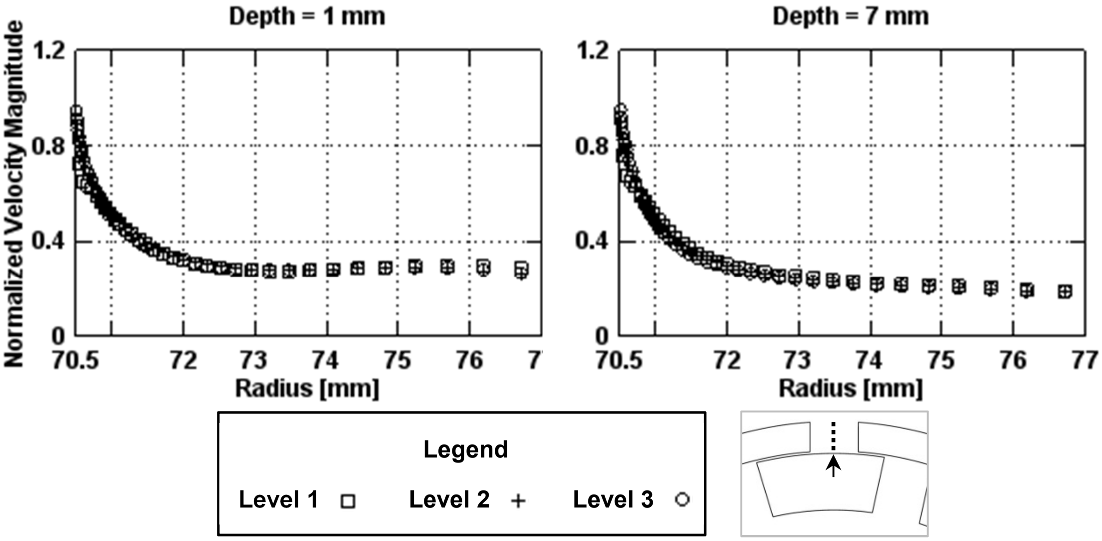

Figure 5.9: Comparison of velocity magnitude in stator slot at depths of 1 mm and 7 mm between Level 1, Level 2, and Level 3 meshes for the low operating scenario (*N* = 300 rpm, *Q* = 0.315 L/s). The arrow and dotted line indicate the location of the profiles.

To evaluate grid independence in the shear gap for the low operating scenario, tangential velocity profiles were compared between the Levels 1, 2, and 3 meshes. Figure 5.10 present the tangential velocity profiles at a depth of 6 mm. Comparison plots for other depths are provided in Appendix A. Level 1, 2, and 3 mesh profiles are denoted with 'X', circle, and triangle markers, respectively. The tangential velocities are normalized with the rotor tip speed. Rotor positions are given in the title of each plot and in the inset illustration.

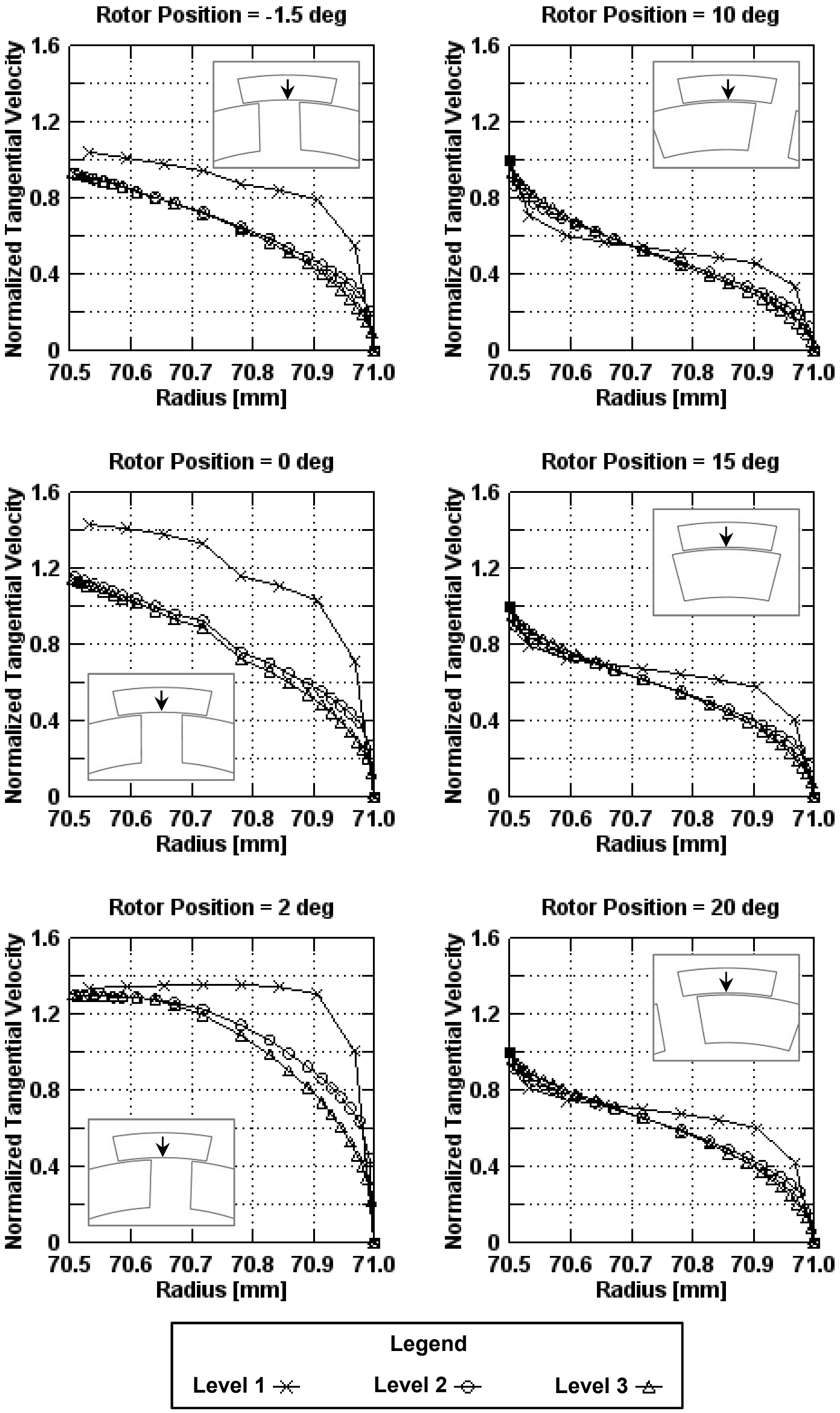

Figure 5.10: Comparison of tangential velocity in the shear gap between Level 1, Level 2, and Level 3 meshes for the low operating scenario ($N = 300$ rpm, $Q = 0.315$ L/s). All profiles are at a depth of 6 mm. The arrow indicates the location of the profiles.

Figure 5.10 shows that a significantly lower tangential velocity is predicted with the more-refined Level 2 and Level 3 meshes when the shear gap is not confined by the rotor tooth. Because of this velocity difference, predictions of volumetric flow rate of fluid through this section of the shear gap would be higher with the Level 1 mesh than with the Level 2 and 3 meshes. On the other hand, when the shear gap is confined by both the stator and rotor walls, the average velocity for the Level 1 solution appears to be only slightly higher than the Level 2 and 3 solutions. In both unconfined and confined positions, the Level 2 and Level 3 solutions are comparable.

The total deformation rates on the stator tooth (see Figure 4.4) for the Levels 1, 2, and 3 meshes are compared in Figure 5.11. The first plot shows the mean total deformation rate on the stator tooth data surface as a function of time and mesh level. The second plot shows the relative change from Level 1 to Level 2 with a circle marker and from Level 2 to Level 3 with a triangle marker. From Figure 5.11, it is observed that the Level 2 solution has a substantially different deformation rate profile than the Level 1 solution, with an average relative difference is 74%. The relative change between the Level 3 and Level 2 meshes, however, is only an average of 2.4%. This indicates that the additional refinement for the Level 3 mesh does not have a significant impact on the total deformation rates inside the shear gap for the low operating scenario.

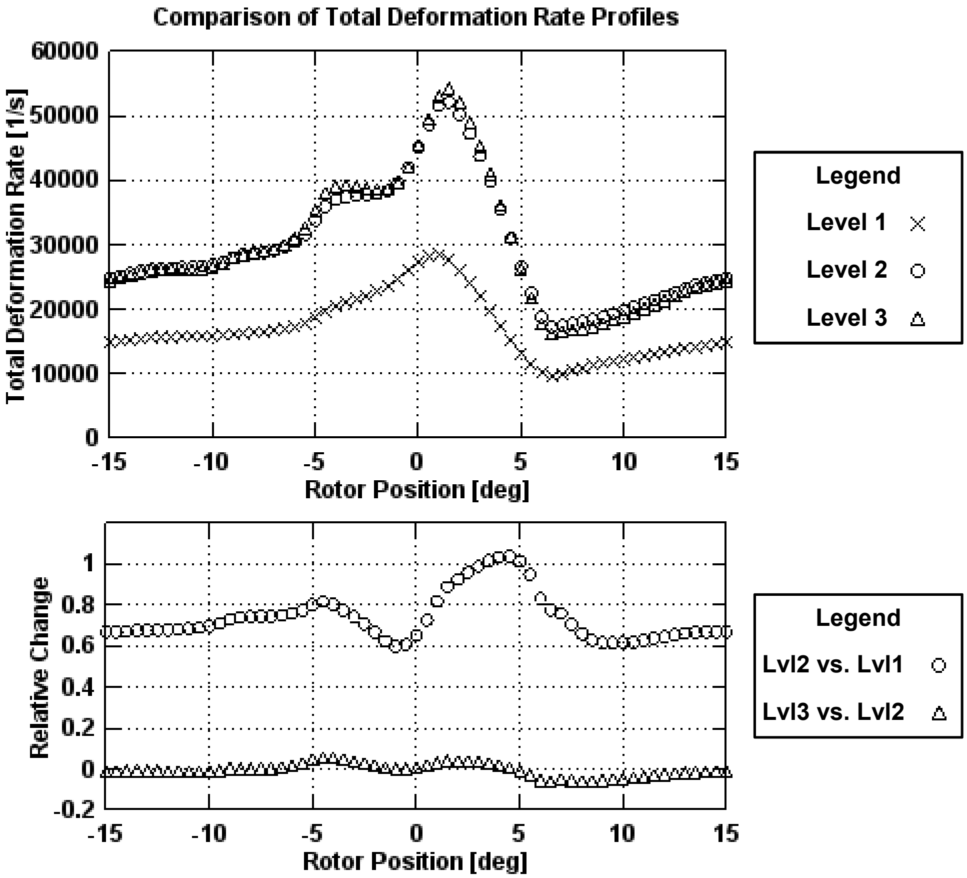

Figure 5.11: Comparison of total deformation rate on the stator tooth between Level 1, Level 2, and Level 3 meshes for the low operating scenario ($N = 300$ rpm, $Q = 0.315$ L/s, $\dot{\gamma} = 4{,}430\ \mathrm{s}^{-1}$).

5.3. Summary of Grid Independence for Low Operating Scenario

All simulations were shown to have converged through quantifying the relative change of velocity magnitude in the stator slot, tangential velocity in the shear gap, and total deformation rate on the stator tooth. It was found that flow field convergence for both shear gap velocity and stator tooth total deformation rates was relatively fast because this region is confined and strongly directed by the rotor. The convergence of velocity in the stator slot was slower due to its larger size and connection to the volute.

While the velocities in the stator slot were found to be similar for all three mesh levels, a definite difference in the profiles of both shear gap velocities and total deformation rates was seen between the Level 2 solution and the baseline Level 1 solution. The Level 2 tangential velocities in the shear gap were generally predicted to be lower than the corresponding Level 1 values when data surface was not confined by the rotor tooth. The Level 2 shear gap velocity profile pattern, when confined by both rotor and stator walls, was closer to the nominal shape expected of plane Couette flow. The magnitude of the total deformation rate on the stator tooth of the Level 2 solution is about 74% higher than in the Level 1 solution.

Comparisons of Level 2 and Level 3 solutions show only minor differences in profiles of total deformation rate and tangential velocity. Given the increased computational complexity of the Level 3 mesh, the Level 2 mesh was deemed to be suitable to model the low operating scenario.

The simulation results for the low operating scenario with Level 2 mesh (presented in previous sections and Chapter 6) are based on about 24 revolutions of the rotor (starting from a converged MRF flow field). However, judging from the low relative changes in stator slot velocity, shear gap velocity, and stator tooth total deformation rate that were presented in Section 5.1, the required number of revolutions may be less, depending on a number of factors. The most important factor is the region of interest. In a strongly-directed region like the shear gap, a converged flow solution (in terms of shear gap velocities and stator tooth deformation rates) may need about 12 revolutions. However, if flows within the stator slot are of interest, then 20 revolutions may be needed. Another factor is the computational strategy. In this project, a series of grids with successively increasing refinement was used. This approach provides a final result with the desired resolution (Level 2) and a relatively low computational time; however, transferring the mesh introduces errors that require additional simulation time to reduce. These errors would not occur if only the Level 2 grid were to be used (i.e., coarser grids were not used), but this strategy increases the overall computational time and possibly slows the propagation of the flow solution through the mesh. The effect of these processes on the required number of revolutions, while considered qualitatively, cannot be easily quantified and are thus discussed only conceptually in this work.

5.4. Convergence of High Operating Scenario

As for the low operating scenario, the convergence of the flow field in the stator slots of the high operating scenario (N = 1800 rpm, Q = 2.54 L/s) was based on velocity components, velocity magnitude, and total deformation at six representative data lines. The locations of the stator slot data surfaces are shown in Figure 4.3, with a magnified image of the data lines in Figure 4.5. The rotor is at the 0° position in all profiles (see Figure 4.6).

Figure 5.12 presents a comparison of selected velocity magnitude profiles (normalized to rotor tip speed) for periods R2-P1 and R2-P7 of the high operating scenario simulation with Level 1 mesh. Each data series represents the velocity magnitude through the centreline of the stator slot at either 1 mm or 7 mm depth. Qualitatively, the profiles appear to be similar.

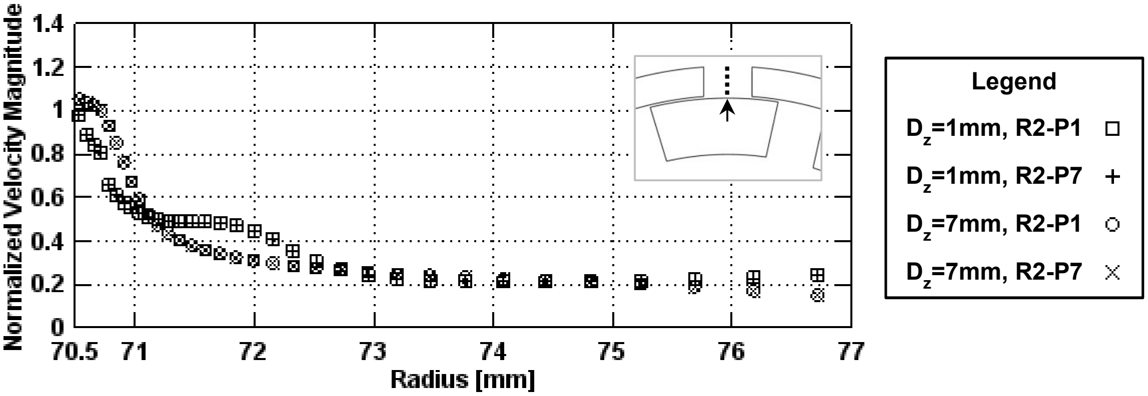

Figure 5.12: Velocity magnitude profiles in the stator slot for the high operating scenario (*N* = 1800 rpm, *Q* = 2.54 L/s) with the Level 1 mesh. The arrow and dotted line indicate the location of the profiles. Velocity profiles for both periods are qualitatively similar.

The relative changes in the Level 1, 2, and 3 meshes with the high operating scenario are shown in Figure 5.13. In all cases, the relative change in velocity magnitude from the first period to the second is less than 1%, so the flow in the stator slot is judged to have converged.

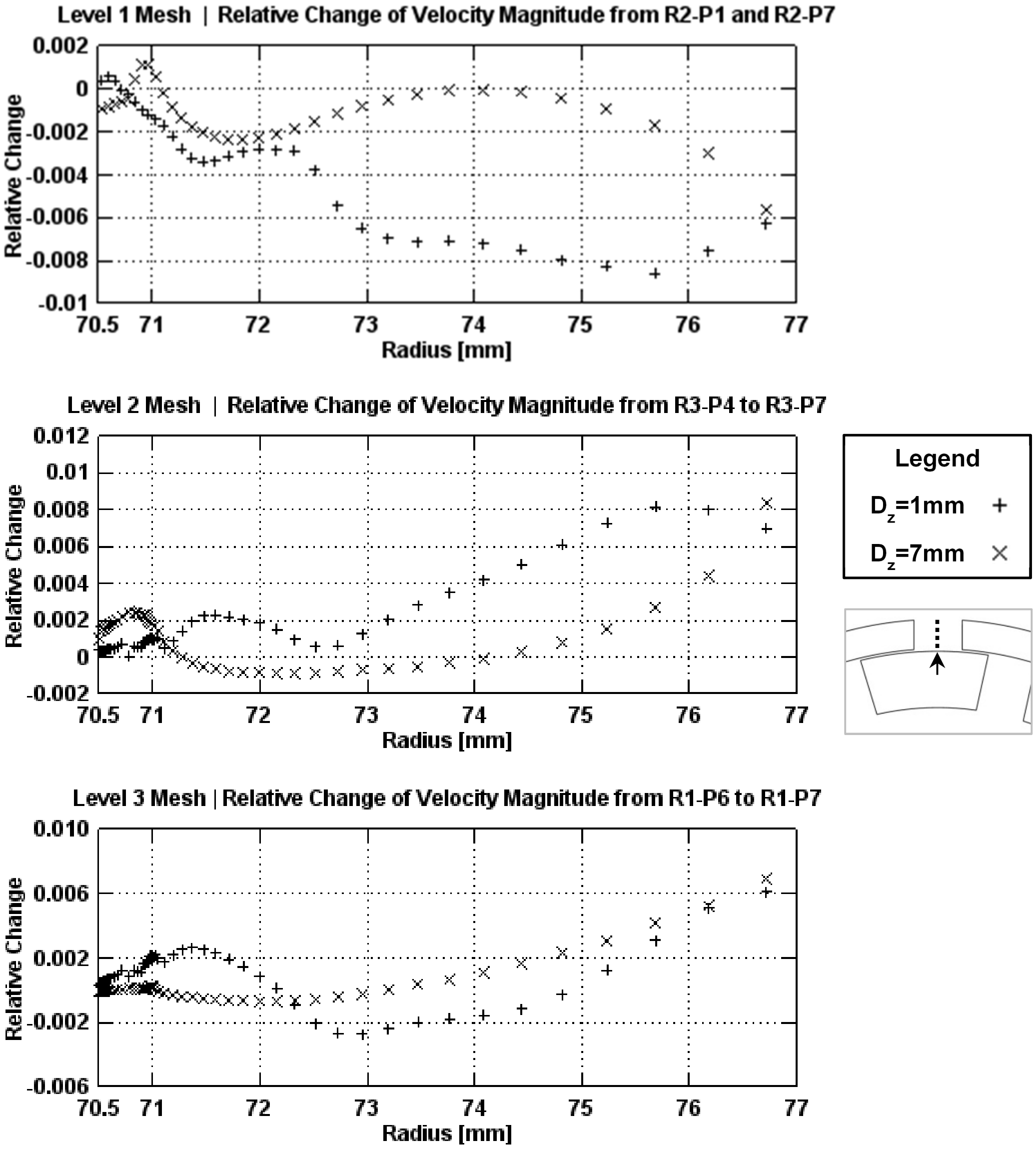

Figure 5.13: Relative change in velocity magnitude in the stator slot for the high operating scenario (*N* = 1800 rpm, *Q* = 2.54 L/s) with the Level 1, 2, and 3 meshes. The arrow and dotted line indicate the location of the profiles.

The tangential velocity profiles within the shear gap at same depths and rotor positions as in Section 5.1 are presented in Figure 5.14 for the high operating condition with Level 1 mesh. The profiles are at two depths (6 and 15 mm) and two rotor positions (0° and 15°). As with the stator slot velocity profiles shown in Figure 5.1, the tangential velocities are observed to be qualitatively similar.

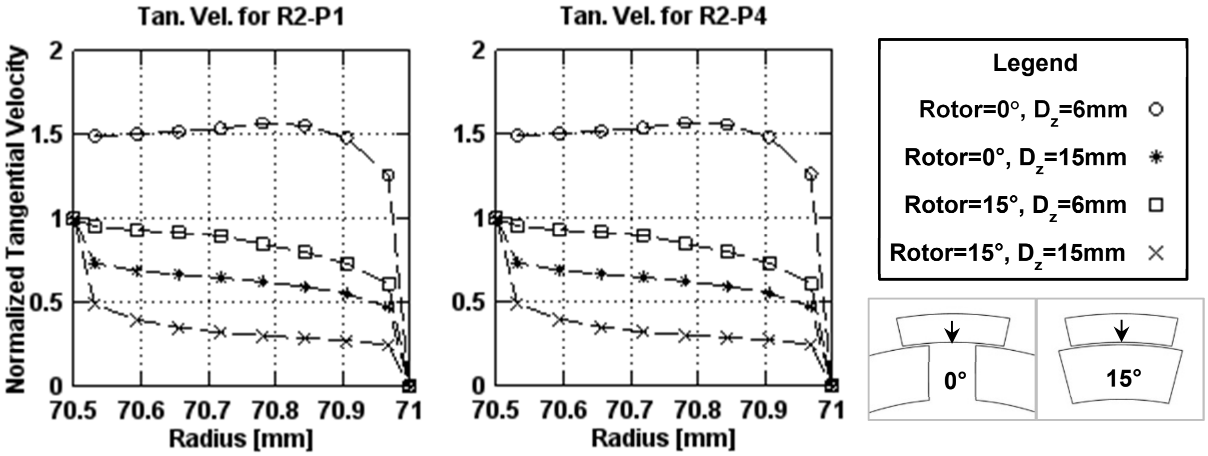

Figure 5.14: Tangential velocity profiles in the shear gap for the high operating scenario (N = 1800 rpm, Q = 2.54 L/s) with the Level 1 mesh. The arrow indicates the location of the profiles.

The relative change in each of the four velocity profiles discussed above for all three mesh levels is shown in Figure 5.15. All relative changes are less than the 1% flow field convergence threshold. The absolute values of the maximum relative changes are 0.27%, 0.14%, and 0.54% for the Level 1, 2, and 3 meshes. By comparison, the maximum relative changes (as absolute values) in the stator slot velocity profiles are 0.86%, 0.84% and 0.69% for the Level 1, 2, and 3 meshes, respectively (see Figure 5.13). It is again observed that relative changes in the wider, more open stator slot are higher than those in the highly confined shear gap.

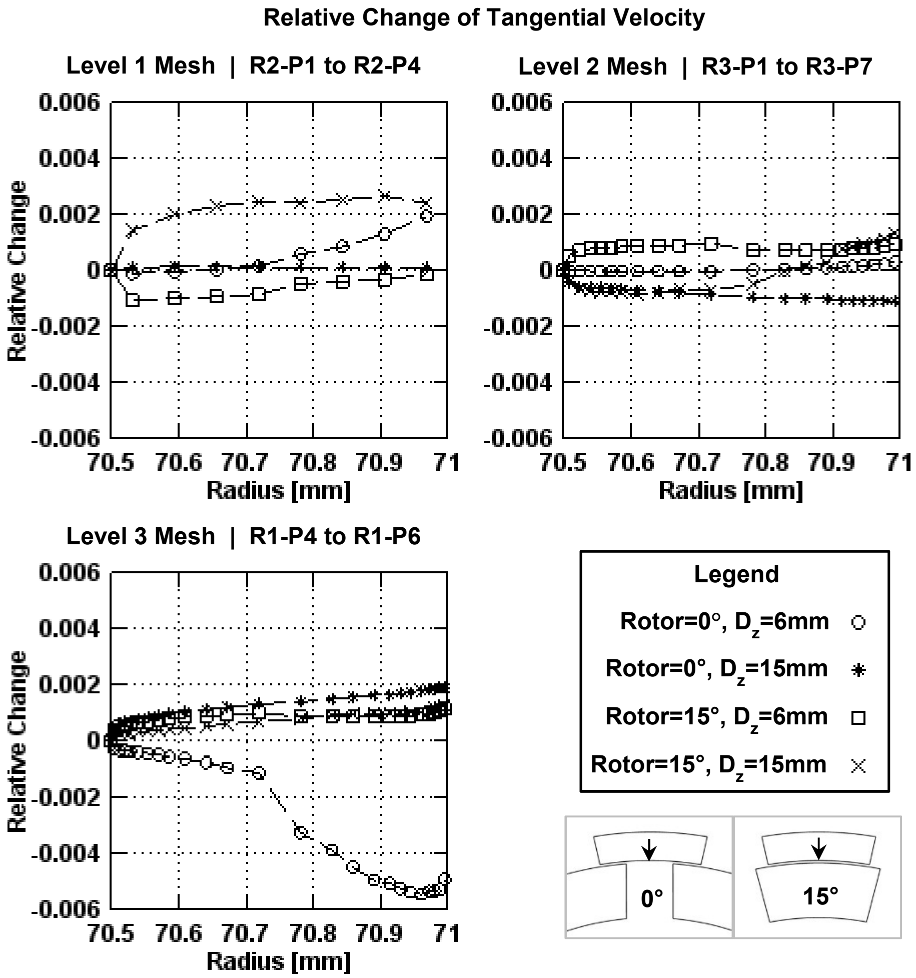

Figure 5.15: Relative change in tangential velocity in the shear gap for the high operating scenario (*N* = 1800 rpm, *Q* = 2.54 L/s) with the Level 1, 2, and 3 meshes. The arrow indicates the location of the profiles.

The total deformation rate profiles on the stator tooth for the high operating scenario with Level 1 mesh for two periods (R2-P1 and R2-P4) are shown in Figure 5.16. The convergence of total deformation rates is evaluated with respect to rotor position (or equivalently time). The dotted line indicates the mean total deformation rate based on all data surface cells, while the dashed lines represent the maximum and minimum predicted total deformation rates for any one data surface cell.

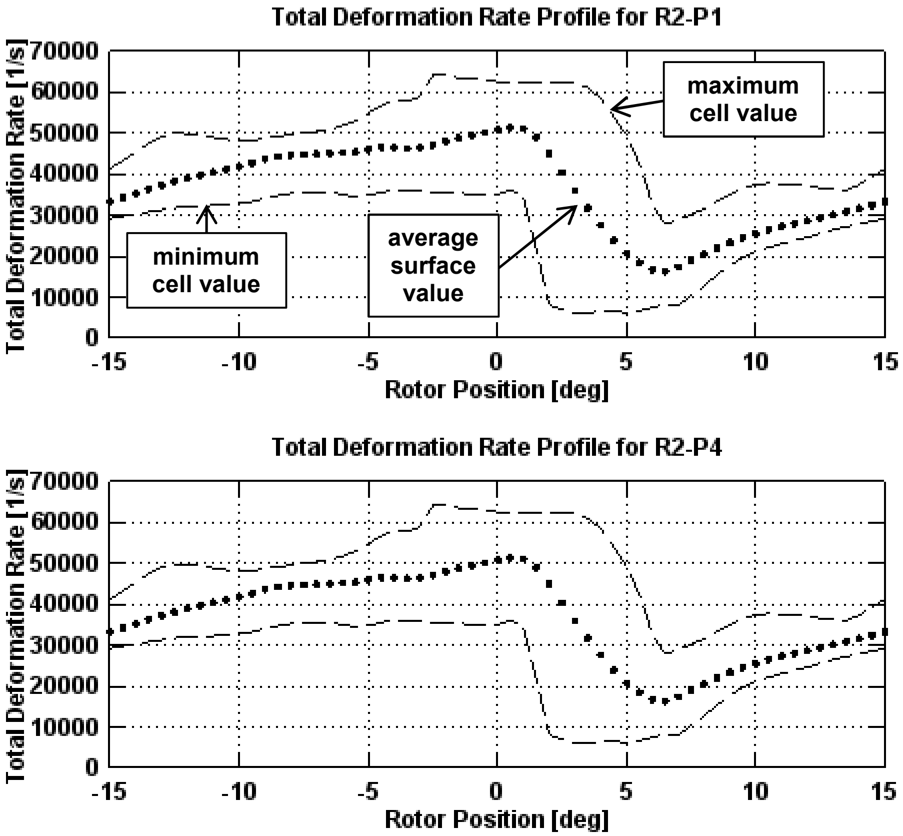
Total Deformation Rate Profile for R2-P1

Total Deformation Rate Profile for R2-P4

Figure 5.16: Total deformation rate profiles on the stator tooth for the high operating scenario (N = 1800 rpm, Q = 2.54 L/s, $\dot{\gamma}$ = 26,630 s^{-1}) with the Level 1 mesh.

The plots of relative change for the Level 2 and 3 simulations are presented in Figure 5.17. The title of each plot identifies the scenario, mesh level, and revolution numbers. The relative changes in total deformation rate are less than 1% for all simulations.

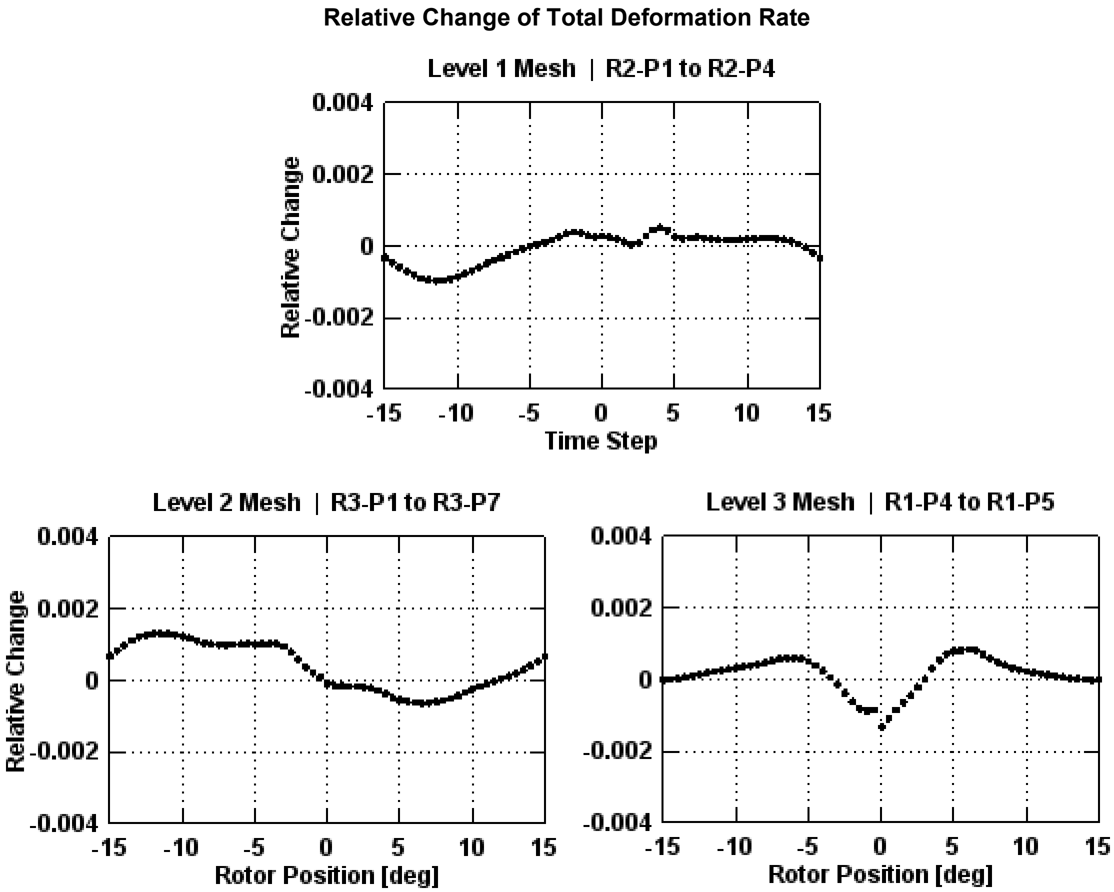

Figure 5.17: Relative change in total deformation on the stator tooth for the high operating scenario ($N = 1800$ rpm, $Q = 2.54$ L/s, $\dot{\gamma} = 26{,}630\ \mathrm{s}^{-1}$) with the Level 1, 2, and 3 meshes.

In summary, simulations of all three mesh levels for the high operating scenario meet the flow field convergence criterion and are therefore judged to be converged. As with the low operating scenario, the relative changes of the velocity and total deformation rate profiles in the tightly confined shear gap are generally lower than the relative changes calculated in the wider stator slot.

5.5. Grid Independence for High Operating Scenario

The arrangement of the figures in this section is the same as for the grid independence study of the low operating scenario; refer to Section 5.2 for more detailed explanations of the plots.

Qualitatively, grid independence in the stator slot for the high operating scenario was established by looking at plots of velocity vectors at two depths. Figure 5.18 compares velocity vector plots at a depth of 1 mm for three different mesh levels and the previously-conducted simulation by Kevala (unpublished personal communication). Figure 5.19 presents the corresponding velocity fields at a depth of 7 mm. The fluid behaviour does not appear to be strongly dependent on the mesh refinement. The predicted velocities at the upstream side of the shear gap do seem to decrease with increasing mesh resolution; this behaviour can also be seen in shear gap velocity profiles later in this next section. Lower velocities are also predicted for fluid impinging on the downstream stator tooth.

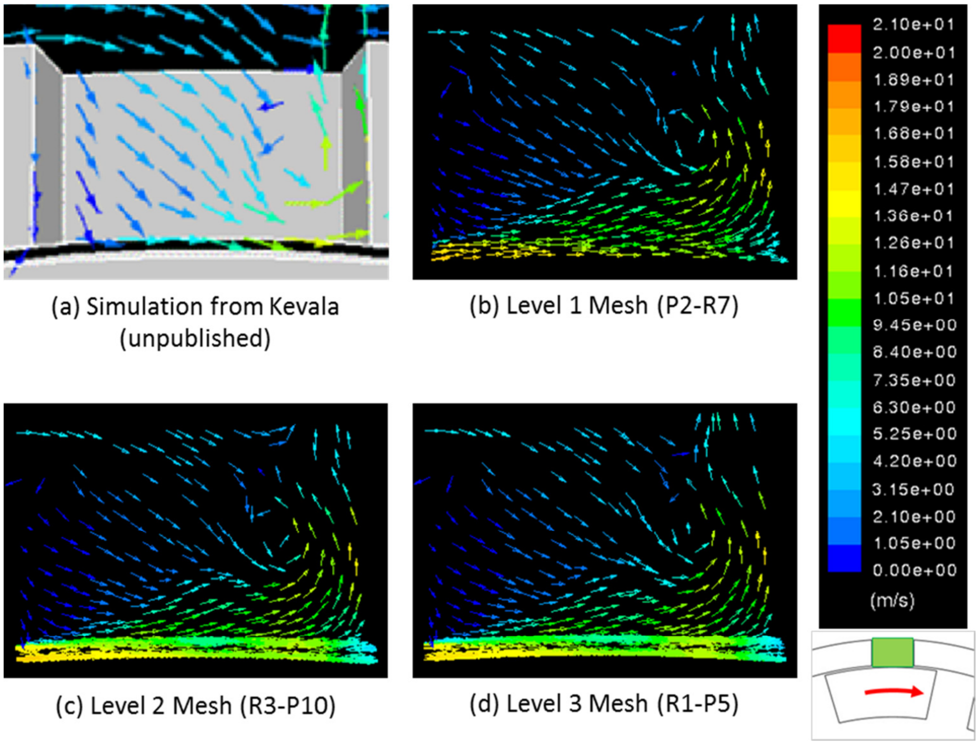

(a) Simulation from Kevala (unpublished)

(b) Level 1 Mesh (P2-R7)

(c) Level 2 Mesh (R3-P10)

(d) Level 3 Mesh (R1-P5)

Figure 5.18: Comparison of velocity vectors in stator slot for Kevala's preliminary CFD model and the Level 1, Level 2, and Level 3 meshes at depth of 1 mm for high operating scenario (N = 1800 rpm, Q = 2.54 L/s).

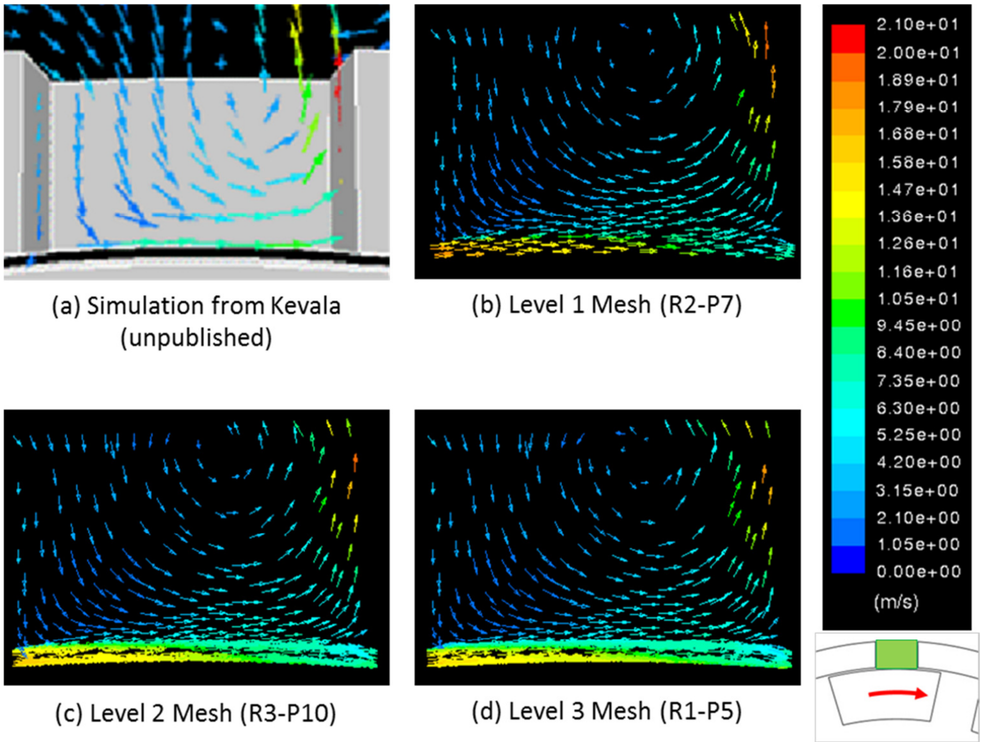

(a) Simulation from Kevala (unpublished)

(b) Level 1 Mesh (R2-P7)

(c) Level 2 Mesh (R3-P10)

(d) Level 3 Mesh (R1-P5)

Figure 5.19: Comparison of velocity vectors in stator slot for Kevala's preliminary CFD model and the Level 1, Level 2, and Level 3 meshes at depth of 7 mm for high operating scenario (N = 1800 rpm, Q = 2.54 L/s).

Figure 5.20 provides a comparison between the stator slot centreline velocity magnitude profiles at each mesh level for the high operating scenarios. These plots show that the velocity close to the rotor tooth (*r* = 70.5 mm) is noticeably lower for the Level 2 and Level 3 solutions, which agrees with the observations from the vector plots.

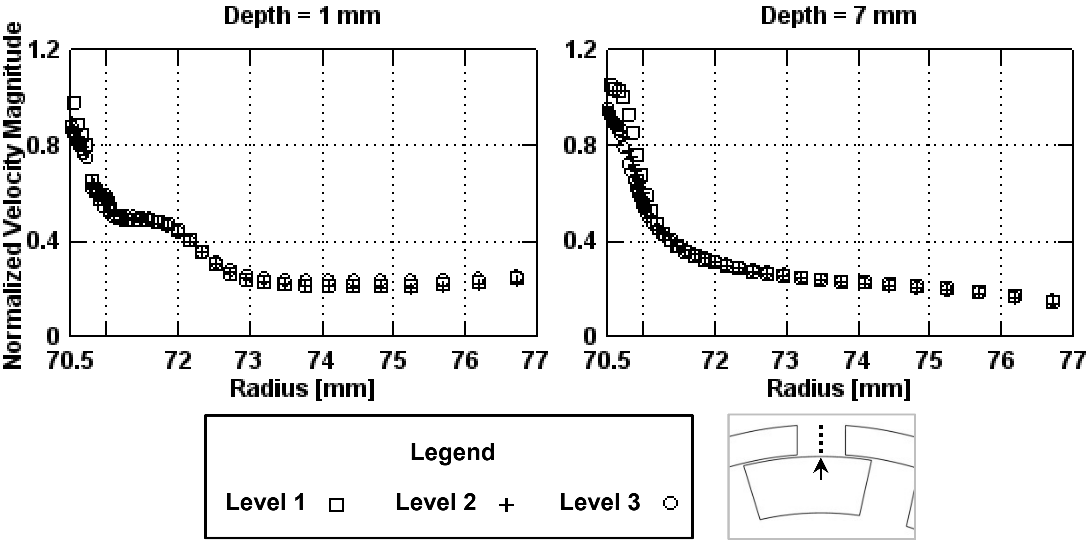

Figure 5.20: Comparison of velocity magnitude in stator slot at depths of 1 mm and 7 mm between Level 1, Level 2, and Level 3 meshes for the high operating scenario (*N* = 1800 rpm, *Q* = 2.54 L/s). The arrow and dotted line indicate the location of the profiles.

Figure 5.21 presents the tangential velocity (normalized with the rotor tip speed) profiles at a depth of 6 mm for the high operating scenario. Comparison plots for other depths are provided in Appendix A. For the Level 1 and 2, the tangential velocity profiles at 6 mm depth are comparable.in their trend and magnitude when the shear gap is not confined by a rotor tooth (-1.5°, 0°, and 2°). However, the behaviour is different in the positions where the shear gap is confined by the rotor tooth (10°, 15°, and 20°). In these positions, we see that the Level 1 solution rises quickly with the sweep of the rotor, reaching a profile that signifies the dominance of pressure difference as a driving force.

The Level 2 solution shows a similar solution, but the fluid velocity does not exceed the rotor tip speed. The Level 2 and 3 tangential velocity profiles are similar in their trend and general behaviour, but the Level 3 profiles are generally lower than their Level 2 counterparts.

The total deformation rates on the stator tooth for high operating scenario with Level 1, 2, and 3 meshes are compared in Figure 5.22. Both plots show that there is a substantial difference in the predicted total deformation rates of all three mesh levels. Compared to the Level 1 solution, the Level 2 total deformation rate profile has an average relative change of nearly 1000%. Compared with the Level 2 mesh, the Level 3 mesh has an average relative change of 34%. Thus, the Level 3 mesh is necessary for grid independence of total deformation rate on the stator teeth.

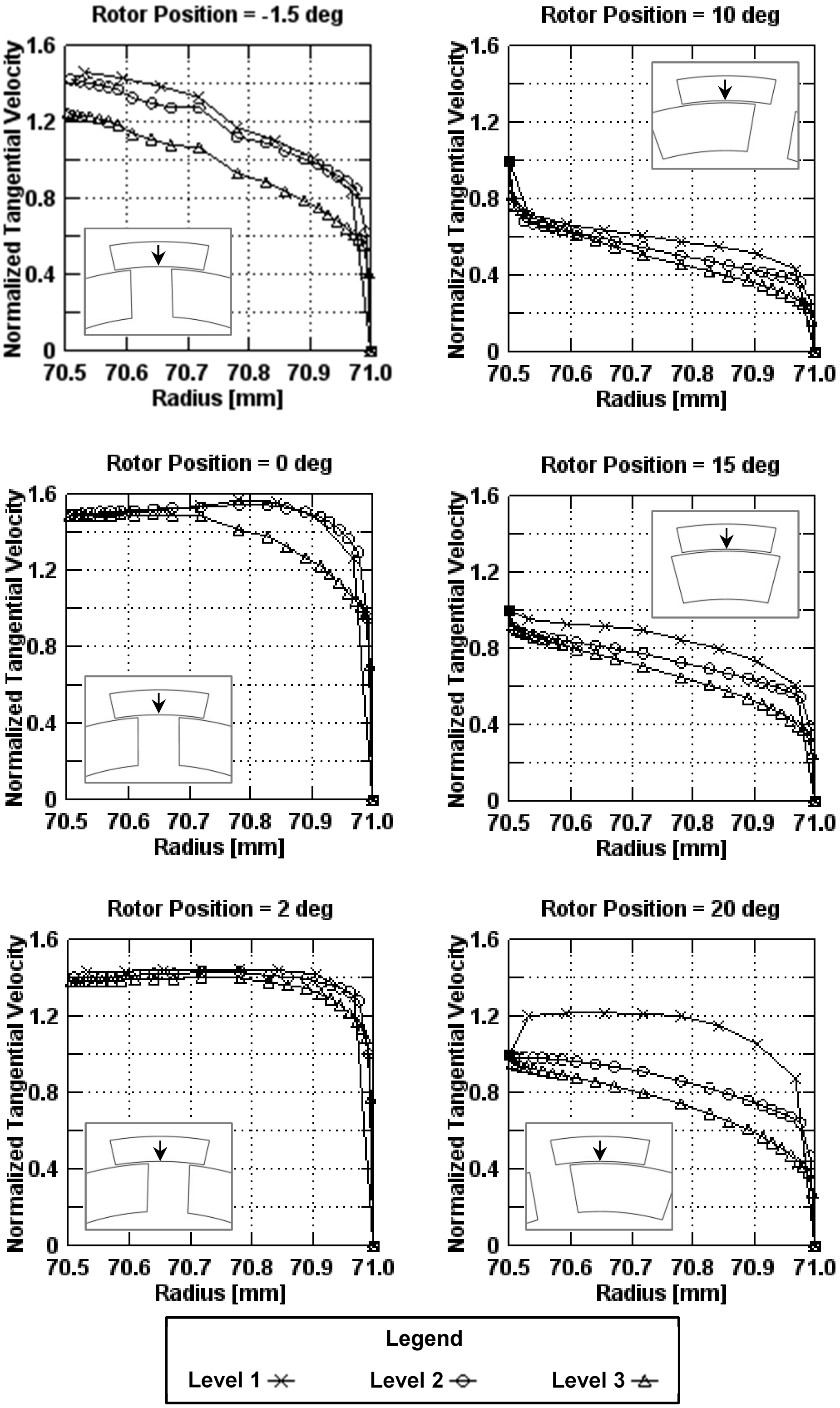

Figure 5.21: Comparison of tangential velocity in the shear gap between Level 1, Level 2, and Level 3 meshes for the high operating scenario ($N = 1800$ rpm, $Q = 2.54$ L/s). All profiles are at a depth of 6 mm. The arrow indicates the location of the profile.

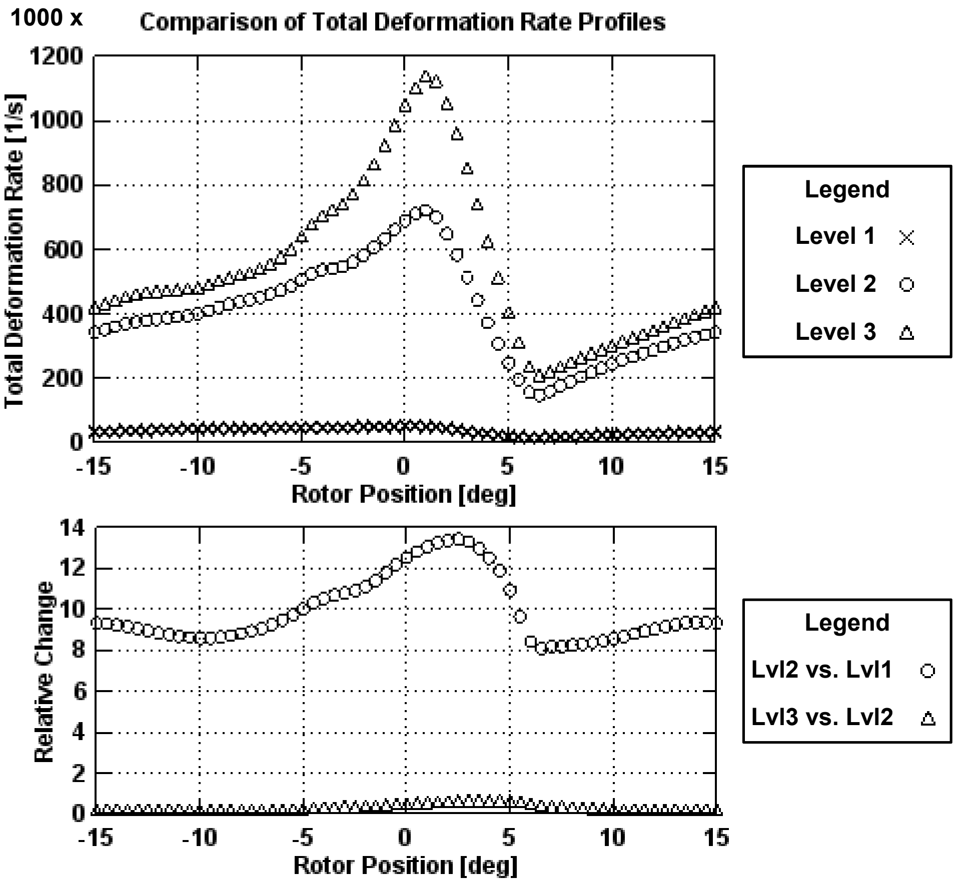

Figure 5.22: Comparison of total deformation rate on the stator tooth between Level 1, Level 2, and Level 3 meshes for the high operating scenario (N = 1800 rpm, Q = 2.54 L/s, $\dot{\gamma}$ = 26,630 s^{-1}).

5.6. Summary of Grid Independence for High Operating Scenario

Analysis of the representative profiles of velocity magnitude in the stator slot, tangential velocity in the shear gap, and total deformation rate on the stator tooth indicate that the flow field has converged in all simulations. As with the low operating scenario, the flow field convergence for both shear gap velocity and stator tooth total deformation rates was relatively fast because this region is confined and strongly directed by the rotor. The convergence of velocity in the stator slot was slower due to its larger size and connection to the volute.

The flow field in the Level 2 mesh was found to be different than the flow field in the Level 1 mesh. The velocities in the stator slot were found to be similar, except in the shear gap where the predicted velocity was lower in the Level 2 mesh. Total deformation rates in the Level 2 solution were greater than the corresponding Level 1 deformation rates by a factor of 10, on average. Level 2 shear gap velocities were similar to Level 1 velocities when the shear gap was open to the rotor slot, but tended to be lower when confined by the rotor tooth.

The Level 3 total deformation rate and tangential velocity profiles were of the same general shape as the corresponding Level 2 profiles. However, the magnitudes of the total deformation rates were higher by an average of about 34%, while tangential velocities at 6 mm depth were somewhat lower.

The limits of the currently available computational resources do not permit practical investigation into further refinement of the mesh. As a consequence, the Level 3 solution was selected to represent the standard operating scenario. As further computational power becomes available, the grid independence of this solution should be verified.

Similar to the low operating scenario, the simulation results of the high operating scenario with the Level 3 mesh (presented in previous sections and Chapter 7) are also based on a total of 24 revolutions (starting from a converged MRF flow field). The required number of revolutions depends on the region of interest and the computational strategy (discussed qualitatively in Section 5.3 and not repeated here). From the results of the convergence study (see Section 5.4), reaching convergence for only the shear gap may take about 16 revolutions. Also reaching convergence in the stator slots will require about 24 revolutions. The high operating scenario reaches convergence more slowly than the low operating scenario because of the greater intensity of turbulence in the flow.

6. Low Operating Scenario: Simulation Results

This chapter presents results from the low operating scenario. The rotational speed of the rotor is 300 rpm (rotor tip speed of 2.21 m/s), and the inlet flow rate is 0.315 L/s. See Table 4.1 for other operational parameters and metrics. All results presented in this chapter come from the Level 2 grid (20 cells across the shear gap, 10 million cells overall), following from the conclusions drawn in Chapter 5. The following sections will present detailed information on the total deformation rate, velocity, and energy dissipation rate within the shear gap and stator slots.

6.1. Velocities within the Stator Slots

Figure 6.1 presents vector plots in the stator slot when the slot is blocked by the rotor tooth. Vectors are coloured by velocity magnitude according to the scale shown on the right. Vector plots for two rotor positions (0° and 5°) and two depths (1 mm and 7mm) are shown; the stator slot data surfaces are illustrated in Figure 4.5. The qualitative flow behaviour is dependent primarily on depth, not position of the rotor. For both positions, there appears to be a circular recirculation zone near the middle of the slot at 7 mm depth (near the midplane of the stator slot). This pattern appears to be along the same depth plane. At 1 mm depth, there is a similar recirculation region appears near the middle of the slot, with an additional region at the upstream stator tooth (on the left side of the vector plot). This recirculation region is not in the plane of constant depth; instead, the recirculation is on the plane perpendicular to the radial direction because of the boundary effects imposed by the volute cover (at 0 mm depth).

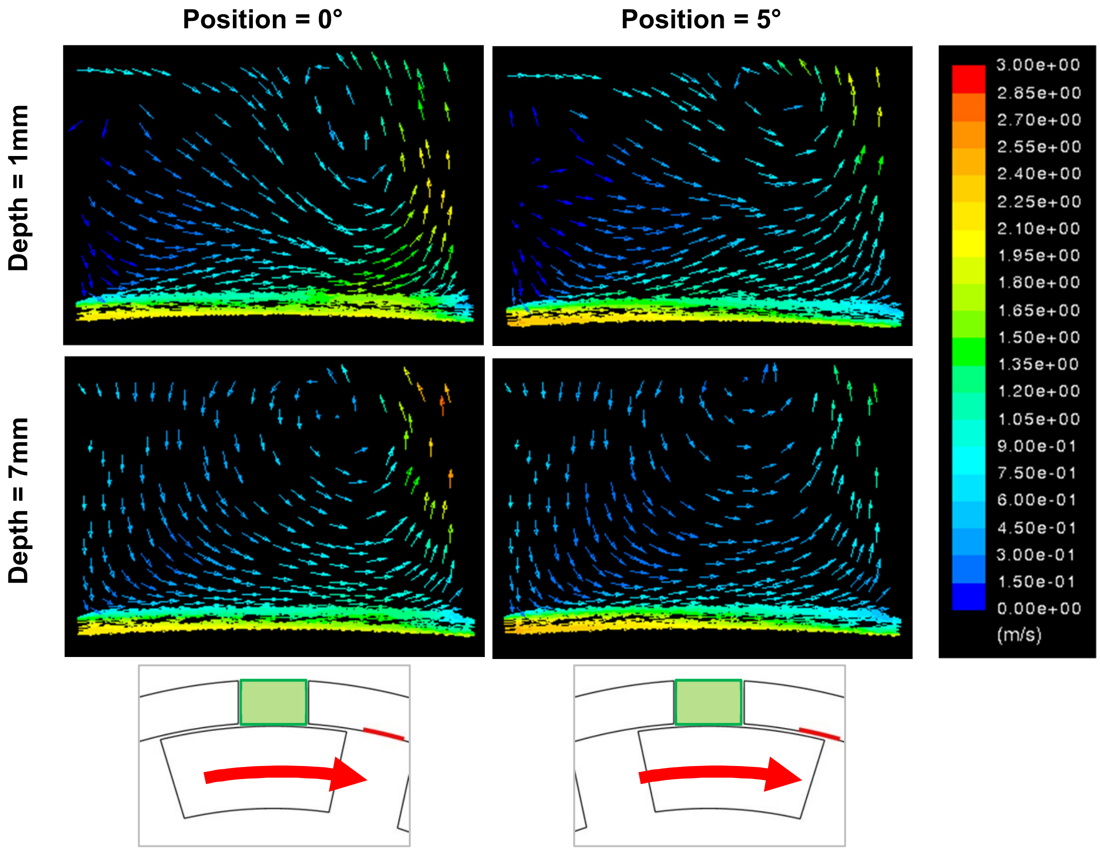

Figure 6.1: Velocity magnitude in the stator slot when the slot is blocked by a rotor tooth for the low operating scenario (*N* = 300 rpm, *Q* = 0.315 L/s, Level 2 mesh).

Figure 6.2 shows the vector plots for 1 mm and 7 mm depth when the rotor tooth is not completely blocking the stator slot. When the trailing edge of the rotor tooth passes the stator slot (such as in the plots at 15°), a small vortex is generated off the downstream edge of the upstream stator tooth at 7 mm depth. At 1 mm depth, the vortex also exists, but its pattern is disrupted by the recirculation region attached to the upstream stator tooth. When the leading edge of the next rotor tooth is passing the rotor slot (20°), there is an acceleration of flow and increased impingement on the downstream stator tooth. The circulation regions seen in the 15° position generally still exist, despite the change in the local boundary conditions due to the presence of the rotor tooth.

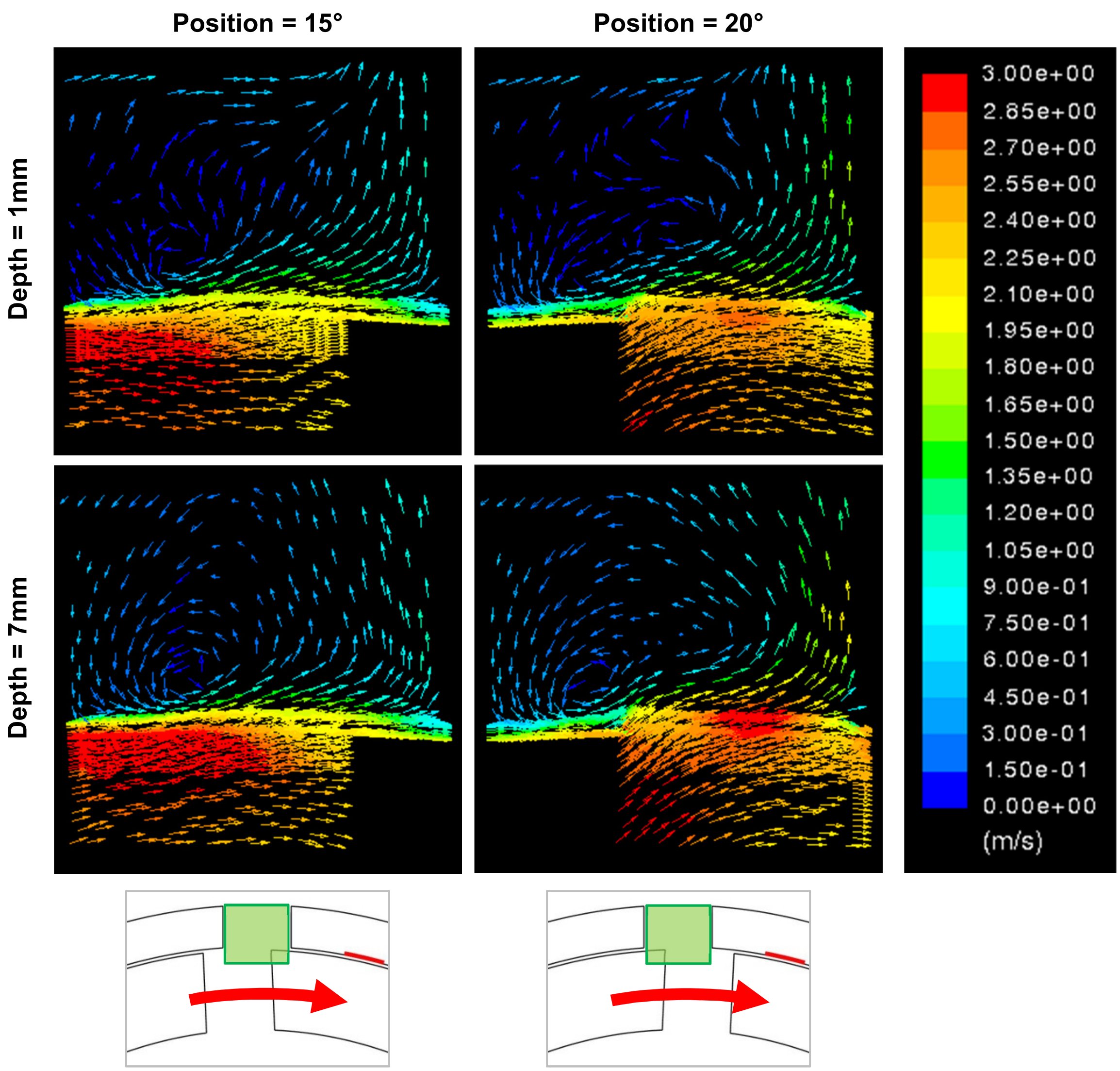

Figure 6.2: Velocity magnitude in the stator slot when the slot is not blocked by the rotor tooth for the low operating scenario ($N = 300$ rpm, $Q = 0.315$ L/s, Level 2 mesh).

6.2. Shear Gap Velocity Profiles

As discussed in Section 4.4, a large number of velocity profiles were evaluated. In this work, selected representative velocity profiles will be discussed; the complete set of velocity profiles are provided in Appendix B. The first twelve profiles are at a depth of 15 mm from the volute cover, deep enough that these profiles are always confined (or bounded) by rotor and stator surfaces. The second twelve profiles are at a depth of 6mm. These profiles illustrate how the periodic disturbance of the rotor slot affects the velocity. All reported velocities are normalized to the rotor tip speed (V_{tip} = 2.21 m/s). Axial velocities are positive in the direction of positive z-coordinate (or equivalently negative D_z-coordinate, see Figure 1.2 for mixer plan and coordinates).

Figure 6.3 shows the normalized tangential and axial velocities across the shear gap at a depth of 15 mm from the volute cover. Radial velocities are less than 1% of the rotor tip speed and are not reported. While the velocity profiles at 15 mm are always confined, the profiles in Figure 6.3 are separated into two groups. In the left subplots, labelled ‘Unconfined Above’, the shear gap data surface is exposed to the rotor slot at depths between 0 mm and 10.25 mm (see Figure 1.2). The right subplots, labelled ‘Confined Above’, show velocity profiles for which the entire shear gap data surface is confined on both rotor and stator sides.

The simulation results show that the general magnitude of the tangential velocities is similar with a slight oscillation as a function of position. When the rotor tooth is not confining the shear gap data surface, a steady decrease in the tangential velocity is observed. When fully-confined by the rotor tooth, the tangential velocity increases as the rotor tooth sweeps past the data surface. Axial velocity is not significant when the data surface is fully-confined by the rotor tooth, but there is a substantial negative axial velocity (i.e., away from the volute cover) when the data surface is partly open to the rotor slot.

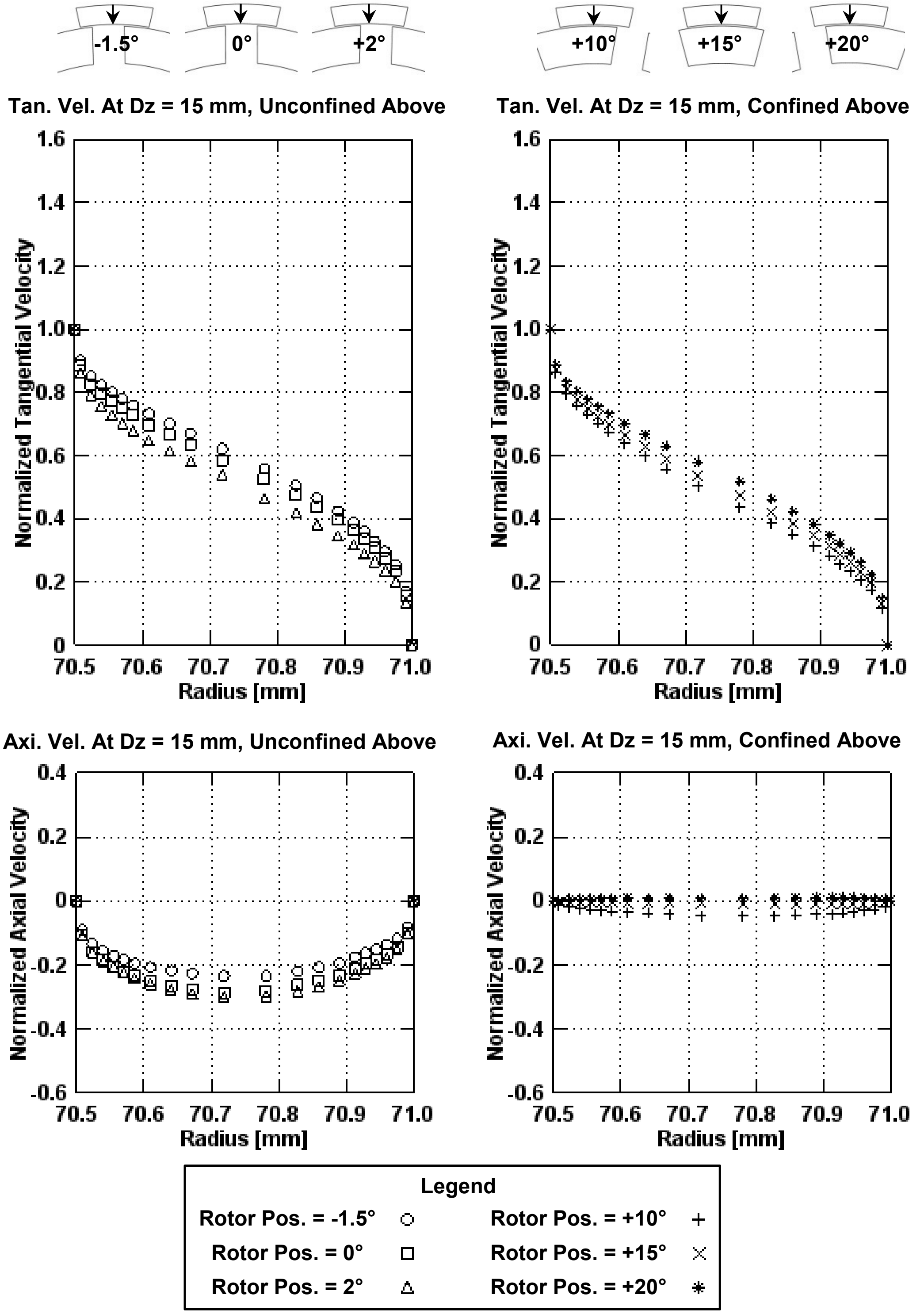

Figure 6.3: Tangential and axial velocity profiles across shear gap at a depth of 15 mm for the low operating scenario (N = 300 rpm, Q = 0.315 L/s, Level 2 mesh).

The tangential and axial velocity profiles at 6 mm depth are shown in Figure 6.4. When the data line is confined by the rotor tooth, as seen in the right plots labelled 'Confined Positions', the tangential and axial velocity profiles appear to be similar to the equivalent profiles at 15 mm depth. The normalized tangential velocity at the centre of the gap is somewhat greater than 0.5, an indication that pressure is a moderate driving force on the flow. As the trailing edge of the rotor tooth passes over the shear gap data surface, the left plots labelled 'Unconfined Positions' show that there is a steady increase in tangential velocity, with the profile flattening out at $1.3V_{tip}$. At all positions, axial velocity is not significant.

Figure 6.5 shows the radial velocity profiles at 6 mm for rotor positions in which the shear gap data surface is not confined by the rotor tooth. As the trailing edge of the rotor tooth sweeps passes the data line (-1.5 to 0°), the negative radial velocity increases (i.e., increased velocity toward center of mixer). However, as the leading edge of the next rotor tooth approaches, the radial velocity decreases toward zero. By 2°, the radial velocity is positive (i.e., in the outward direction). Note that radial velocities for rotor positions in which the shear gap is confined (10°, 20°, and 30°) are less than 1% of the rotor tip velocity and are not shown.

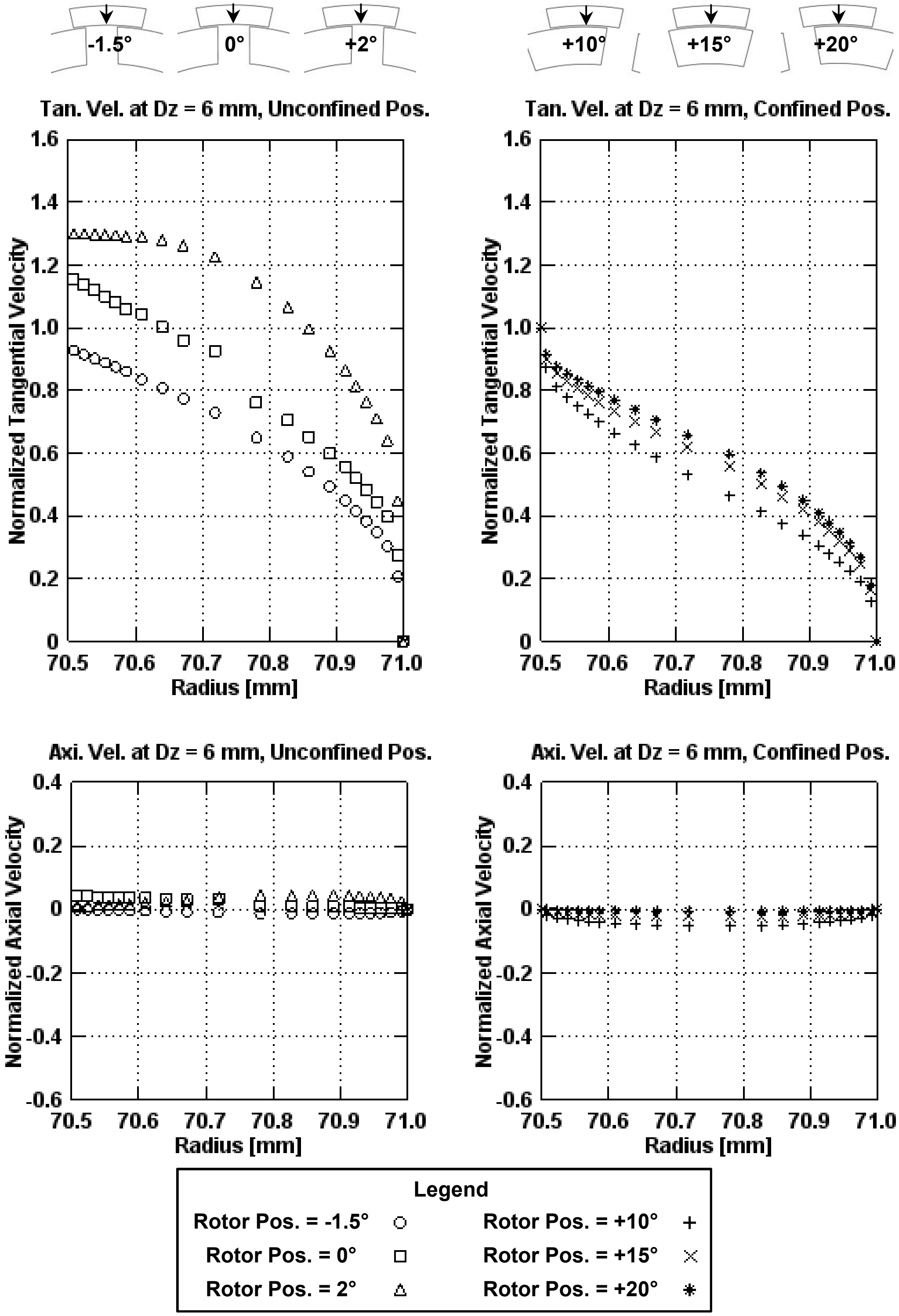

Figure 6.4: Tangential and axial velocity profiles across shear gap at a depth of 6 mm for the low operating scenario (N = 300 rpm, Q = 0.315 L/s, Level 2 mesh).

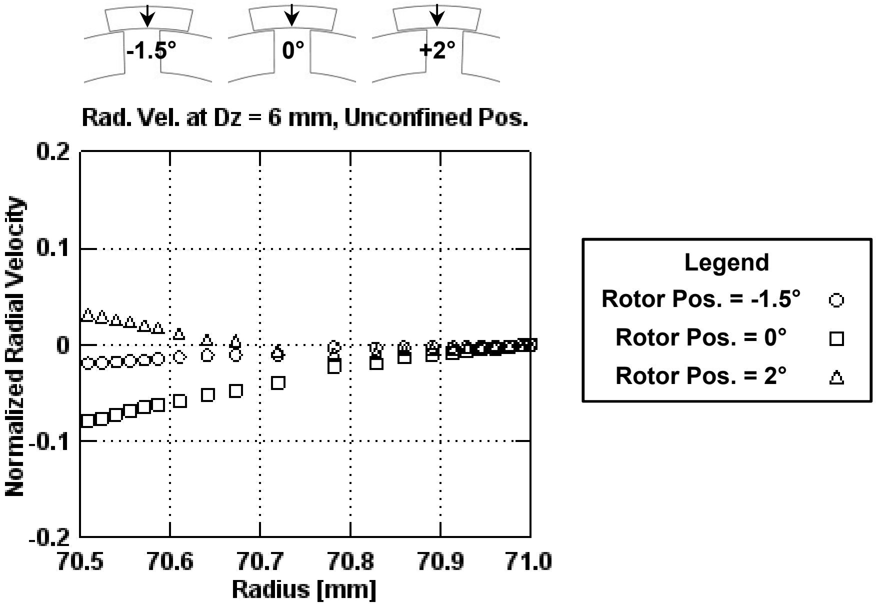

Figure 6.5: Radial velocity profiles across shear gap at a depth of 6 mm for the low operating scenario (N = 300 rpm, Q = 0.315 L/s, Level 2 mesh).

The behaviour of the fluid on either side of the shear gap (i.e., at the corners of the stator tooth) is shown in Figure 6.6 for three selected rotor positions (0°, 10°, and 20°), with the left and right plots showing the areas counter-clockwise and clockwise, respectively, of the shear gap data surface. Vectors are coloured by the value of velocity magnitude, and the depth is 6 mm (same depth as the velocity profiles in Figure 6.4 and Figure 6.5). The fluid in the rotor slots appears to be moving at the same speed or faster than the rotor tip speed (V_{tip} = 2.21 m/s). In both the 10° and 20° vector plots, the velocity magnitude does not change significantly across the confined region. In the 0° plots, the velocity magnitude in the downstream area (right plot) is different than that in the upstream area (left plot). This appears to be because the shear gap is the only outlet for the otherwise confined relatively high velocity fluid in the rotor slot.

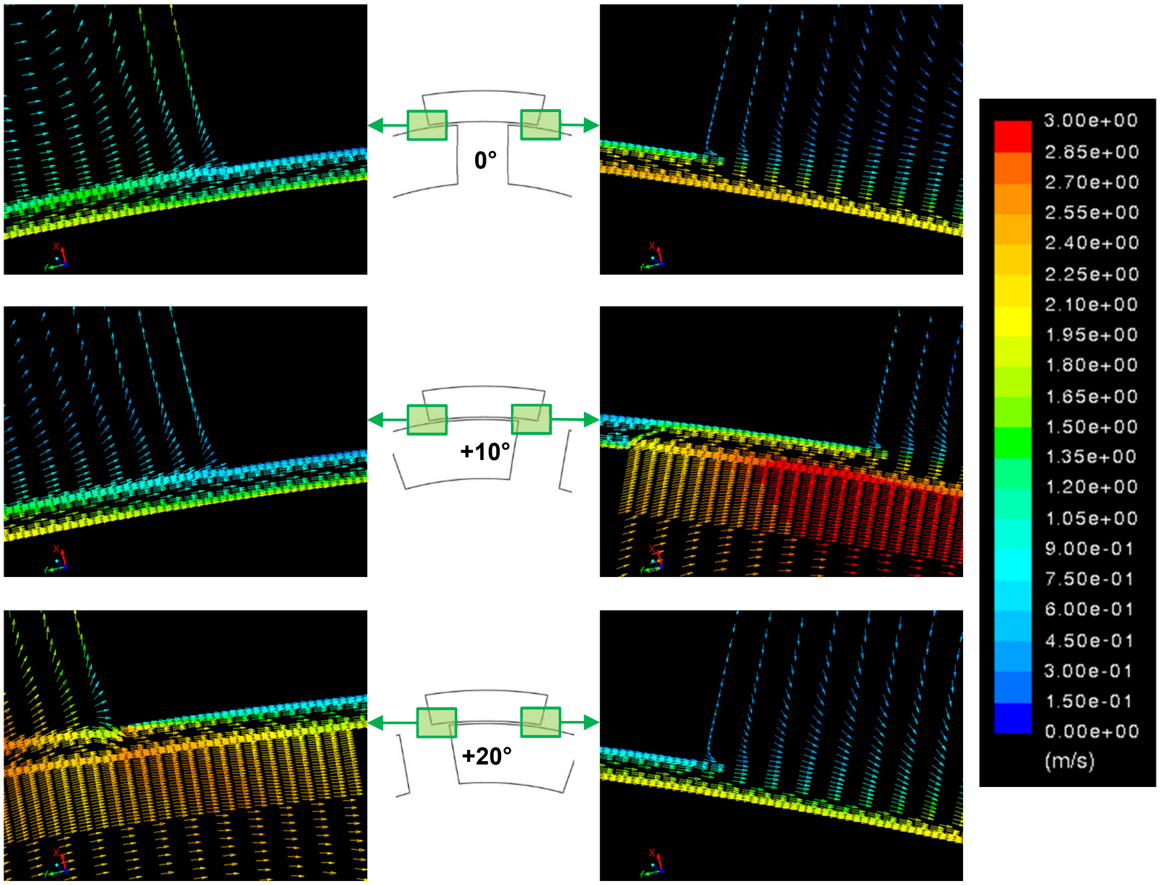

Figure 6.6: Velocity vector plots at corners of the stator slot at selected rotor positions for the low operating scenario (N = 300 rpm, Q = 0.315 L/s, Level 2 mesh). Plots are at a depth of 6 mm, and vectors are coloured by velocity magnitude.

6.3. Total Deformation Rates on Stator Teeth

The total deformation rate on the stator teeth was extracted from the solution for each of 2304 cells comprising the stator tooth data surface (illustrated in Figure 4.5). This data is plotted against rotor position in Figure 6.7. The dotted line is the mean total deformation rate over all cells at each rotor position, with dashed lines above and below indicating the maximum and minimum individual cell values. Within the vertical dash-dot lines, the stator tooth data surface is either partly or wholly exposed to the rotor slot (i.e., not confined by the rotor tooth). To the left and right of the dash-dot lines, the stator tooth is wholly confined by the rotor tooth.

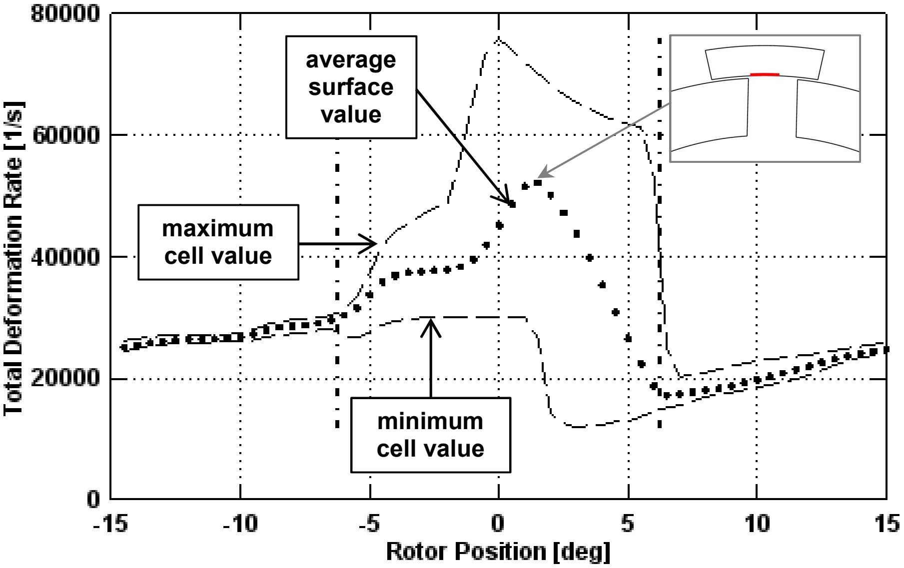

Figure 6.7: Total deformation rates from stator tooth data surface for the low operating scenario (N = 300 rpm, Q = 0.315 L/s, $\dot{\gamma}$ = 4,430 s^{-1}, Level 2 mesh). The inset illustration shows the rotor position at the peak mean total deformation rate.

Figure 6.7 shows that when the stator tooth data surface is confined by the rotor tooth (i.e., the rotor tooth 'covers' the data surface, from +6.5° to +15°/-15° to -6.5°), the mean total deformation rate across the stator tooth data surface is nearly uniform. However, it is not constant with position/time, as would have been assumed for plane Couette flow. Instead, it is predicted to increase steadily from the minimum mean of the period (17,200 s^{-1}), which occurs just as the rotor tooth passes over the data surface. Note that the nominal shear rate of 4,430 s^{-1} was exceeded at all points on the data surface.

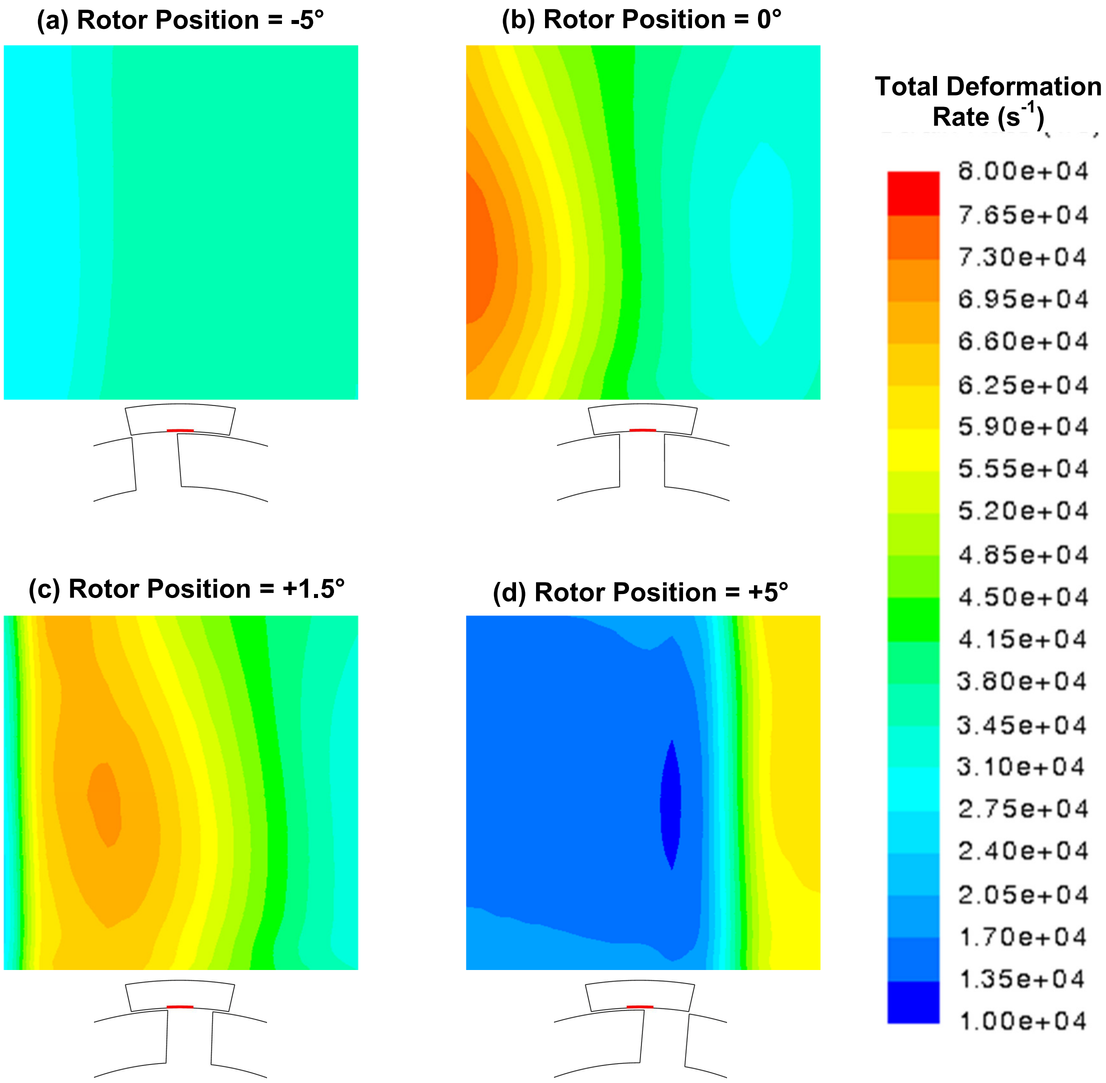

Figure 6.8: Contour plots of total deformation rates when the stator tooth data surface is not completely confined by the rotor tooth for the low operating scenario ($N = 300$ rpm, $Q = 0.315$ L/s, $\dot{\gamma} = 4{,}430$ s^{-1}, Level 2 mesh).

The total deformation rate profile is more complex when the rotor slot/opening passes over the data surface. The contour plots presented in Figure 6.8 illustrate the greater degree of spatial variation. When the rotor tooth passes plot (a) shows that there is a suction region in which the total deformation rate on the data surface decreases. As the face of the next rotor tooth approaches, plots (b) and (c) show a sharp increase in the total deformation rate, rising to a peak value of 52,200 s^{-1}. As the rotor tooth travels over the data surface, it re-confines and suppresses much of the fluid flow, demonstrated sharp drop in plot (d).

6.4. Effect of Turbulence Model on Shear Gap Velocity Profile

Flow throughout most of the IKA prototype mixer is expected to be turbulent, necessitating the use of some form of turbulence model. However, the low Reynolds number within the shear gap is characteristic of laminar flow. In an ideal plane Couette flow, the velocity profile would be strictly linear with between the moving and stationary surfaces. The shear gap velocity results presented in Section 6.2 show a distinct S-type curve. This may be caused by physical phenomena, such as pressure gradient or periodic exposure to turbulence, or it may be a numerical error caused by the application of turbulence models to laminar regions.

To quantify the impact of the turbulence model on the results in the shear gap, FLUENT was used to simulate a simple steady-state channel flow. The channel, shown in Figure 6.9, was 10 cm long, 6 cm wide, and 0.5 mm deep. Cell geometries equivalent to those in shear gaps of the Level 1 and Level 2 IKA prototype mixer simulations were tested. The bottom wall (shown in grey) had a velocity of 2.21 m/s (equivalent to 300 rpm in the IKA prototype mixer). The top wall, not shown in Figure 6.9, was stationary. The side walls (shown in yellow) were treated as symmetry boundary conditions ($\partial u/\partial z = 0$). Both inlet (not shown) and outlet (shown outlined in blue) were specified at the same pressure; the only driving force for fluid motion was from the motion of the bottom plate.

Velocity predictions were taken in the centre of the channel, 9 cm from the inlet (shown as a red line).

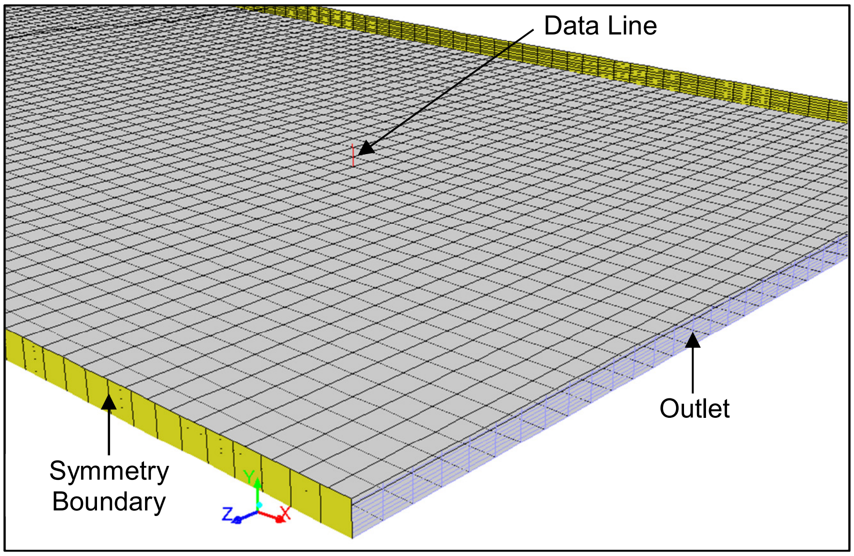

Figure 6.9: Image of mesh for the channel model, with top plate removed. The grey surface is the moving wall at the bottom of the channel. The yellow surface is the side wall, set to symmetry boundary conditions to simulate an infinitely wide channel. The outlet mesh is outlined in blue. Velocities were measured at the red data line.

The results of the benchmark tests are shown in Figure 6.10. Note that in all plots, the coordinate is shifted to the range of the shear gap (70.5 mm to 71 mm) and the velocities are normalized to the velocity of the moving wall. Plot (a) shows the velocity profiles with the laminar and realizable k-ε models. The laminar profiles for Level 1 (8 cell) and Level 2 (20 cell) shear gaps were identical and therefore independent of grid resolution; only the Level 1 profile is shown. For the turbulent k-ε simulations, velocity profiles are notably different than the laminar profile. This confirms that using the realizable k-ε model in regions of laminar flow introduces numerical errors into the simulation. Improved grid resolution appears to bring the turbulent velocity profile toward to the laminar velocity profile, but it is unlikely to reach the laminar velocity profile, given that further grid refinement in the grid independence study did not result in significantly different results.

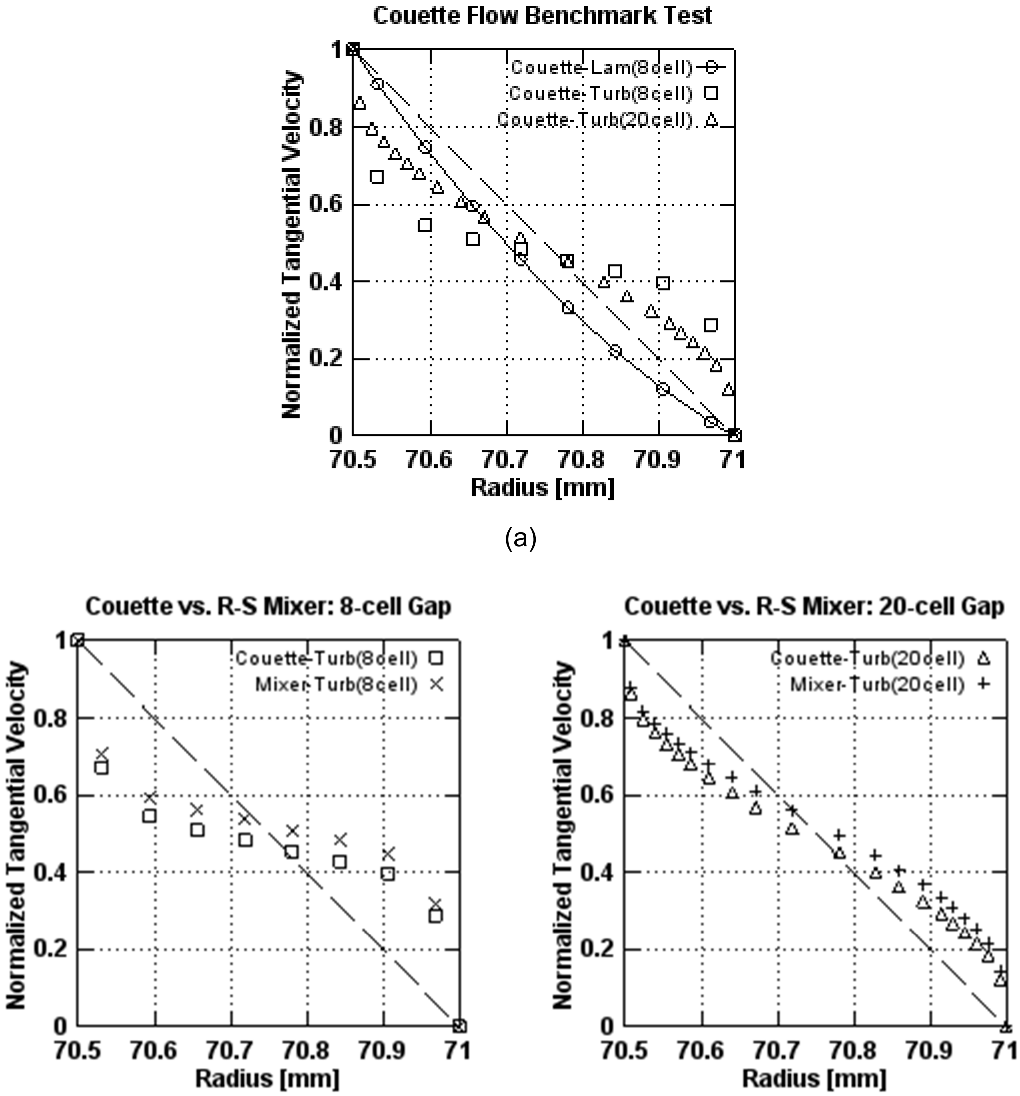

(a)

(b)

(c)

Figure 6.10: Results of Couette channel flow benchmark simulation. Plot (a) shows the results predicted by FLUENT with the laminar and realizable k-ε model. Plots (b) and (c) compare the channel flow results to average IKA mixer simulation results at 15 mm depth over the six rotor positions examined in Section 6.2.

Plots (b) and (c) show comparisons of the benchmark Couette profiles to the shear gap velocity profiles from the IKA prototype mixer. The velocity profile used to represent the IKA prototype mixer was an average of the six 15-mm depth tangential velocity profiles shown in Figure 6.3. The 15 mm tangential velocity profiles are the closest physical match Couette flow; they were averaged to remove the effect of the oscillation that was observed. Plots (b) and (c) in Figure 6.10 show that for both the Level 1 (8-cell) and Level 2 (20-cell) shear gaps, the velocity profiles for the channel flow and IKA simulations are similar.

6.5. Total Energy Dissipation and Power Draw

Table 6.1 shows the predicted average energy dissipation rates (Equation 2.3-3) for the low operating scenario (N = 300 rpm, Q = 0.315 L/s, $\dot{\gamma}$ = 4,430 s^{-1}, Level 2 mesh) for each fluid zone (see Figure 4.1). The energy dissipation due to mean velocity gradients is based on the volume integral of the square of total deformation rate, while the energy dissipation due to turbulence was based on the volume integral of the turbulence dissipation rate ε. These quantities are evaluated every 1° (two time steps). Both of these pathways are significant pathways for energy dissipation.

Table 6.1: Average Energy Dissipation Rates for Low Operating Scenario (N = 300 rpm, Q = 0.315 L/s, $\dot{\gamma}$ = 4,430 s^{-1}, Level 2 mesh).

Fluid Zone	**Volume [cm^3]**	**Volumetric Energy Dissipation Rate**		**Total Energy Dissipation Rate**	
		Mean [W/m^3]	**Turbulent [W/m^3]**	**Mean [W]**	**Turbulent [W]**
Rotor Zone	469	376	1470	0.176	0.689
Stator Zone	554	285	1350	0.158	0.748
Outlet Zone	69.5	12.6	1110	0.00087	0.0768
Total	1090	307	1390	0.335	1.51

The power consumption and power number for the rotor are also calculated at each time step. Based on the torque output from FLUENT, the power consumption and power number are calculated using Equations 2.3-1 and 2.3-2, respectively, again at 1° increments (two time steps). The average, minimum, and maximum values of torque, power consumption, and power number are shown in Table 6.2.

Table 6.2: Torque, Power, and Power Number Predictions for Low Operating Scenario ($N = 300$ rpm, $Q = 0.315$ L/s, $\dot{\gamma} = 4{,}430\ \mathrm{s}^{-1}$, Level 2 mesh).

Variable	**Description**	**Units**	**Average Value**	**Minimum Value**	**Maximum Value**
T	Torque	N-m	0.0714	0.0685	0.0782
P	Power Consumption	W	2.24	2.15	2.46
N_{Po}	Power Number	-	10.3	9.90	11.3

6.6. Summary of Results

The velocity field in the stator slots was examined at two depths and four rotor positions. When the rotor tooth is blocking the stator slot, there appear to be two main circulating flows in the stator slot. At both depths (1 mm and 7 mm) and positions (0° and 5°), there is a pattern that circulates flow mostly in the radial-tangential plane. In addition, there is a flow pattern that circulates flow in the tangential-axial plane attached to the upstream stator tooth. When the rotor tooth is not fully blocking the stator slot (positions 15° and 20°), a vortex is predicted at the downstream edge of the upstream stator tooth. This is caused by the strong impingement of flow on the downstream stator tooth.

The velocity components across the shear gap were presented for six rotor positions at depths of 6 mm and 15 mm. At 15 mm depth, where the inner side of the shear gap is always confined by the rotor, the tangential velocity profiles oscillate, with velocities decreasing when the rotor tooth is not confining the shear gap data surface and increasing when the data surface is confined by a rotor tooth. At 6 mm depth, the tangential velocity increases in a similar fashion when the data surface is completely confined by a rotor tooth, but continues to increase as the rotor slot passes over the data surface, dropping again only when the shear gap becomes re-confined. Axial velocity is significant at 15 mm depth when the shear gap data surface is not wholly confined, but otherwise appears to be negligible. Radial velocity is significant at 6 mm depth when the rotor slot is open to the shear gap data surface, but otherwise is negligible.

Vector plots of the flow patterns at each end of the shear gap were presented. Across a continuous region of the shear gap, the velocity magnitude does not change significantly. When the rotor slot is blocked by the stator tooth, there is an increase in fluid velocity in the shear gap section downstream of the rotor slot.

The profile of total deformation rate was quantified with respect to mean, maximum, and minimum values over the stator tooth data surface. The predicted total deformation rates always exceed the nominal shear rate of 4,430 s^{-1} by a factor of at least 3.8. In rotor positions where the shear gap is confined by the rotor tooth, the total deformation rate on the stator tooth data surface increases steadily with time. During this time, the total deformation rates across the data surface are relatively uniform. However, once the trailing edge of the rotor tooth passes over the data surface, there is a period of lower deformation rates followed by a pulse of high deformation ahead of the leading edge of the next rotor tooth.

The results of the IKA prototype simulations were compared with benchmark Couette channel flow simulations with both laminar and turbulent viscous models. Comparing channel flow simulations conducted with both the laminar and realizable k-ε model shows that applying the realizable k-ε model to a laminar flow case does not result in a laminar velocity profile. The velocity profiles in the simulation of the IKA prototype mixer (conducted with the realizable k-ε model) are similar to the Couette flow simulations with the turbulent model. This indicates the IKA prototype simulations may be poorly-modelled in the shear gap regions because turbulent kinetic energy is being generated in potentially laminar regions. Because FLUENT is incapable of applying different turbulence models to different regions, resolving this issue will require user-defined functions to limit turbulence generation in cells tightly confined by the rotor and stator surfaces.

The energy dissipation in the IKA prototype was evaluated using the total deformation rates and turbulence dissipation rates. A total of 1.84 W is dissipated in the three fluid zones in the simulation (0.335 W due to mean velocity gradients and 1.51 W from turbulence dissipation). The average power consumption from the rotor is 2.24 W, and the average power number is 10.3.

7. High Operating Scenario: Simulation Results

This chapter presents results from the high operating scenario. The rotational speed of the rotor is 1800 rpm (rotor tip speed of 13.3 m/s), and the inlet flow rate is 2.54 L/s. Other operational parameters and metrics are found in Table 4.1. All results come from the Level 3 mesh, based on the conclusions of the grid independence study (see Chapter 5). The following sections will present detailed information on the total deformation rate, velocity, and energy dissipation rate within the shear gap and stator slots.

The layout of this chapter and its figures are similar to Chapter 6. For brevity, general explanations of the figures are omitted. Refer to the previous chapter for additional details.

7.1. Velocities within the Stator Slots

Figure 7.1 presents vector plots in the stator slot when the slot is blocked by the rotor tooth. Vector plots for two rotor positions (0° and 5°) and two depths (1 mm and 7mm) are shown (see Section 4.4 for more details). The qualitative flow behaviour is dependent more on depth than on the specific position of the rotor. The surface at 7 mm (near the midplane of the stator slot) experiences a circular recirculation zone. The surface at 1 mm shows two distinct regions of flow: 1) a region of moderate velocity that impinges on the tooth and escapes into the volute, and 2) a low velocity region which appears to enter the stator slot from the volute and gets entrained into the flow of region 1.

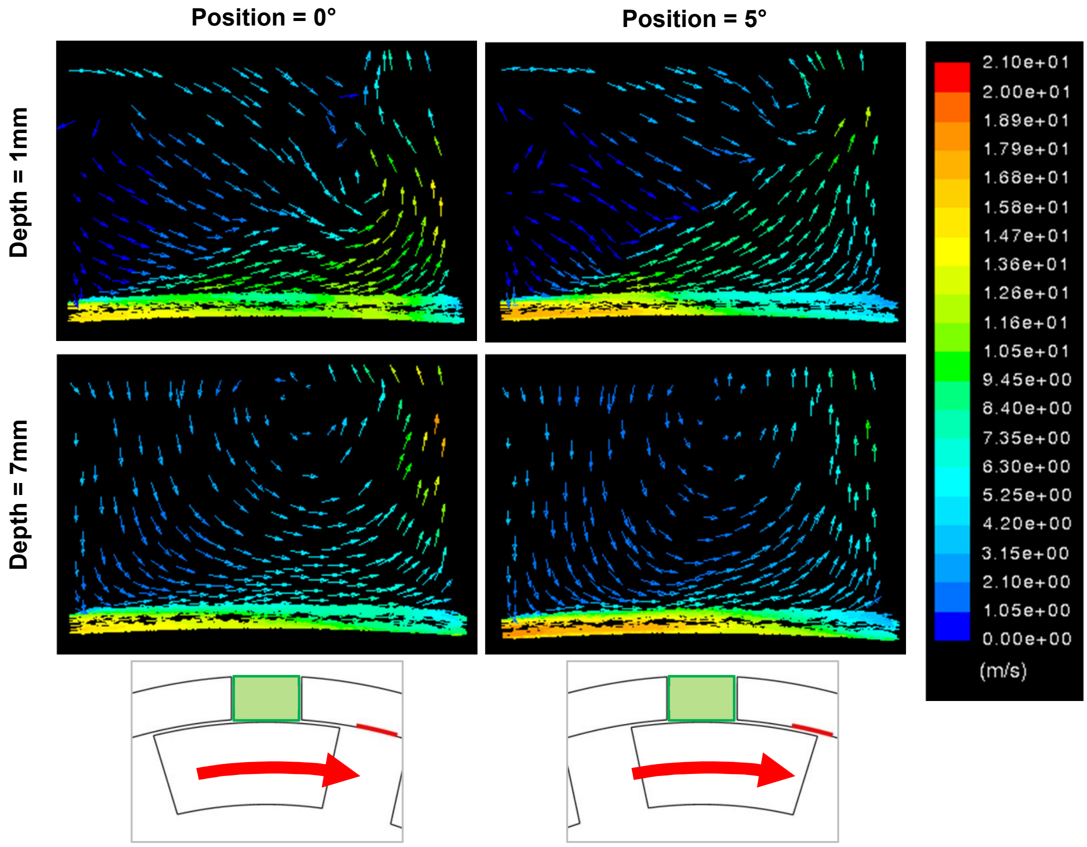

Figure 7.1: Velocity magnitude in the stator slot when the slot is blocked by a rotor tooth for the high operating scenario (N = 1800 rpm, Q = 2.54 L/s, Level 3 mesh).

Figure 7.2 shows the vector plots for 1 mm and 7 mm depth when the rotor tooth is not completely blocking the stator slot. Similar to the low operating scenario, a vortex is generated off the downstream edge of the upstream stator tooth at 7 mm depth. The vortex also exists at 1 mm depth, but its pattern is disrupted by the greater degree of axial flow attached to the upstream stator tooth. The general structure of the flow appears to be similar in both rotor positions, but there is acceleration in the flow and increased impingement on the downstream stator tooth at 20°.

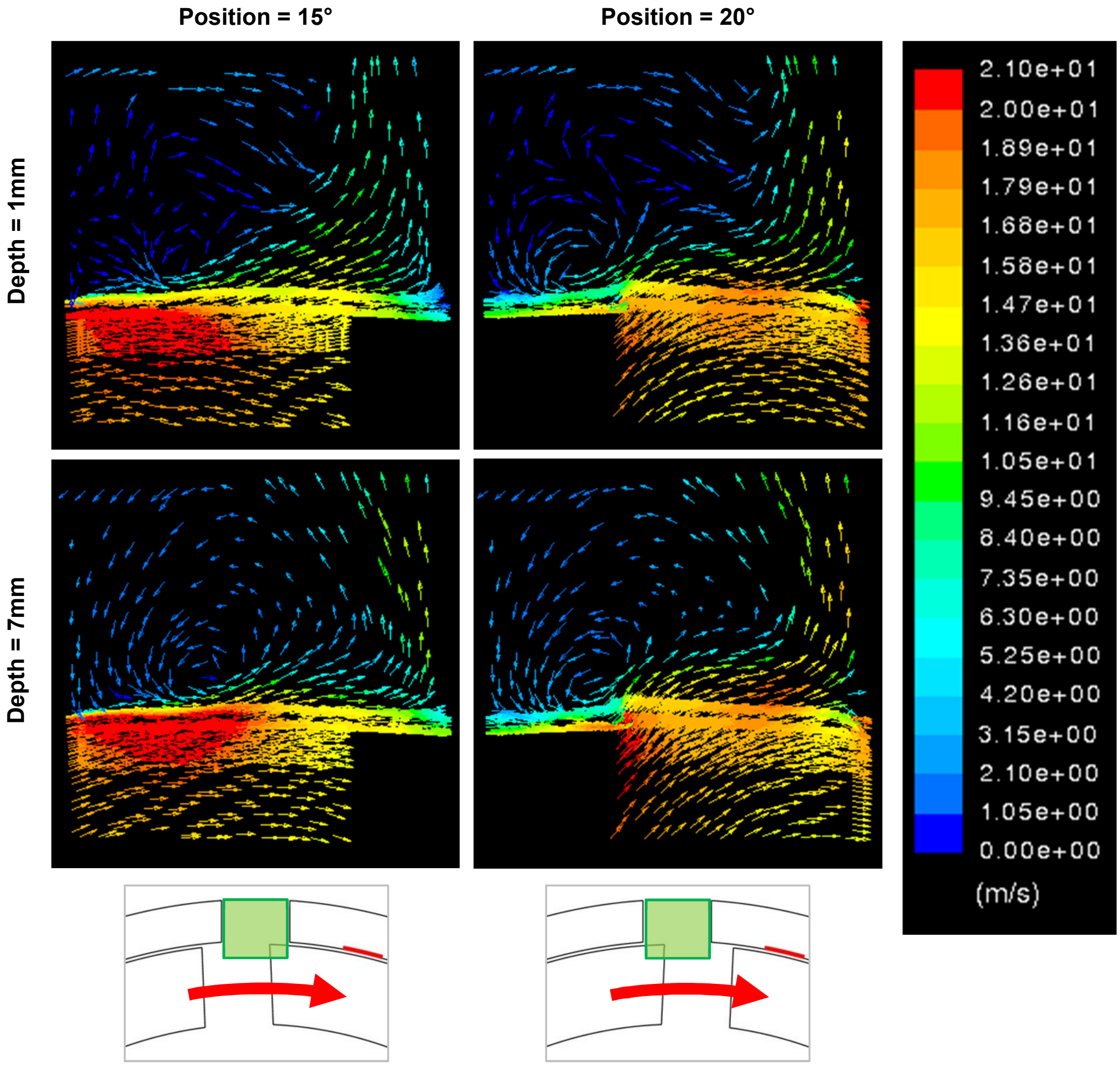

Figure 7.2: Velocity magnitude in the stator slot when the slot is not blocked by a rotor tooth for the high operating scenario ($N = 1800$ rpm, $Q = 2.54$ L/s, Level 3 mesh).

7.2. Shear Gap Velocity Profiles

A large number of velocity profiles were evaluated (see Section 4.4). Selected representative velocity profiles are discussed in this section. The complete set of velocity profiles are provided in Appendix B.

Figure 7.3 shows the normalized tangential and axial velocities across the shear gap at a depth of 15 mm from the volute cover. Radial velocities are less than 1% of the rotor tip speed and are not reported. The simulation results show that while the general magnitude of the tangential velocities is similar, there is a slight oscillation as a function of position. When the shear gap data surface is not confined by the rotor tooth (-1.5° to 2°), the tangential velocity generally decreases with time. There is a slight rise in tangential velocity when the rotor tooth re-confines the shear gap data surface (10°) and a more significant rise as the trailing edge of the rotor tooth approaches the shear gap (20°). In general, the axial component of the velocity is significant, particularly closer to the stator wall and when the shear gap data surface is not confined by the rotor tooth. The axial velocity is mostly negative (i.e., in the direction of the negative z-coordinate or positive D_z-coordinate), but there is a significant positive axial velocity during the most significant rise in tangential velocity at 20°.

The tangential and axial velocity profiles at 6 mm depth are shown in Figure 7.4. When the shear gap data surface has been confined by the rotor tooth (10°), the tangential and axial velocity profiles are similar in shape to the equivalent profiles at 15 mm depth. However, as the rotor tooth sweeps past the shear gap data surface, the tangential velocity increases and the axial velocity is suppressed. The shape of the profile at 20° suggests that in addition to the drag of the rotor, pressure may be acting as a driving force. When shear gap data surface starts to become unconfined by the rotor tooth (-1.5°), there is a sharp increase in the tangential velocity while axial velocity becomes slightly positive. As the next rotor tooth approaches (2°), the tangential velocity profile flattens out at $1.3V_{tip}$. At this rotor position, there is also a significant negative axial velocity.

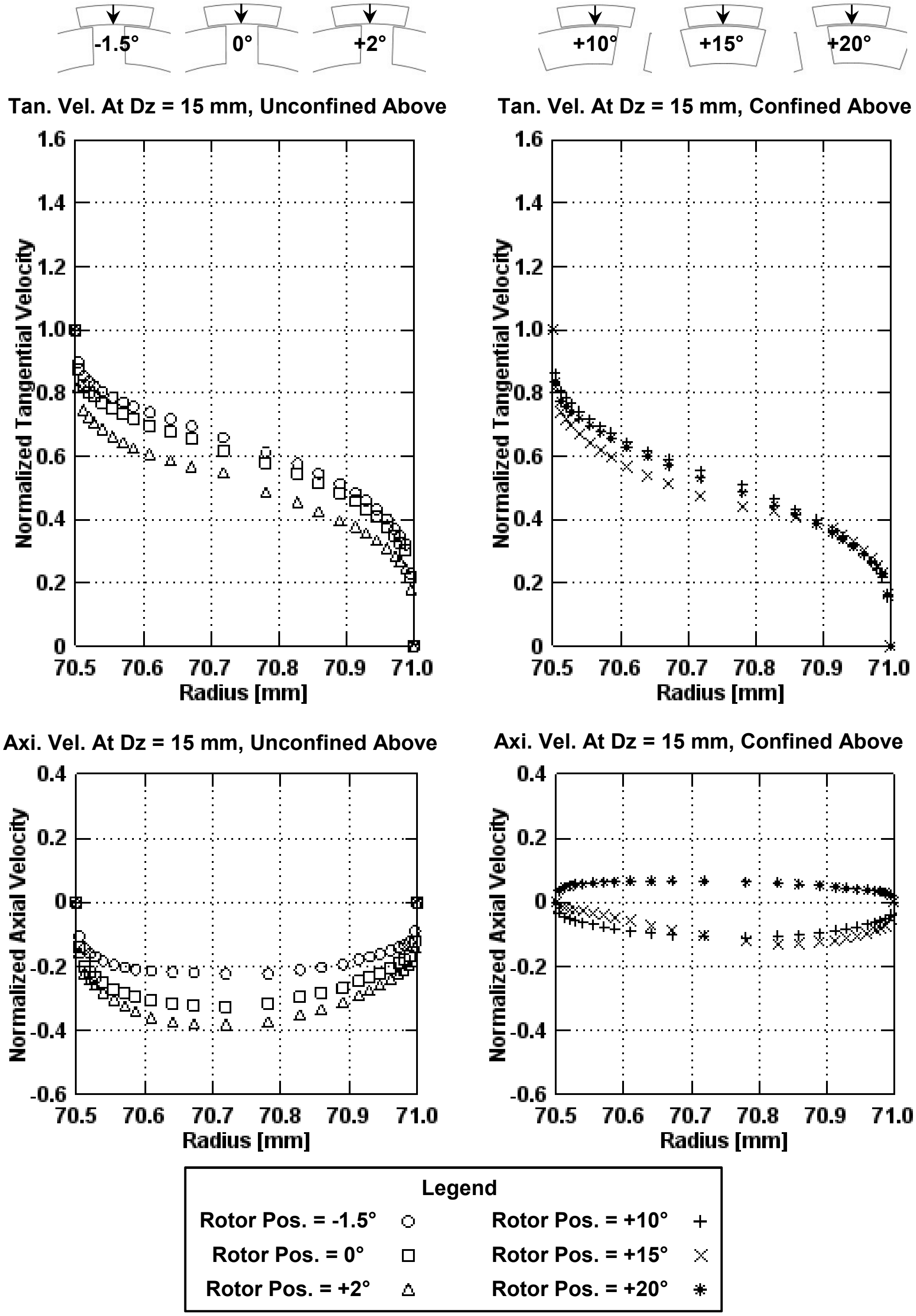

Figure 7.3: Tangential and axial velocity profiles across shear gap at a depth of 15 mm for the high operating scenario (N = 1800 rpm, Q = 2.54 L/s, Level 3 mesh).

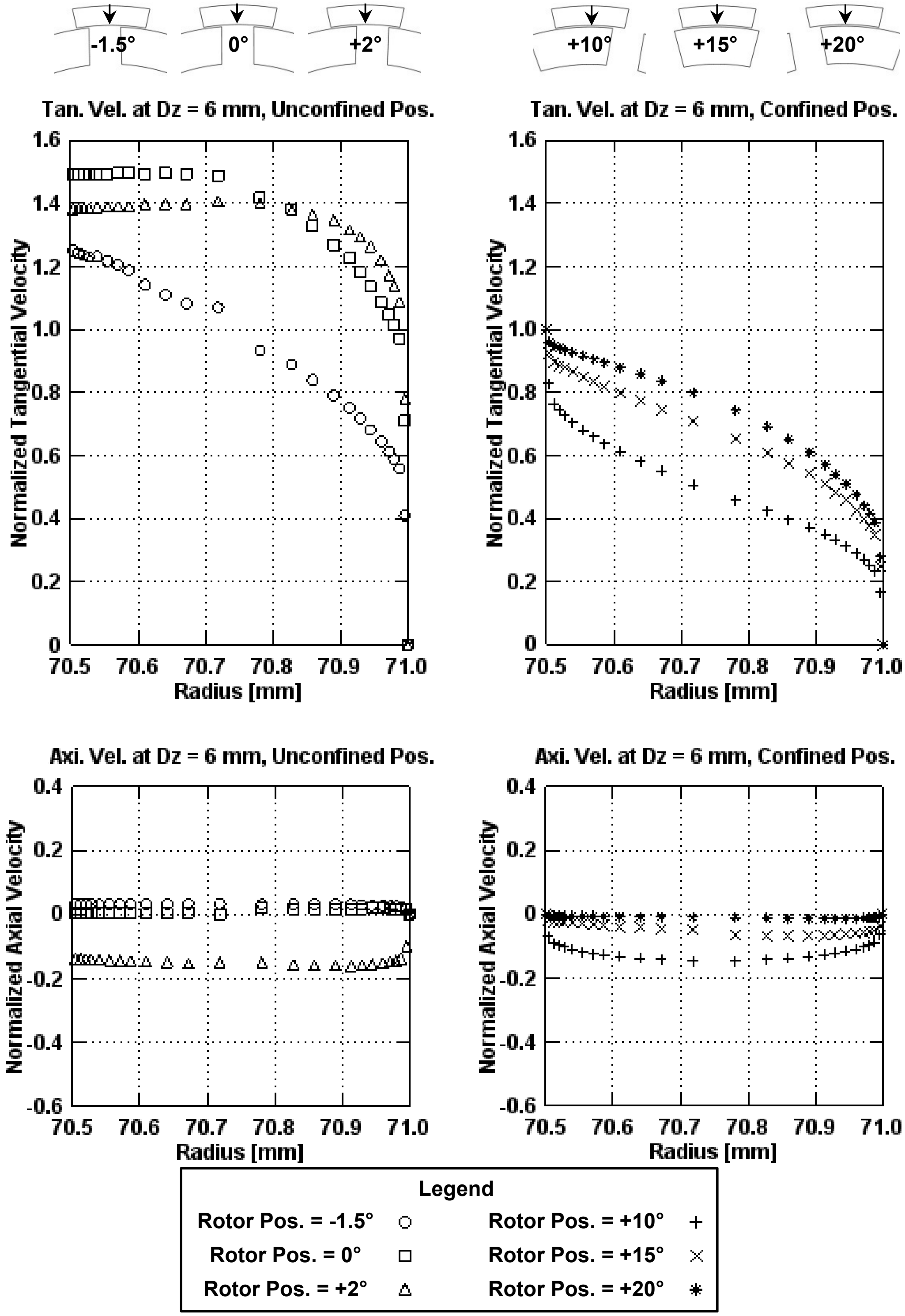

Figure 7.4: Tangential and axial velocity profiles across shear gap at a depth of 6 mm for the high operating scenario ($N = 1800$ rpm, $Q = 2.54$ L/s, Level 3 mesh).

The radial velocities in the rotor positions where the shear gap is confined by the rotor tooth (10°, 20°, and 30°) are less than 1% of rotor tip velocity and are therefore not significant. However, as shown in Figure 7.5, the radial velocity profiles at a depth of 6 mm are significant when the profile is not confined by a rotor tooth. At -1.5°, the radial velocity is negative (i.e., inward toward the centre of the rotor). The radial velocity decreases then increases in the outward direction as the rotor slot sweeps past the shear gap data surface (0° and 2°). Qualitatively, this behaviour is different than that observed for the low operating scenario (see Figure 6.5).

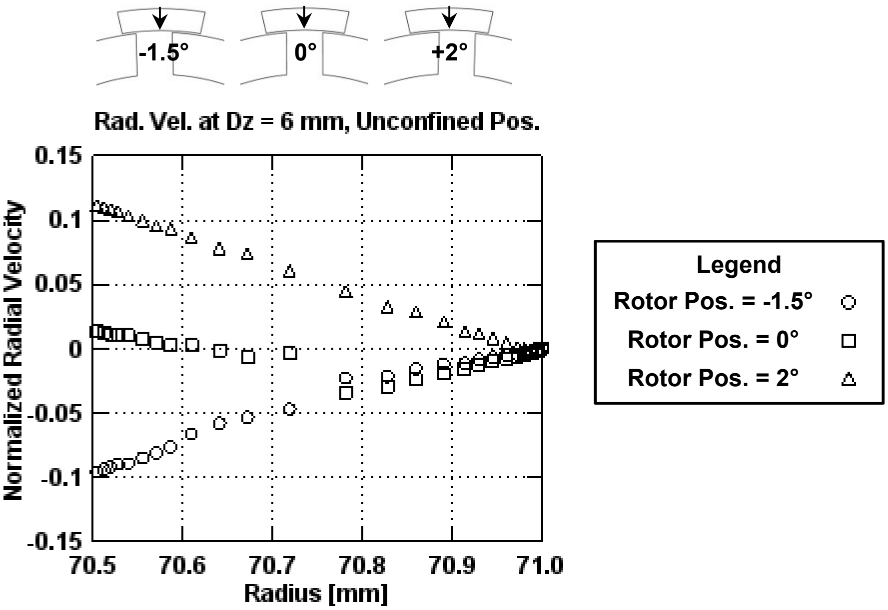

Figure 7.5: Radial velocity profiles across shear gap at a depth of 6 mm for the high operating scenario (N = 1800 rpm, Q = 2.54 L/s, Level 3 mesh).

The behaviour of the fluid on either side of the shear gap is shown in Figure 7.6 for three selected rotor positions (0°, 10°, and 20°). The depth is 6 mm (same depth as the velocity profiles in Figure 7.4 and Figure 7.5). The fluid behaviour is qualitatively similar to that at the low operating scenario. The fluid in the rotor slots again appears to be moving at the same speed or faster than the rotor tip speed (V_{tip} = 13.3 m/s). Across the shear gap for both the 10° and 20° vector plots, the velocity magnitude does not change significantly. A similar high velocity flow through the shear gap occurs for the 0° rotor position as the flow tries to escape the rotor slot.

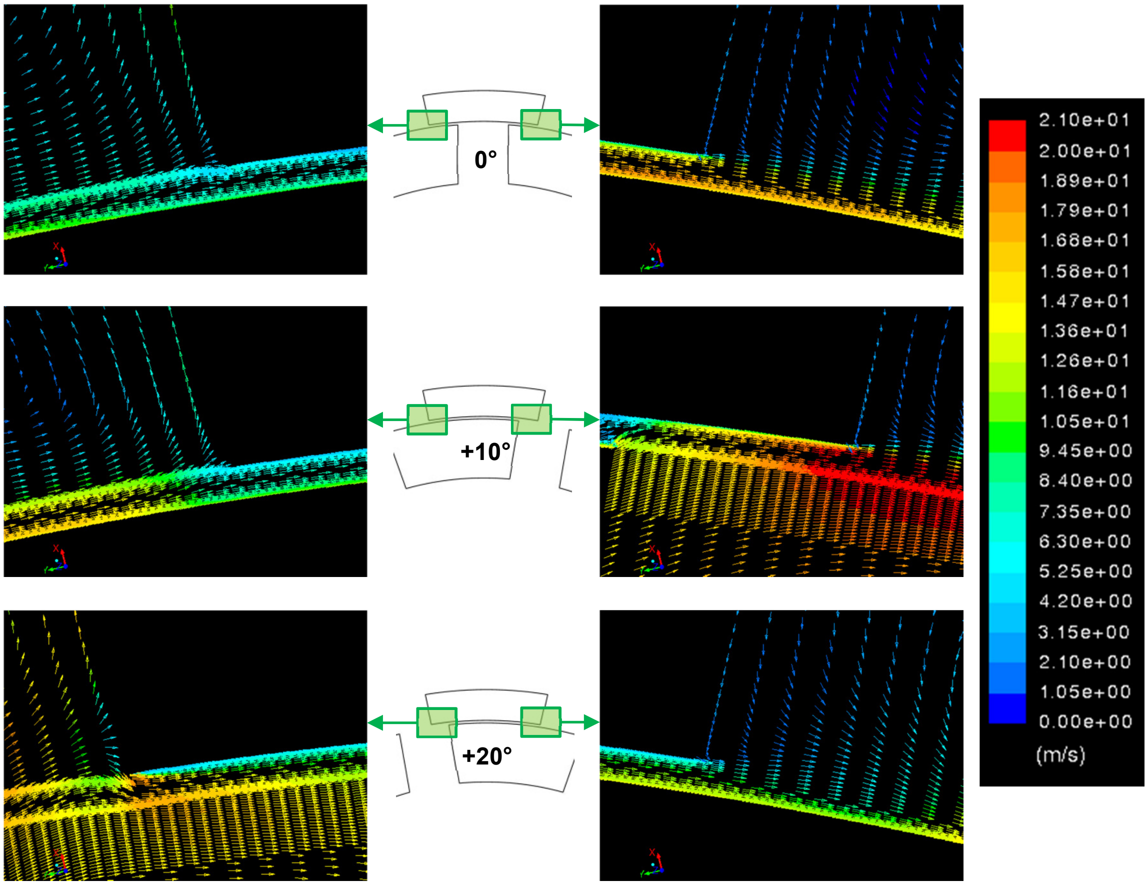

Figure 7.6: Velocity vector plots at corners of the stator slot at selected rotor positions for the high operating scenario (N = 1800 rpm, Q = 2.54 L/s, Level 3 mesh). Plots are at a depth of 6 mm, and vectors are coloured by velocity magnitude.

7.3. Total Deformation Rates on Stator Teeth

The total deformation rate on the stator teeth is plotted against rotor position in Figure 7.7. The dotted line is the mean total deformation rate over all 9216 cells at each rotor position, with dashed lines above and below indicating the maximum and minimum individual cell values.

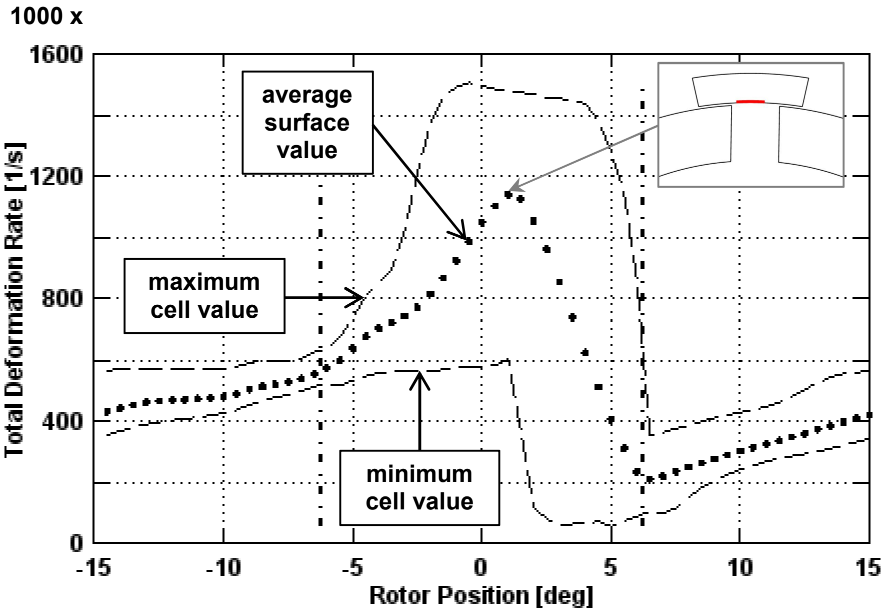

Figure 7.7: Total deformation rates from stator tooth data surface for the high operating scenario (N = 1800 rpm, Q = 2.54 L/s, $\dot{\gamma}$ = 26,630 s^{-1}, Level 3 mesh). The inset illustration shows the rotor position at the peak mean total deformation rate.

When the stator tooth data surface is confined by the rotor tooth (i.e., the rotor tooth 'covers' the data surface, from +6.5° to +15°/-15° to -6.5°), Figure 7.7 shows that the mean total deformation rate over the 6 mm x 6 mm data surface has a wider range of variation than in the low operating scenario (see Figure 6.7). When the shear gap becomes re-confined initially (6.5°), the minimum and maximum predicted deformation rates are -50% and +60%, respectively, of the mean total deformation rate. The mean total deformation rises from 210,700 s^{-1} to 555,500 s^{-1} as the rotor tooth sweeps past the data surface. The variation reaches a minimum of +/-10% just after the trailing edge of the rotor tooth passes the data surface. Note that the nominal shear rate of 26,630 s^{-1} was greatly exceeded at all points on the data surface.

The total deformation rate profile has even greater variation when the rotor slot/opening passes over the data surface. Figure 7.8 presents contour plots of total deformation rate at selected rotor positions. Plot (a) shows that when the rotor tooth passes the data surface, there is a suction region in which the total deformation rate decreases. As the face of the next rotor tooth approaches, there is a sharp increase in the total deformation rate, shown in plots (b) and (c). The peak total deformation rate of 1,143,000 s^{-1} occurs at 1°. As the rotor tooth travels over the data surface, it re-confines and suppresses much of the fluid flow, demonstrated by near-linear drop in plot (d).

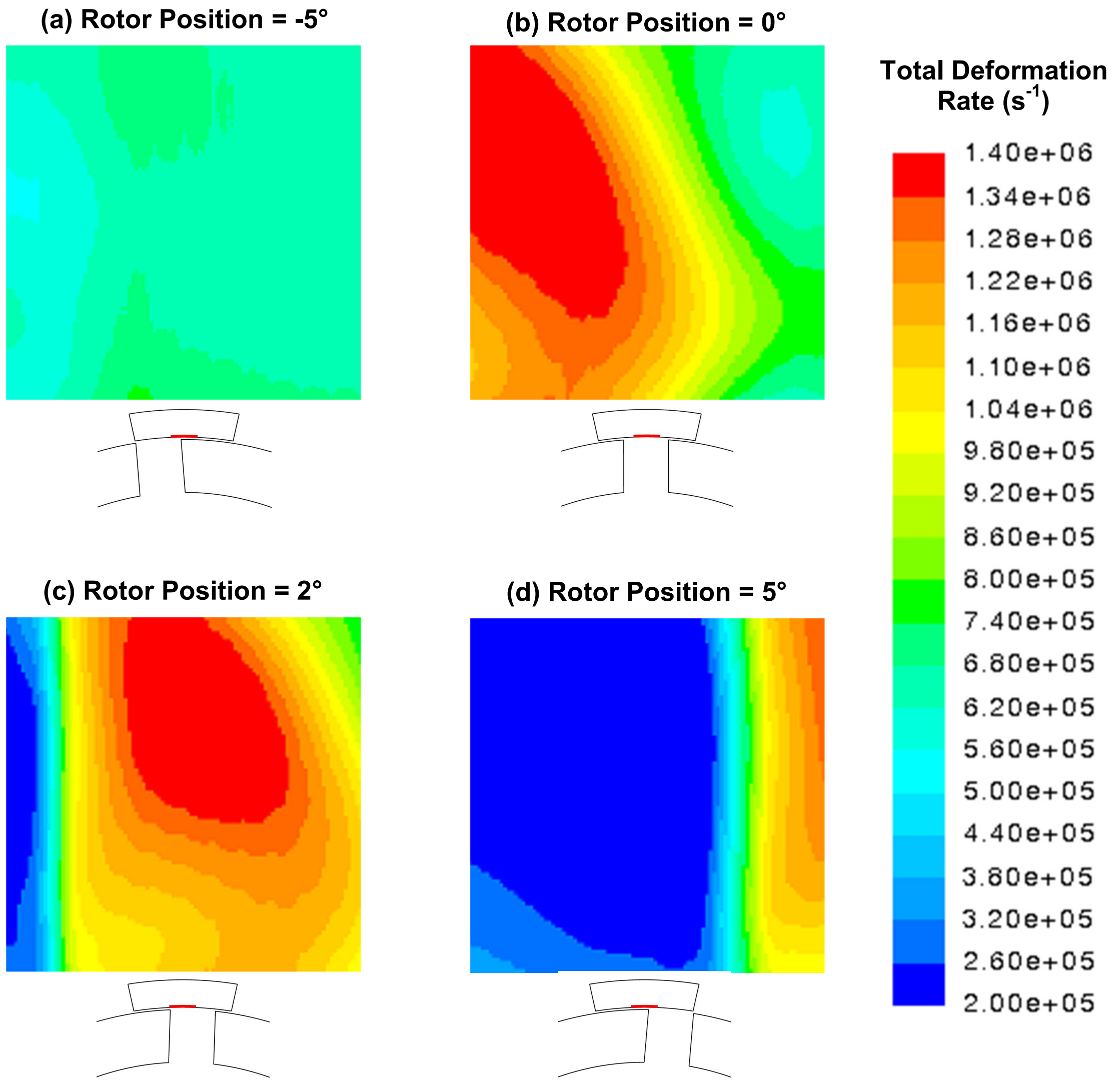

Figure 7.8: Contour plots of total deformation rates when the stator tooth data surface is not completely confined by the rotor tooth for the high operating scenario (N = 1800 rpm, Q = 2.54 L/s, $\dot{\gamma}$ = 26,630 s^{-1}, Level 3 mesh).

7.4. Total Energy Dissipation and Power Draw

Table 7.1 shows the predicted average energy dissipation rates (Equation 2.3-3) for the high operating scenario for each fluid zone. The turbulence dissipation rate is clearly a more significant pathway than the energy dissipation due to mean velocity gradients.

Table 7.1: Average Energy Dissipation Rates for High Operating Scenario (N = 1800 rpm, Q = 2.54 L/s, $\dot{\gamma}$ = 26,630 s^{-1}, Level 3 mesh).

Fluid Zone	Volume [cm^3]	Volumetric Energy Dissipation Rate		Total Energy Dissipation Rate	
		Mean [W/m^3]	Turbulent [W/m^3]	Mean [W]	Turbulent [W]
Rotor Zone	469	14,400	166,000	6.75	77.8
Stator Zone	554	11,800	430,000	6.54	239
Outlet Zone	69.5	698	448,000	0.0485	31.1
Total	1090	12,200	318,000	13.3	347

A summary of the average, minimum, and maximum values of torque, power consumption, and power number are shown in Table 7.2. Note that the power numbers are similar to those obtained for the low operating scenario (see Table 6.2).

Table 7.2: Torque, Power, and Power Number Predictions for High Operating Scenario (N = 1800 rpm, Q = 2.54 L/s, $\dot{\gamma}$ = 26,630 s^{-1}, Level 3 mesh).

Variable	Description	Units	Average Value	Minimum Value	Maximum Value
T	Torque	N-m	2.55	2.45	2.80
P	Power Consumption	W	480	461	528
N_{Po}	Power Number	-	10.2	9.82	11.3

7.5. Summary of Results

In the stator slots, the velocity field is examined at two depths and four rotor positions. When the rotor tooth is blocking the stator slot, there is a great deal of recirculation at the midplane of the slot (D_z = 7 mm). The flow appears to be mostly in radial-tangential plane. At a depth of 1 mm, there is one region where fluid of moderate velocity impinges on the downstream data tooth and another region where fluid is travelling into the stator slot from the volute. When the rotor tooth is not completely blocking the slot, different flow patterns are observed. A vortex is generated off the downstream edge of the upstream stator tooth, and there is a significant amount of flow impinging on the downstream stator tooth.

The velocity components across the shear gap were presented for six rotor positions at depths of 6 mm and 15 mm. At 15 mm depth, where the inner side of the shear gap is always confined by the rotor, there is a minor oscillation in the tangential velocity profiles, although the same general shape is maintained for all rotor positions. With the exception of the 20° rotor position, the axial velocity was predicted to be negative (i.e., away from the volute cover). At 6 mm depth, the overall velocity was dominated by the tangential velocity component. However, just before and just after the leading edge of a rotor tooth passes the data surface, moderate negative axial velocities were observed.

The vector plots of flow patterns at each end of the shear gap showed similar qualitative behaviour compared to the low operating scenario. The velocity magnitude does not change significantly in the tangential direction along a continuous region of the shear gap. When the rotor slot is blocked by the stator tooth, there is an increase in fluid velocity in the shear gap section downstream of the rotor slot.

The average, minimum, and maximum values for the total deformation rate profile were quantified with respect to mean, maximum, and minimum values over the stator tooth data surface. The predicted total deformation rates always exceeded the nominal shear rate of 26,630 s^{-1} by a factor of almost 8. In rotor positions where the shear gap is confined by the rotor tooth, the total deformation rate on the data surface was not constant; instead, it increased with time. There was also a substantial amount of variation in the total deformation rates over the surface, unlike in the low operating scenario (see Section 6.3). When the trailing edge of the rotor passes over the data surface, there is a period of lower deformation rates. This is followed by a pulse of high deformation ahead of the leading edge of the next rotor tooth.

The energy dissipation in the IKA prototype was evaluated using the total deformation rates and turbulence dissipation rates outputted by FLUENT. A total of 360 W is dissipated in the three fluid zones in the simulation. The energy dissipation due to mean velocity gradients is only 3.6% of the total, and thus is negligible in many applications. The average power consumption from the rotor is 480 W, and the average power number is 10.2.

8. Summary, Conclusions, and Recommendations

This chapter presents the key observations and conclusions from each phase of this project. Also presented are recommendations to further develop knowledge of fluid behaviour in rotor-stator mixers.

8.1. Summary of Project Objectives and Methodologies

The objective of this project was to further develop an existing CFD model of the IKA prototype rotor-stator mixer. With these models, detailed information on the velocity field within the stator slots and shear gap, total deformation on stator teeth, and dissipation of power was sought for two operating scenarios. The two operating scenarios were chosen to represent a generally low condition (low speed, low flow rate) and a generally high condition (high speed, high flow rate).

Because of the transient and time-periodic nature of the flow, the IKA prototype mixer was modelled using the sliding mesh simulation technique. Turbulence was modelled with the realizable k-ε model and non-equilibrium wall functions. All simulations were based on the RANS equations and were conducted with the commercial CFD software FLUENT.

8.2. Convergence and Grid Independence

The purpose of the grid independence study was to verify the convergence of the conducted simulations and determine the level of mesh refinement for which the flow solution was independent of the grid geometry.

- It was demonstrated that the convergence behaviour of the flow field depend on the region of interest in the rotor-stator mixer. For all six simulations, convergence in the tightly-confined shear gap was faster than in the stator slots that were larger and open to the volute. For five of the six simulations run, the relative change between the reported periods for the shear gap were at least a factor of 2 lower than the relative change in the stator slots. In one simulation, the relative change in the shear gap was about 20% lower than the relative change in the stator slots.

- Grid independence was found to depend on the parameters of the operating scenario. For the low operating scenario (N = 300 rpm, Q = 0.315 L/s), grid independence was established with 20 cells across the shear gap and 10 million cells overall. For the high operating scenario (N = 1800 rpm, Q = 2.54 L/s), grid independence was not established. Simulations were conducted based on the most refined grid (24 cells across the shear gap and 24 million cells overall) practical to run with the current computational resources.

- For the low operating scenario, reaching convergence in only the shear gap requires about 12 revolutions. If convergence in the stator slots is also desired, about 20 revolutions are needed.

- For the high operating scenario, reaching convergence in only the shear gap requires about 16 revolutions. If convergence in the stator slots is also desired, about 24 revolutions are needed.

8.3. Low Operating Scenario

The flow characteristics for the low operating scenario were investigated in further detail using the Level 2 mesh (20 cells across the shear gap and 10 million cells overall), for which the solution was previously found to be grid independent.

- From the benchmark simulations of Couette channel flow, it was found that when simulating laminar flow conditions, turbulent simulations (with the realizable k-ε model) produced different velocity profiles than laminar flow simulations. Applying turbulence models to laminar flow was therefore found to be a source of numerical error in the computational simulation.

- The velocity profile in the shear gap of the IKA prototype mixer, at this low angular speed, was similar to velocity profiles from the simulation of laminar Couette channel flow with realizable k-ε turbulence model. However, given the complex nature of flow in the shear gap caused by the periodicity of the rotor, it cannot be determined whether the flow in the shear gap is indeed laminar without experimental validation.

- Flow patterns within the stator slots were shown to be three dimensional. When the stator slot is fully blocked by a rotor tooth, the primary flow pattern appeared to be circular in the plane normal to the axial direction. There was also circulation of flow near the upstream stator tooth in the plane normal to the radial direction. When the stator slot is partly open to the rotor slot, circulation of flow within the stator slot is primarily at the downstream edge of the upstream stator tooth due to the impingement of flow on the downstream stator tooth.

- Flow patterns within the shear gap were shown to be primarily in the tangential direction. At a depth of 15 mm, where the shear gap data surface is always confined by both the rotor and the stator, the magnitude of the tangential velocity oscillates slightly within the rotor period. At a depth of 6 mm, where the shear gap data surface is directly affected by the travelling rotor teeth, velocity was found to increase throughout the period until leading edge of the rotor tooth imposed additional boundary conditions on the flow. When the shear gap data surface was not confined by the rotor tooth, axial velocity was shown to be significant at 15 mm depth, and radial velocity was shown to be significant at 6 mm depth.

- Total deformation rates on the stator tooth surface were shown to be greater than the nominal shear rate for all rotor positions. When confined by the rotor tooth, the total deformation rates across the data surface were spatially uniform and steadily increasing with rotor position (or time). When the rotor tooth was not confining (or covering) the stator tooth data surface, there were significant spatial variations across the surface, with the highest total deformation rates just ahead of the leading edge of the approaching rotor tooth.

- The average energy dissipation rate was predicted to be 1.84 W, with 0.33 W due mean velocity gradients and 1.51 W due to dissipation of turbulence. The average power consumption of the rotor, based on torque predictions, was calculated to be 2.24 W. The average power number is 10.3.

8.4. High Operating Scenario

The flow characteristics for the high operating scenario were investigated in further detail using the Level 3 mesh (24 cells across the shear gap and 24 million cells overall). This mesh is the largest size that can be practically built and run with the currently available computational resources, but has not been verified to be grid independent.

- When the stator slot is blocked by the rotor tooth, the flow patterns near the midplane of the stator slot (depth of 7 mm) appeared to be primarily circular in the plane normal to the axial direction. At the depth of 1 mm, there is a region where a fluid jet impinges on the stator tooth and another region where the fluid travels into the stator slot from the volute. When the stator slot is partly open to the rotor slot, a vortex is generated off the downstream edge of the upstream stator tooth, and there is a significant amount of flow impinging on the downstream stator tooth.

- Flow patterns within the shear gap were shown to be primarily in the tangential and axial directions. At 15 mm depth, where the shear gap data surface is fully-confined by the rotor and stator, the magnitude of the tangential velocity oscillates slightly within the rotor period. Axial velocity is mostly negative at the centerline of the stator tooth. At the 6 mm depth, where the time-periodic travel of the rotor tooth will directly influence the shear gap data surface, tangential velocity was found to increase through most of the rotor period. Tangential velocity decreased as the rotor tooth neared and re-confined the data surface. Axial velocity was generally significant at most positions and heights. Radial velocity was shown to be significant only at depths exposed directly to an open rotor slot.

- Total deformation rates on the stator tooth surface were shown to be greater than the nominal shear rate for all rotor positions. When the stator tooth data surface was confined (or covered) by the rotor tooth, the total deformation rates were generally increasing, with a moderate amount of spatial variation. When the stator tooth data surface was not confined (or only partially confined) by a rotor tooth, there was a greater degree of spatial variations across the surface, with the highest mean total deformation rates just ahead of the rotor tooth.

- The average energy dissipation rate was predicted to be 360 W, with 13 W due mean velocity gradients and 347 W due to dissipation of turbulence. The energy dissipation due to mean velocity gradients was thus judged to be a much less significant pathway than through turbulence dissipation. The average power consumption of the rotor, based on torque predictions, was calculated to be 480 W. The average power number is 10.2.

8.5. Comparison between the Low and High Operating Scenarios

This section highlights some notable differences between the solutions to the low and high operating scenarios.

- In the stator slots, the qualitative patterns of the velocity magnitude vectors were generally similar between the low and high operating scenarios. The primary difference seems to be for depths near the volute cover (D_z = 1 mm) when the stator slot is blocked by a rotor tooth. The low operating scenario shows a circulation of flow within the stator slot, while the high operating scenario shows more of a jetting phenomenon.
- In the shear gap, there are differences in tangential velocity profiles at depths of 6 mm (where the profiles are directly affected by the rotor teeth/slots). Tangential velocities for the high operating scenario are generally higher than in the low operating scenario, and the shape of the profiles when confined by the rotor teeth suggest that pressure was also a driving force in the high operating scenario. Axial velocities for the high operating scenario tended to be of higher magnitude (but same direction). The behaviour of the radial velocity profiles at depths of 6 mm as a function of rotor position was very different. For the low operating scenario, the radial velocities started at about neutral, increased in the negative direction (toward the centre of the apparatus), and then reversed direction to be slightly positive in the positive direction as the rotor slot travelled past the data surface. This oscillation was not seen in the high operating scenario, where the radial velocity started negative, went neutral, and then became positive as the rotor slot travelled past the data surface.

- The mean total deformation rate profiles are qualitatively similar. The high operating scenario has a higher degree of variation when the stator tooth data surface is confined by a rotor tooth. In contrast, the stator tooth data surface is spatially uniform in the low operating scenario when confined by the rotor tooth.

8.6. Recommended Future Work

A number of areas were identified during his project that would benefit from additional investigation.

- As additional computational resources become available, the grid for the high operating scenario (1800 rpm) should be further refined to verify whether grid independence has been reached.
- CFD simulation results should be compared to PIV measurements to validate the flow behaviour and appropriateness of the selected mathematical models. This would involve conducting simulations with the exact geometry and flow conditions of the PIV experiments, which were between the low and high operating scenarios in this work.
- If further work with the low operating scenario is desired, additional study will be needed to determine whether the flows in the shear gap are laminar. The 0.5 mm shear gap may be too narrow to conduct PIV measurements, but the wider 4 mm gap studied by Kevala (2001) can be used to measure shear gap velocities at a range of typically-laminar Reynolds numbers. If the velocity profiles are seen to be more like the plane Couette flow case, then CFD model will need to be modified. One potential direction would be to implement a method for deactivating the generation of turbulent kinetic energy in the shear gap. This could involve calculating turbulent kinetic energy generation in the gap with a user-defined function.

Appendix A – Grid Independence Tangential Velocity Plots

Appendix A contains the grid independence comparisons of tangential velocity profiles across the shear gap data surface for both operating scenarios. Refer to Section 4.4 for more information on the shear gap data surface. A list of figures in this appendix is below.

Figure A.1: Comparison of tangential velocity in the shear gap, at 3 mm depth, between Level 1, Level 2, and Level 3 meshes for the low operating scenario (N = 300 rpm, Q = 0.315 L/s).

Figure A.2: Comparison of tangential velocity in the shear gap, at 6 mm depth, between Level 1, Level 2, and Level 3 meshes for the low operating scenario (N = 300 rpm, Q = 0.315 L/s).

Figure A.3: Comparison of tangential velocity in the shear gap, at 9 mm depth, between Level 1, Level 2, and Level 3 meshes for the low operating scenario (N = 300 rpm, Q = 0.315 L/s).

Figure A.4: Comparison of tangential velocity in the shear gap, at 12 mm depth, between Level 1, Level 2, and Level 3 meshes for the low operating scenario (N = 300 rpm, Q = 0.315 L/s).

Figure A.5: Comparison of tangential velocity in the shear gap, at 15 mm depth, between Level 1, Level 2, and Level 3 meshes for the low operating scenario (N = 300 rpm, Q = 0.315 L/s).

Figure A.6: Comparison of tangential velocity in the shear gap, at 3 mm depth, between Level 1, Level 2, and Level 3 meshes for the high operating scenario (N = 1800 rpm, Q = 2.54 L/s).

Figure A.7: Comparison of tangential velocity in the shear gap, at 6 mm depth, between Level 1, Level 2, and Level 3 meshes for the high operating scenario (N = 1800 rpm, Q = 2.54 L/s).

Figure A.8: Comparison of tangential velocity in the shear gap, at 9 mm depth, between Level 1, Level 2, and Level 3 meshes for the high operating scenario (N = 1800 rpm, Q = 2.54 L/s).

Figure A.9: Comparison of tangential velocity in the shear gap, at 12 mm depth, between Level 1, Level 2, and Level 3 meshes for the high operating scenario (N = 1800 rpm, Q = 2.54 L/s).

Figure A.10: Comparison of tangential velocity in the shear gap, at 15 mm depth, between Level 1, Level 2, and Level 3 meshes for the high operating scenario (N = 1800 rpm, Q = 2.54 L/s).

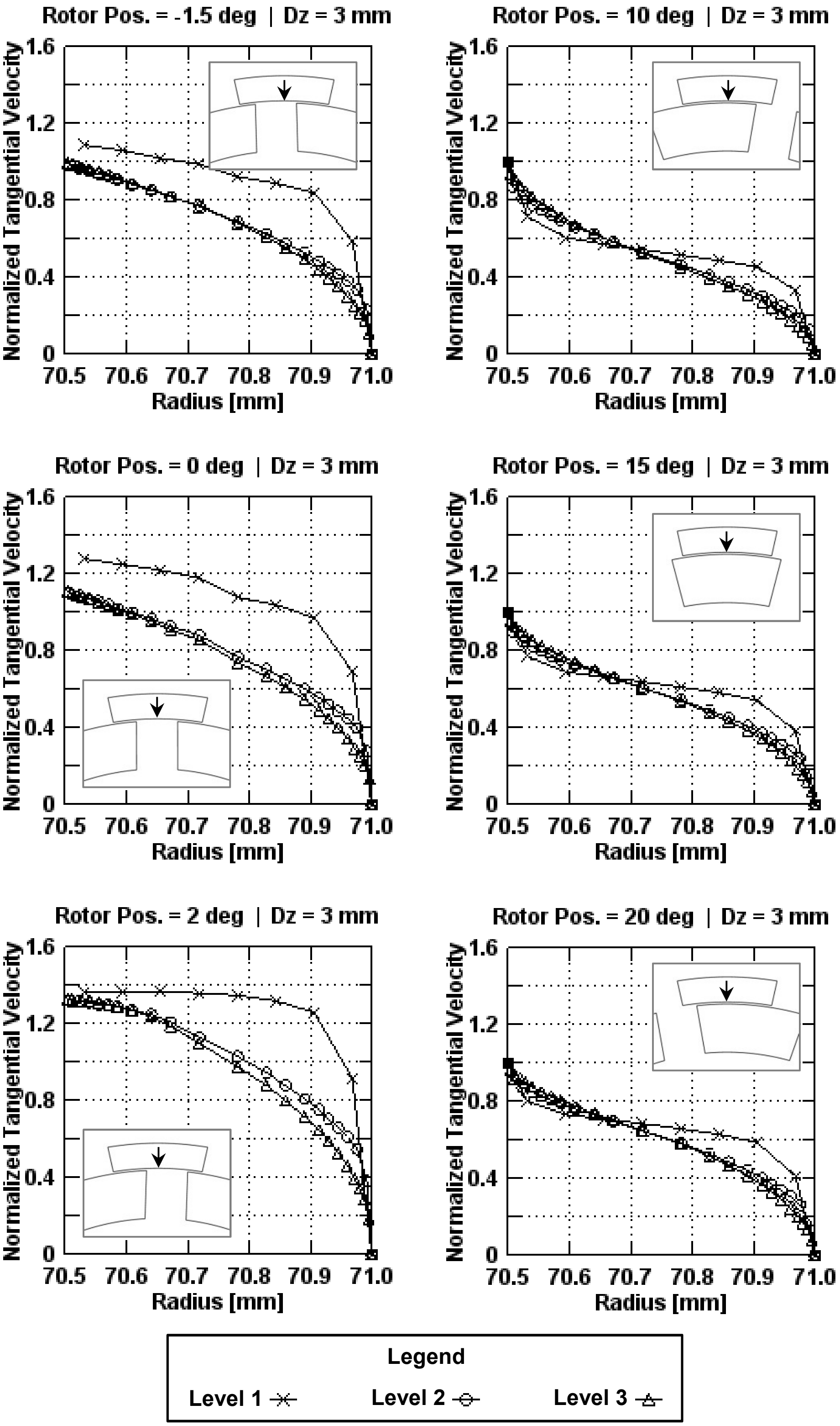

Figure A.1: Comparison of tangential velocity in the shear gap, at 3 mm depth, between Level 1, Level 2, and Level 3 meshes for the low operating scenario ($N = 300$ rpm, $Q = 0.315$ L/s).

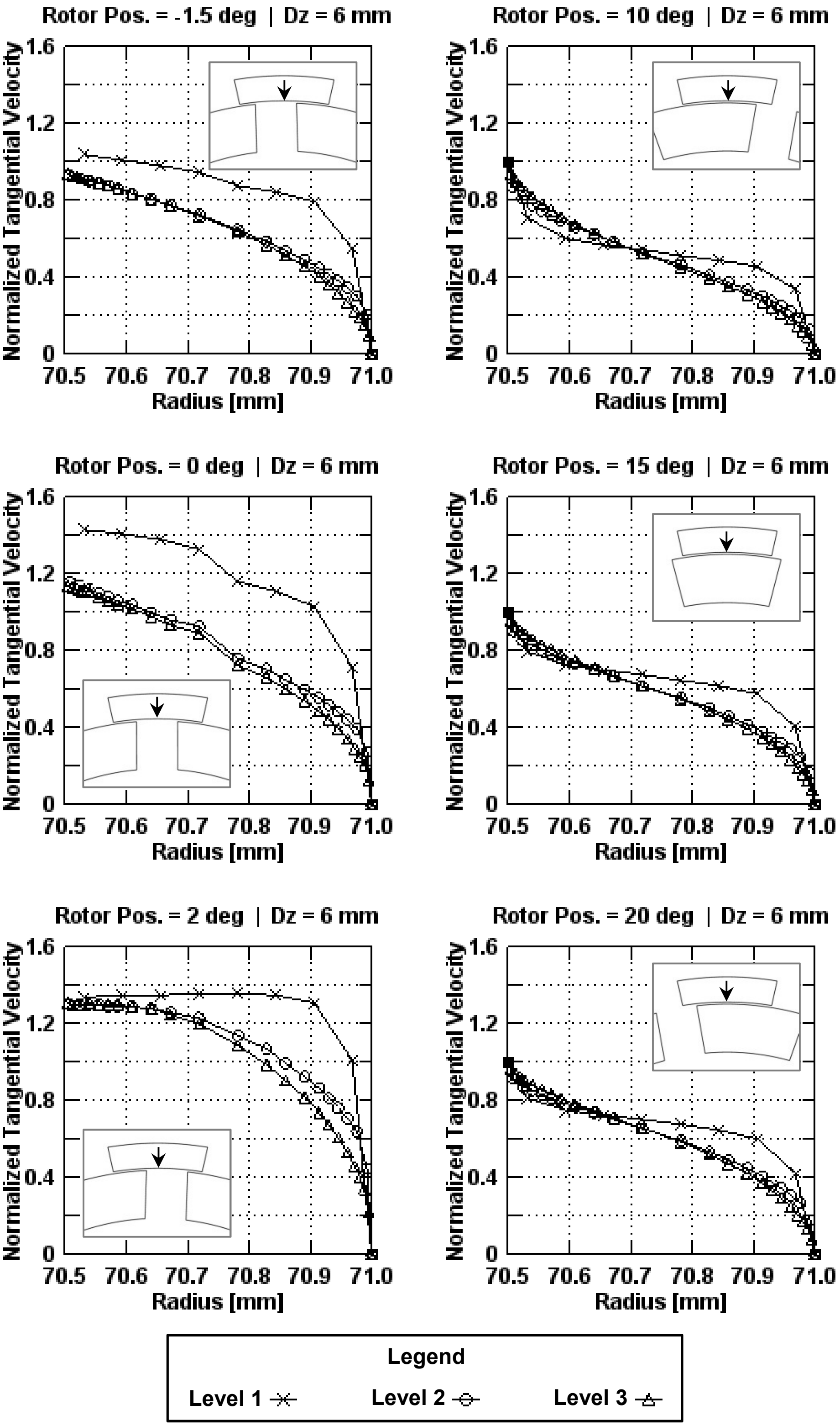

Figure A.2: Comparison of tangential velocity in the shear gap, at 6 mm depth, between Level 1, Level 2, and Level 3 meshes for the low operating scenario (N = 300 rpm, Q = 0.315 L/s).

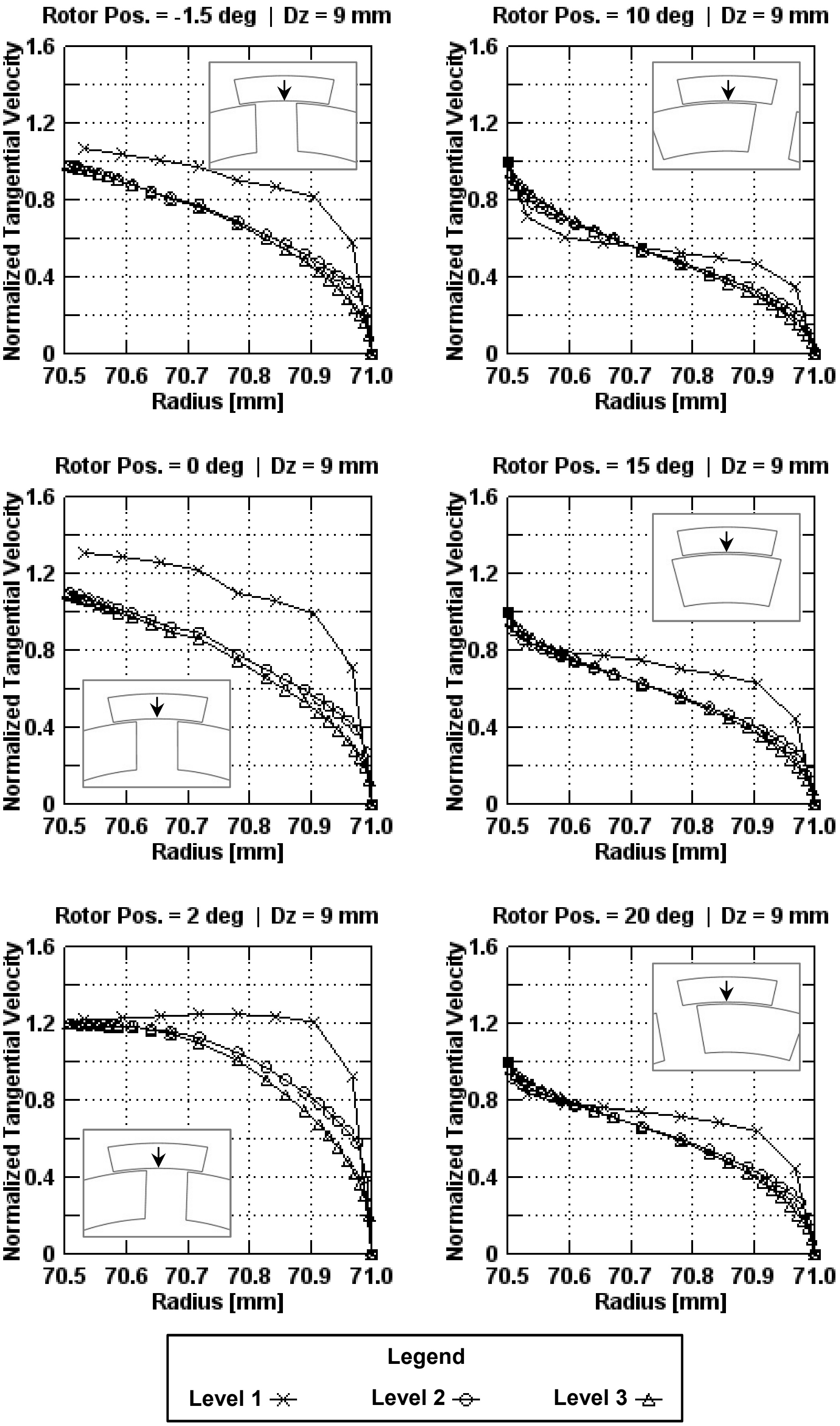

Figure A.3: Comparison of tangential velocity in the shear gap, at 9 mm depth, between Level 1, Level 2, and Level 3 meshes for the low operating scenario (*N* = 300 rpm, *Q* = 0.315 L/s).

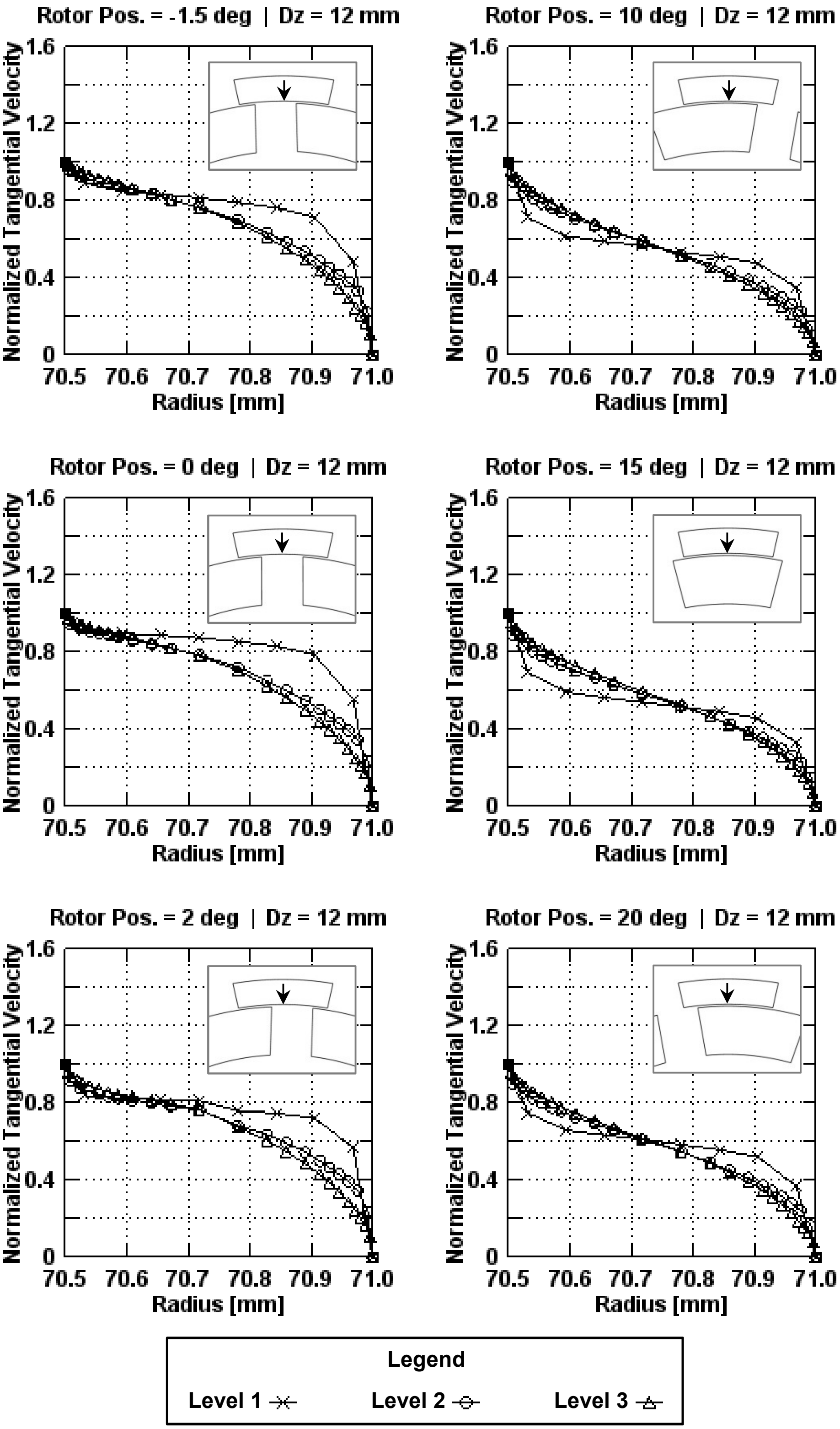

Figure A.4: Comparison of tangential velocity in the shear gap, at 12 mm depth, between Level 1, Level 2, and Level 3 meshes for the low operating scenario (N = 300 rpm, Q = 0.315 L/s).

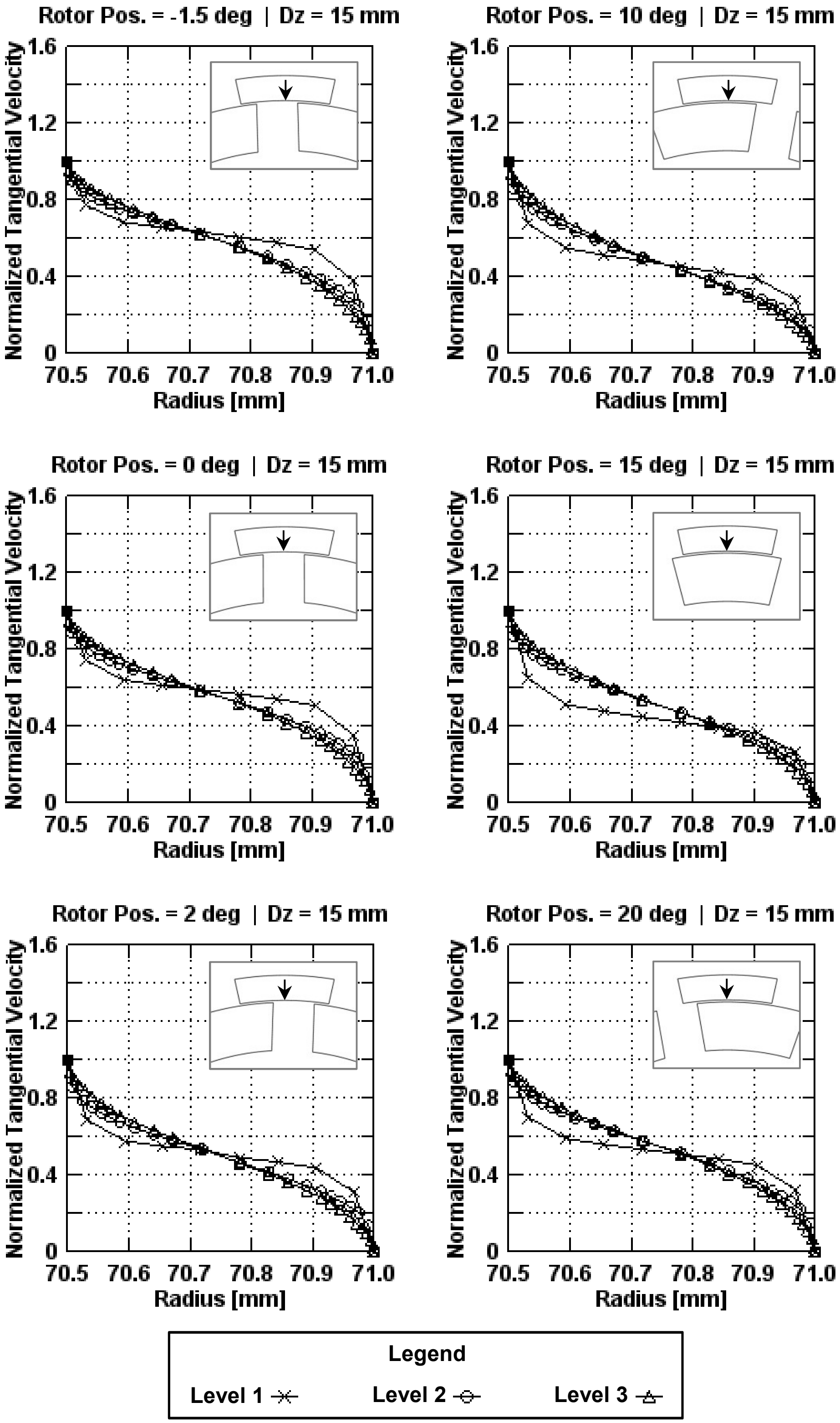

Figure A.5: Comparison of tangential velocity in the shear gap, at 15 mm depth, between Level 1, Level 2, and Level 3 meshes for the low operating scenario (N = 300 rpm, Q = 0.315 L/s).

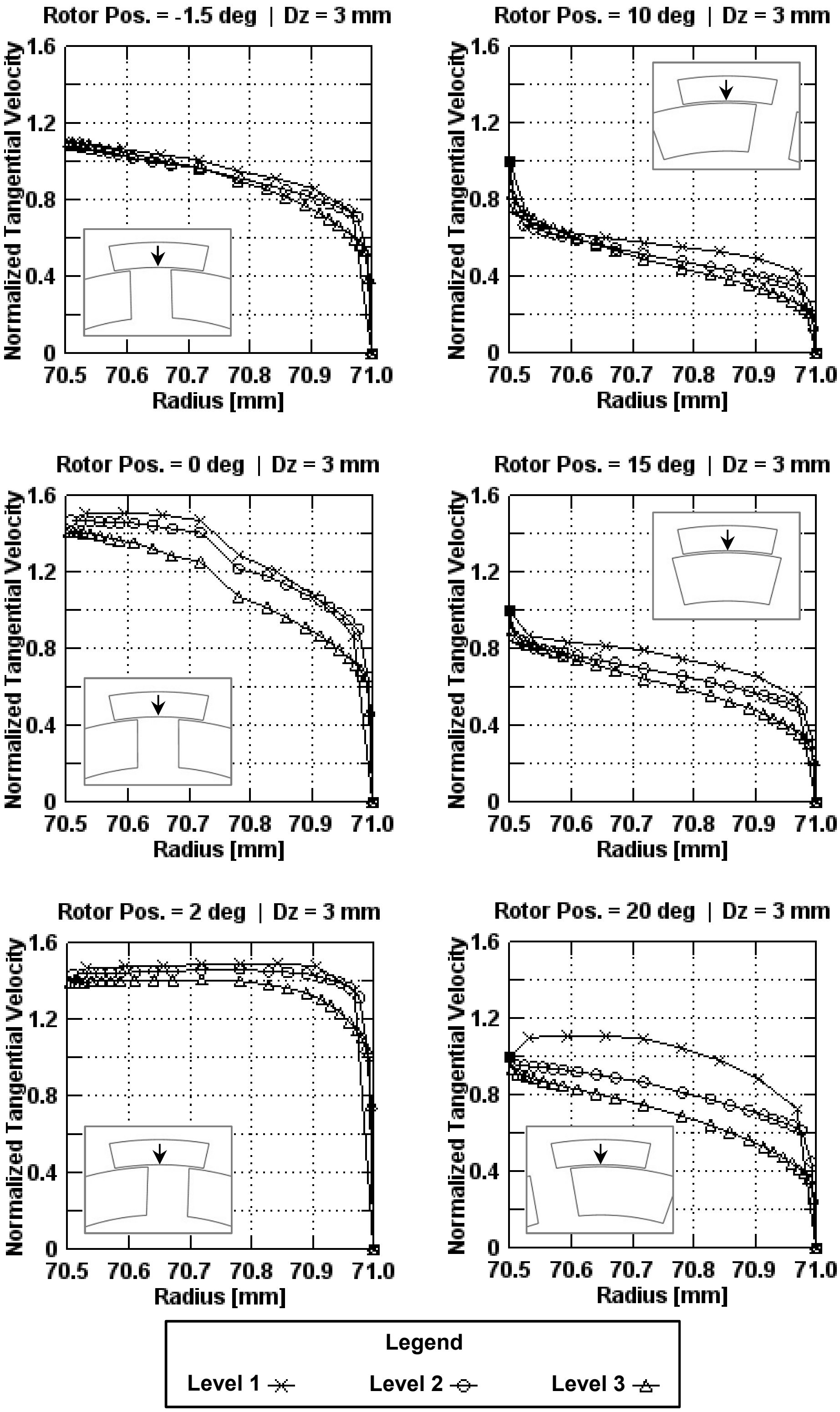

Figure A.6: Comparison of tangential velocity in the shear gap, at 3 mm depth, between Level 1, Level 2, and Level 3 meshes for the high operating scenario ($N = 1800$ rpm, $Q = 2.54$ L/s).

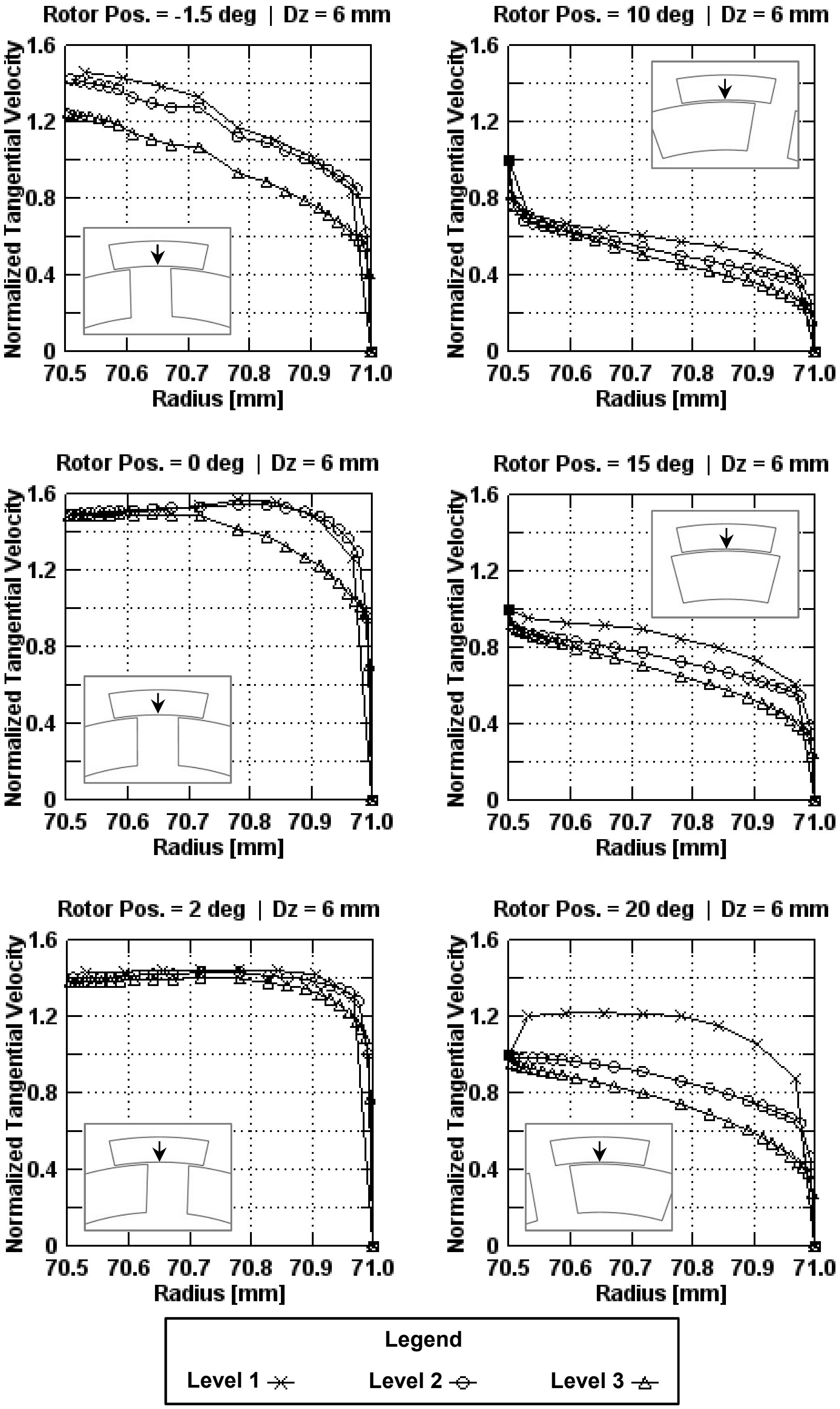

Figure A.7: Comparison of tangential velocity in the shear gap, at 6 mm depth, between Level 1, Level 2, and Level 3 meshes for the high operating scenario (N = 1800 rpm, Q = 2.54 L/s).

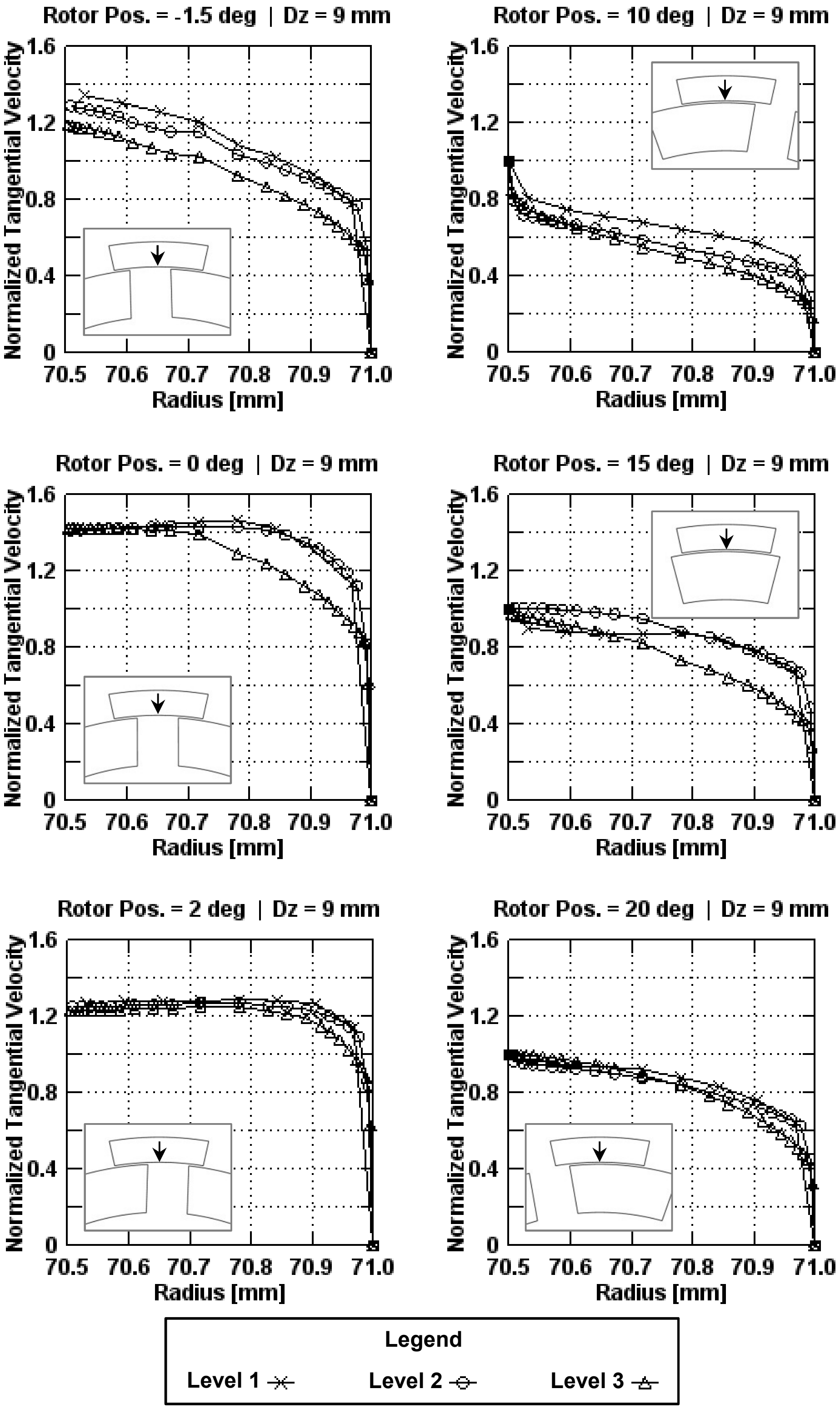

Figure A.8: Comparison of tangential velocity in the shear gap, at 9 mm depth, between Level 1, Level 2, and Level 3 meshes for the high operating scenario ($N = 1800$ rpm, $Q = 2.54$ L/s).

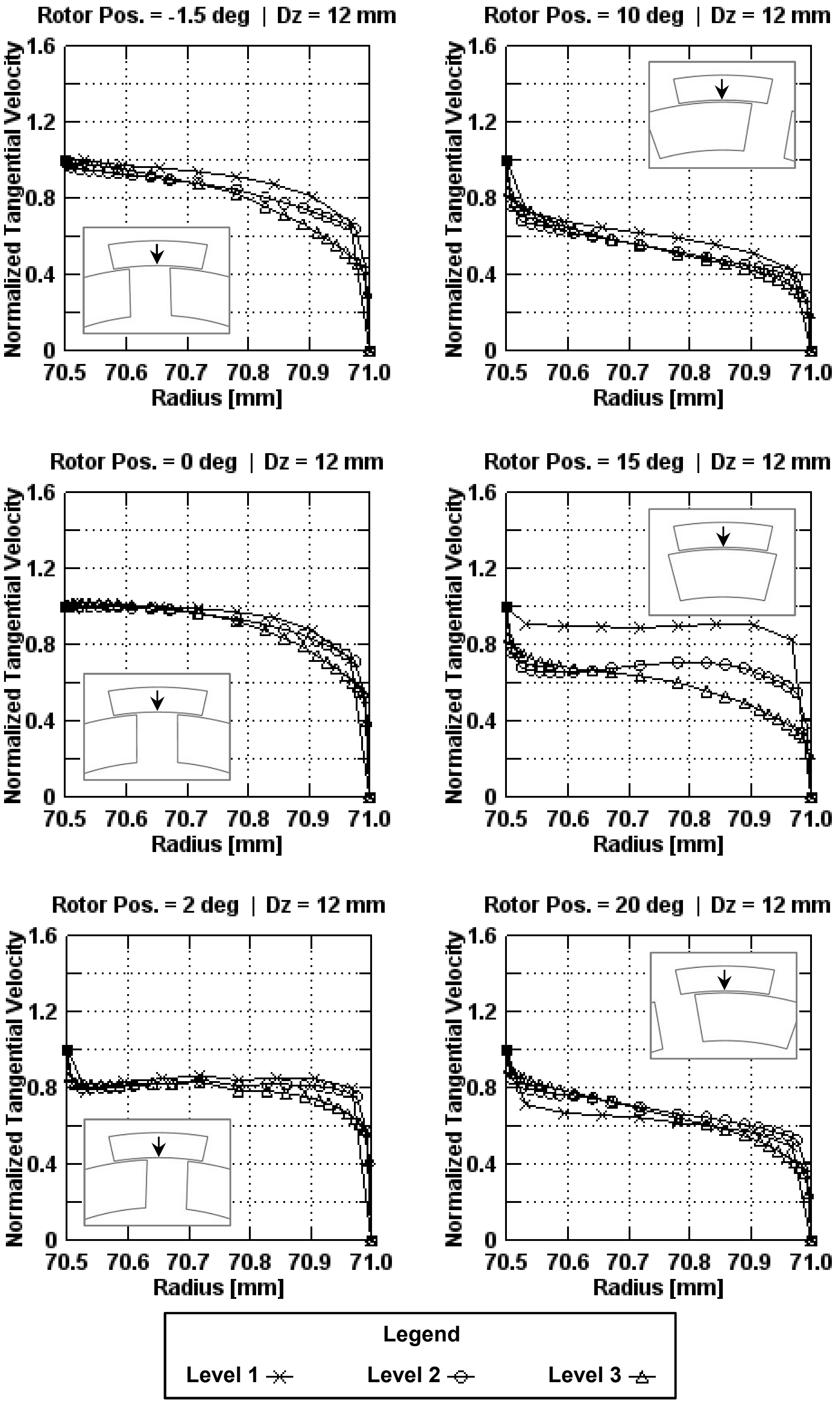

Figure A.9: Comparison of tangential velocity in the shear gap, at 12 mm depth, between Level 1, Level 2, and Level 3 meshes for the high operating scenario (*N* = 1800 rpm, *Q* = 2.54 L/s).

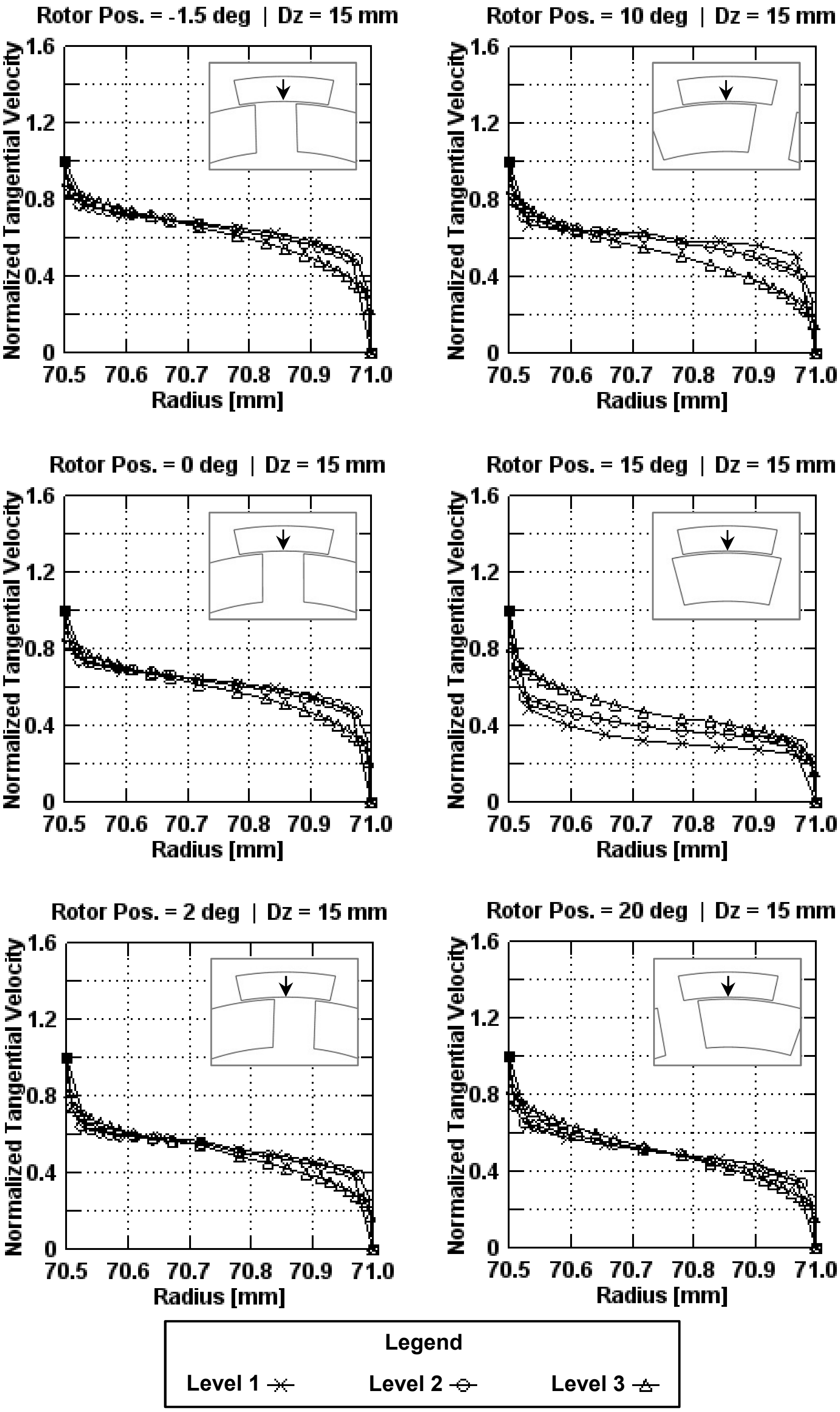

Figure A.10: Comparison of tangential velocity in the shear gap, at 15 mm depth, between Level 1, Level 2, and Level 3 meshes for the high operating scenario (*N* = 1800 rpm, *Q* = 2.54 L/s).

Appendix B – Complete Shear Gap Velocity Profiles

Appendix B contains the complete set of tangential, axial, and radial velocity profiles across the shear gap data surface for both operating scenarios. Refer to Section 4.4 for more information on the shear gap data surface. A list of figures in this appendix is below.

Figure B.1: Tangential and axial velocity profiles across shear gap at a depth of 3 mm for the low operating scenario (*N* = 300 rpm, *Q* = 0.315 L/s, Level 2 mesh).

Figure B.2: Tangential and axial velocity profiles across shear gap at a depth of 6 mm for the low operating scenario (*N* = 300 rpm, *Q* = 0.315 L/s, Level 2 mesh).

Figure B.3: Tangential and axial velocity profiles across shear gap at a depth of 9 mm for the low operating scenario (*N* = 300 rpm, *Q* = 0.315 L/s, Level 2 mesh).

Figure B.4: Tangential and axial velocity profiles across shear gap at a depth of 12 mm for the low operating scenario (*N* = 300 rpm, *Q* = 0.315 L/s, Level 2 mesh).

Figure B.5: Tangential and axial velocity profiles across shear gap at a depth of 15 mm for the low operating scenario (*N* = 300 rpm, *Q* = 0.315 L/s, Level 2 mesh).

Figure B.6: Radial velocity profiles across shear gap at depths of 3, 6, and 9 mm for the low operating scenario (*N* = 300 rpm, *Q* = 0.315 L/s, Level 2 mesh).

Figure B.7: Tangential and axial velocity profiles across shear gap at a depth of 3 mm for the high operating scenario (*N* = 1800 rpm, *Q* = 2.54 L/s, Level 3 mesh).

Figure B.8: Tangential and axial velocity profiles across shear gap at a depth of 6 mm for the high operating scenario (*N* = 1800 rpm, *Q* = 2.54 L/s, Level 3 mesh).

Figure B.9: Tangential and axial velocity profiles across shear gap at a depth of 9 mm for the high operating scenario (*N* = 1800 rpm, *Q* = 2.54 L/s, Level 3 mesh).

Figure B.10: Tangential and axial velocity profiles across shear gap at a depth of 12 mm for the high operating scenario (*N* = 1800 rpm, *Q* = 2.54 L/s, Level 3 mesh).

Figure B.11: Tangential and axial velocity profiles across shear gap at a depth of 15 mm for the high operating scenario (*N* = 1800 rpm, *Q* = 2.54 L/s, Level 3 mesh).

Figure B.12: Radial velocity profiles across shear gap at depths of 3, 6, 9, and 12 mm for the high operating scenario (*N* = 1800 rpm, *Q* = 2.54 L/s, Level 3 mesh).

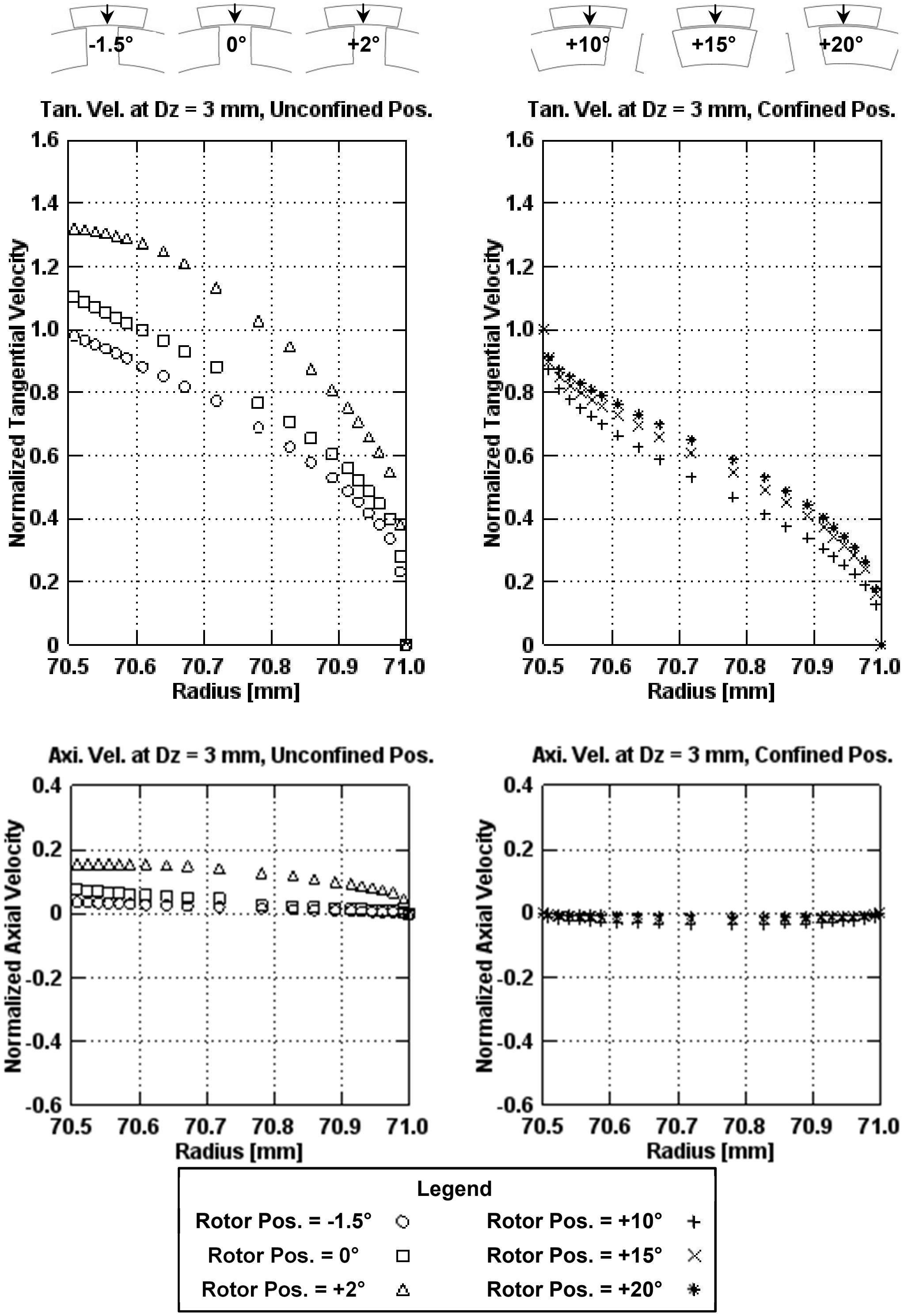

Figure B.1: Tangential and axial velocity profiles across shear gap at a depth of 3 mm for the low operating scenario ($N = 300$ rpm, $Q = 0.315$ L/s, Level 2 mesh).

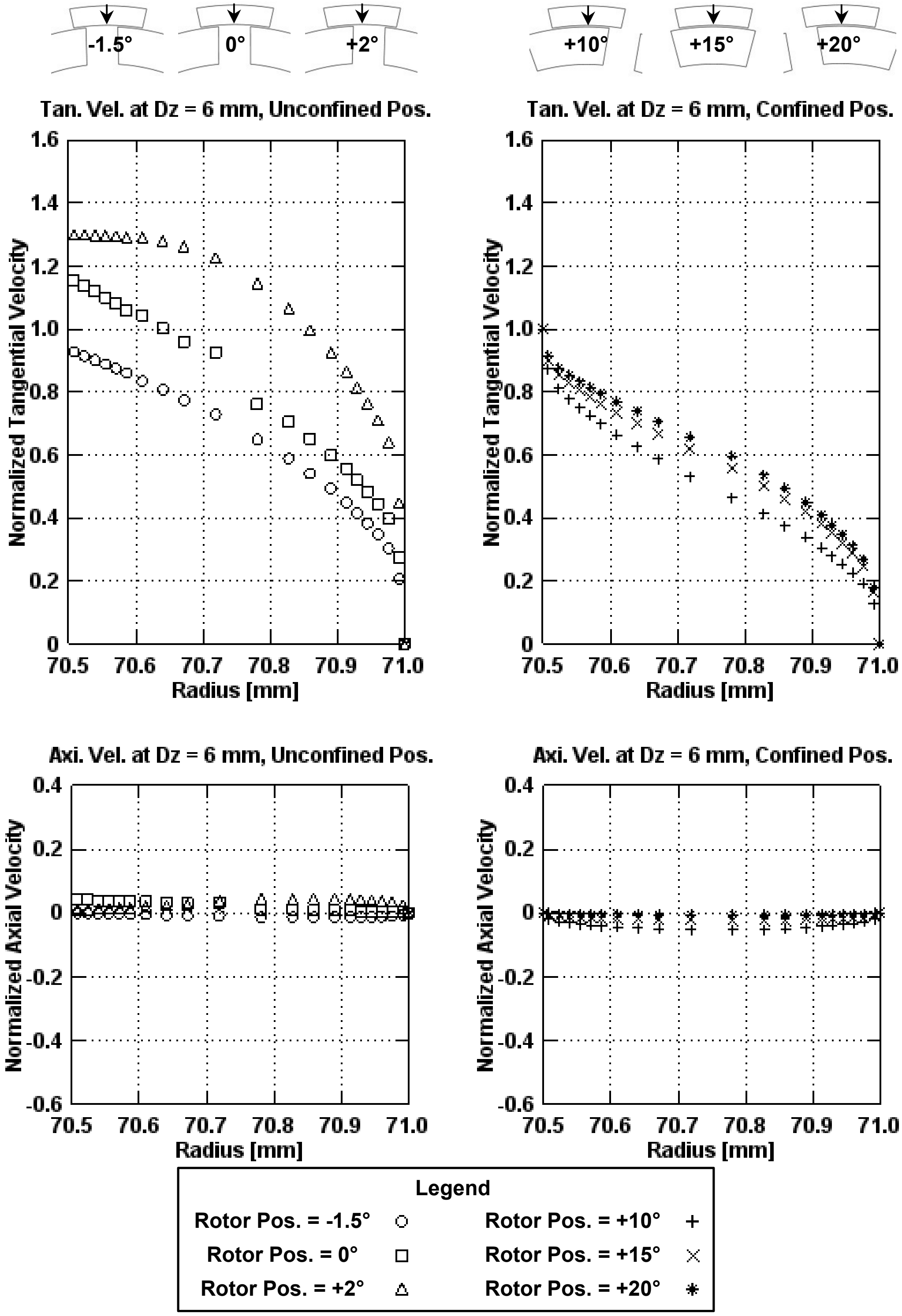

Figure B.2: Tangential and axial velocity profiles across shear gap at a depth of 6 mm for the low operating scenario (*N* = 300 rpm, *Q* = 0.315 L/s, Level 2 mesh).

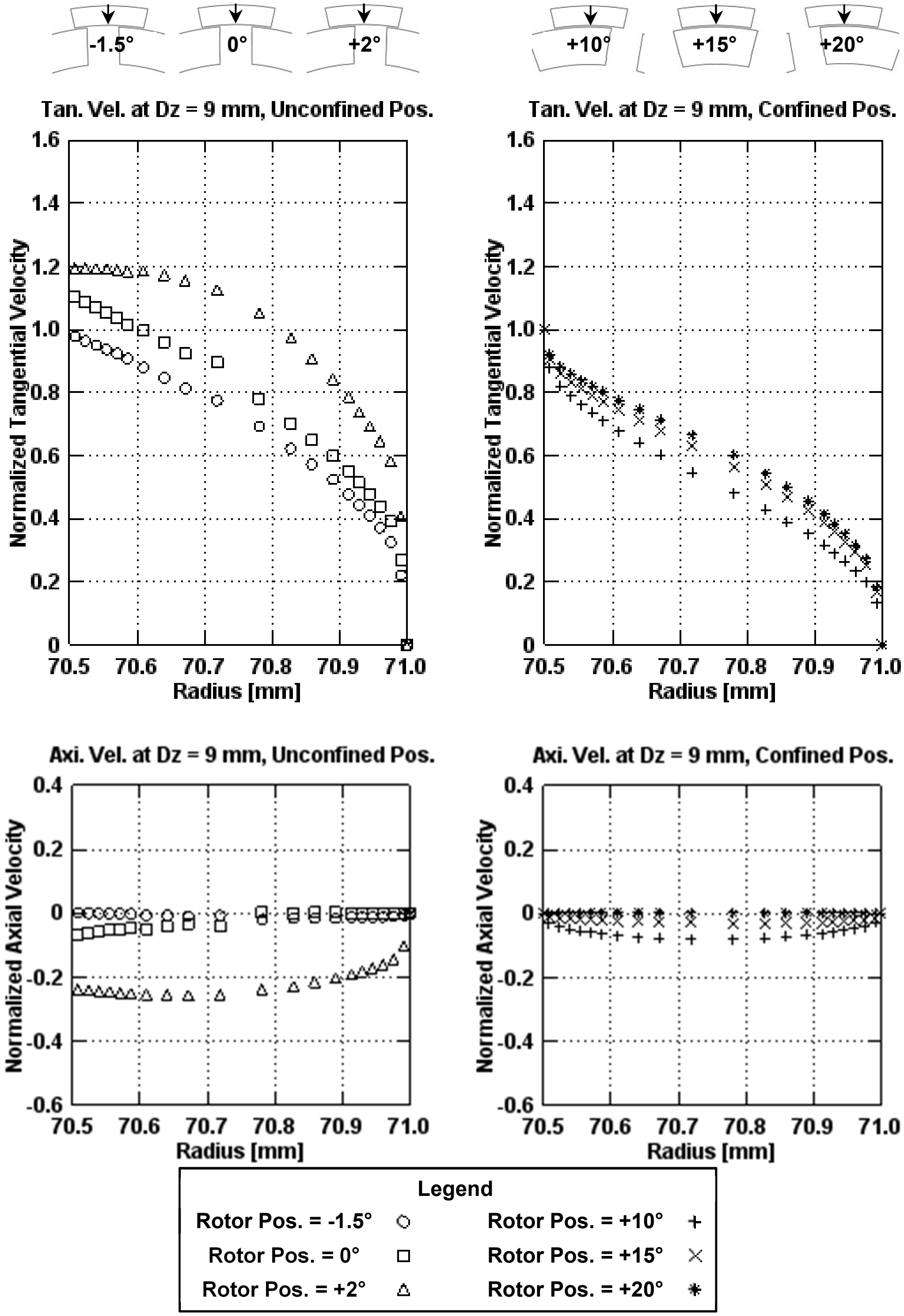

Figure B.3: Tangential and axial velocity profiles across shear gap at a depth of 9 mm for the low operating scenario ($N = 300$ rpm, $Q = 0.315$ L/s, Level 2 mesh).

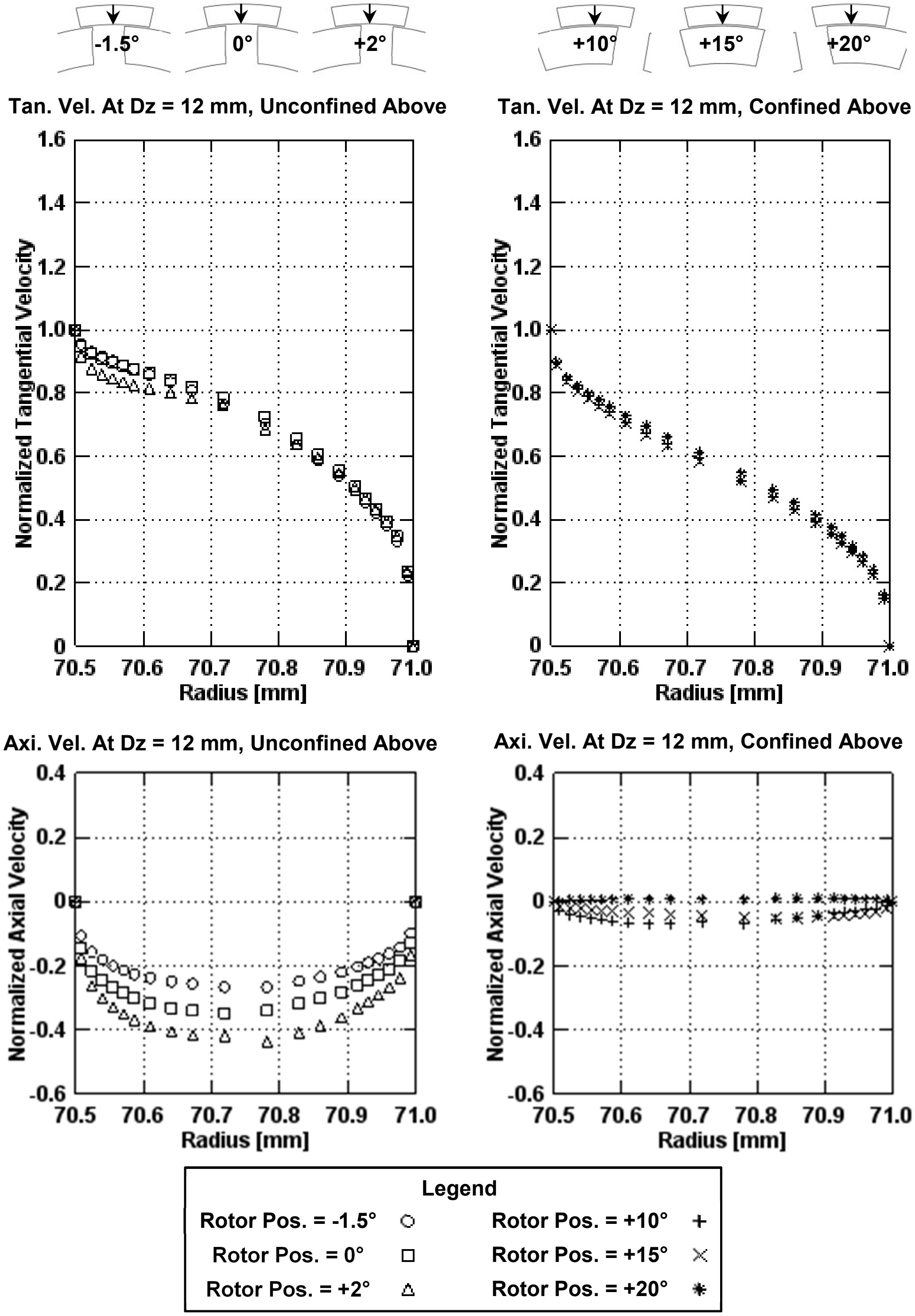

Figure B.4: Tangential and axial velocity profiles across shear gap at a depth of 12 mm for the low operating scenario (N = 300 rpm, Q = 0.315 L/s, Level 2 mesh).

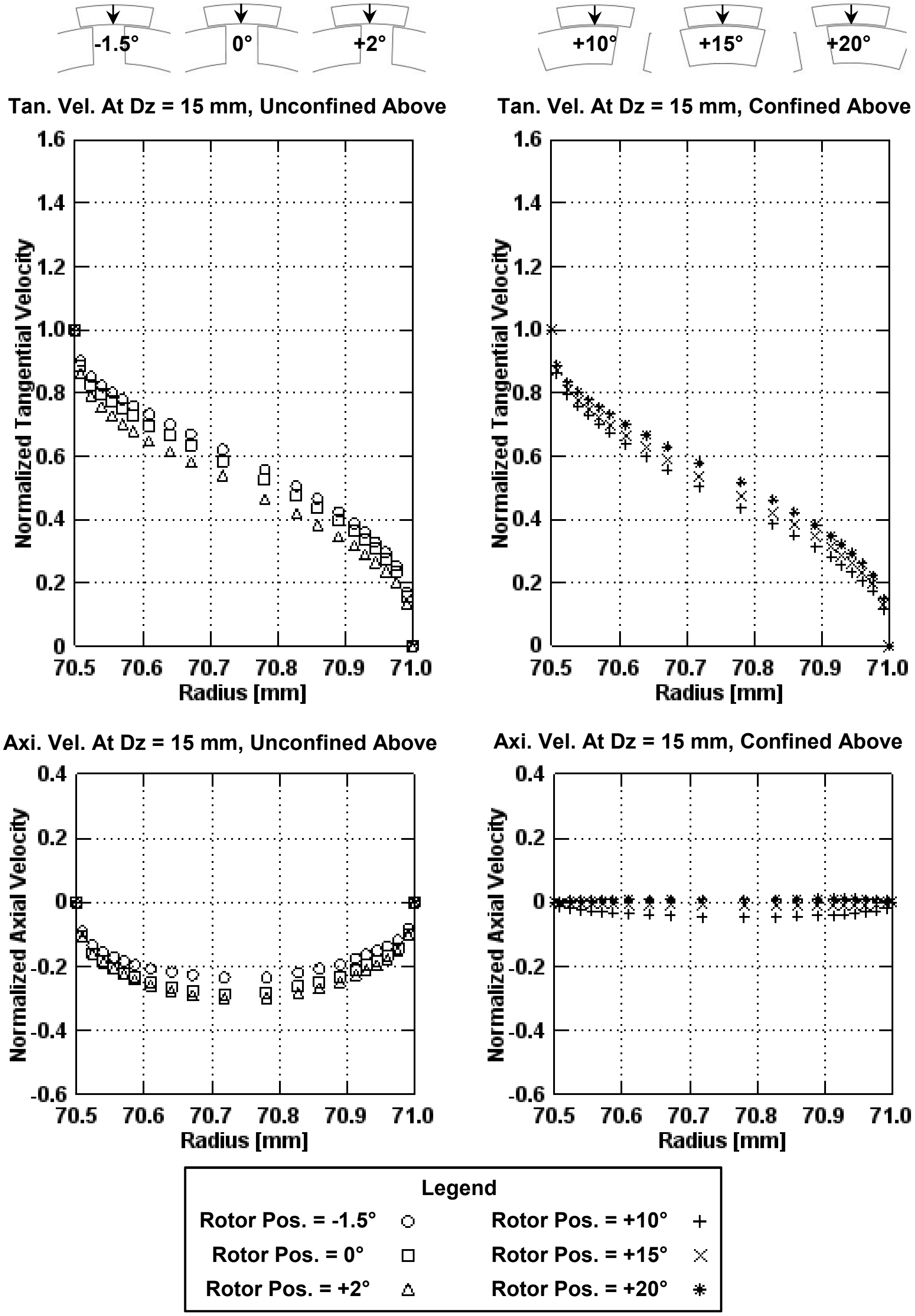

Figure B.5: Tangential and axial velocity profiles across shear gap at a depth of 15 mm for the low operating scenario ($N = 300$ rpm, $Q = 0.315$ L/s, Level 2 mesh).

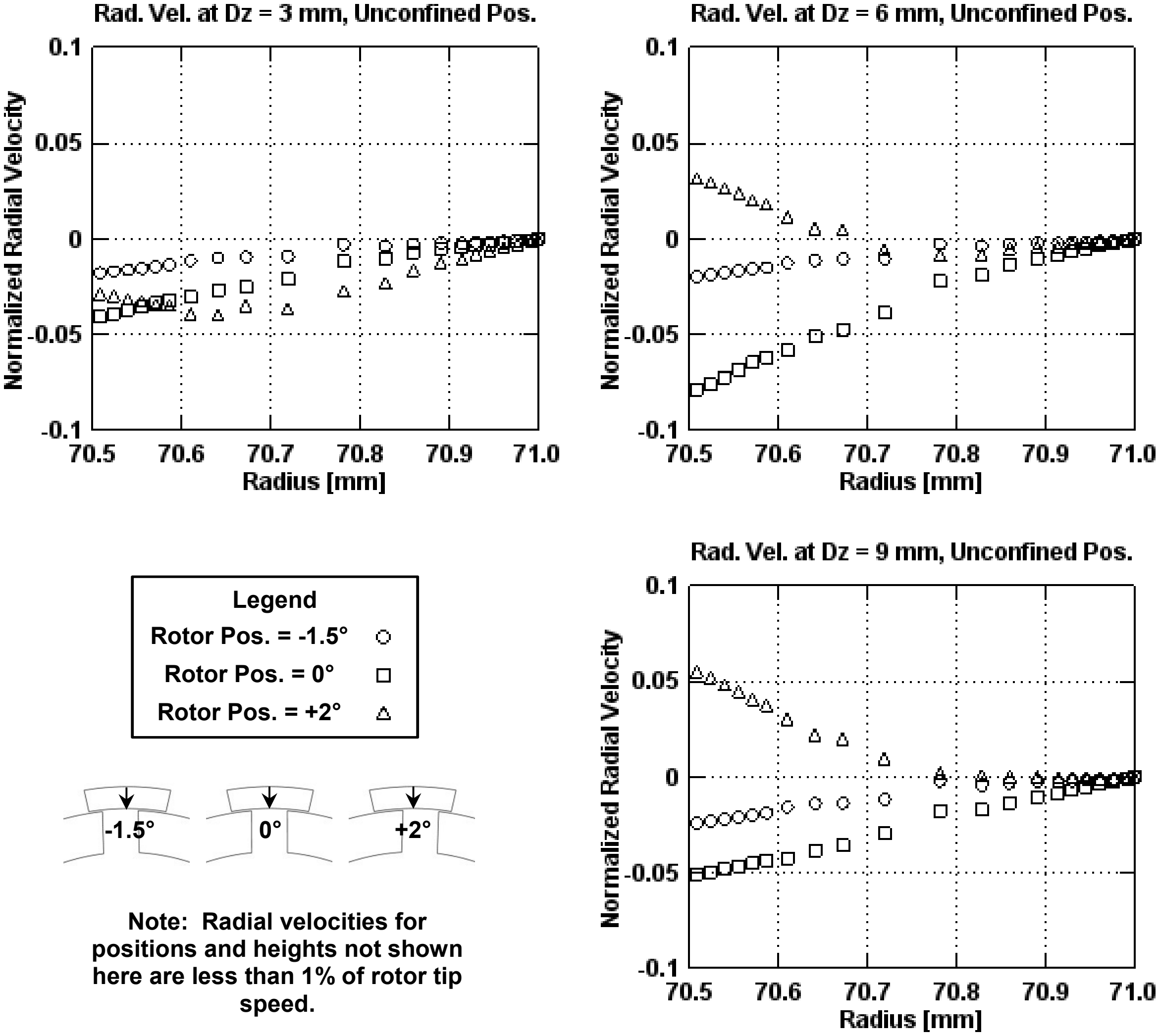

Rad. Vel. at Dz = 3 mm, Unconfined Pos.

Rad. Vel. at Dz = 6 mm, Unconfined Pos.

Rad. Vel. at Dz = 9 mm, Unconfined Pos.

Note: Radial velocities for positions and heights not shown here are less than 1% of rotor tip speed.

Figure B.6: Radial velocity profiles across shear gap at depths of 3, 6, and 9 mm for the low operating scenario (N = 300 rpm, Q = 0.315 L/s, Level 2 mesh).

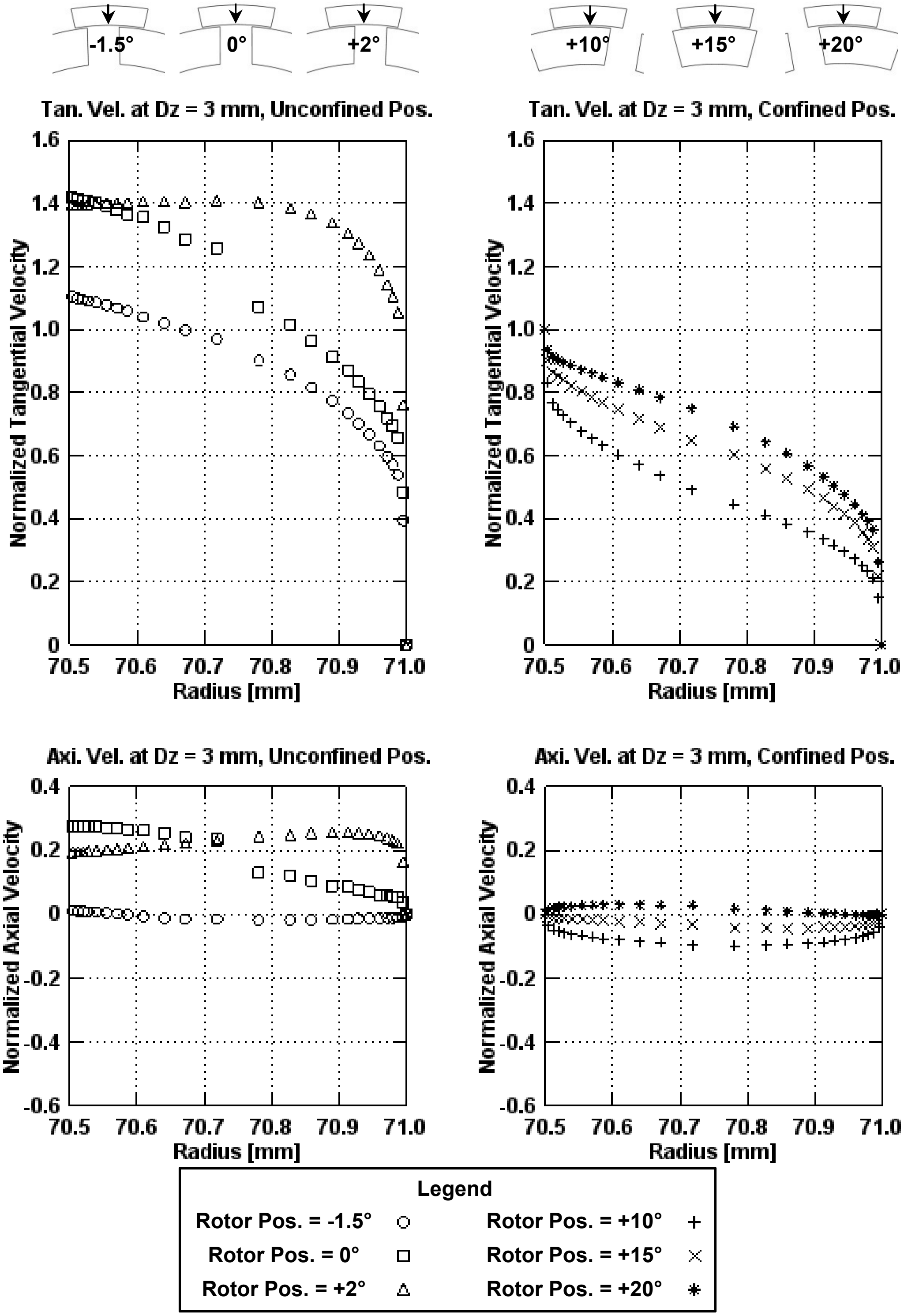

Figure B.7: Tangential and axial velocity profiles across shear gap at a depth of 3 mm for the high operating scenario (*N* = 1800 rpm, *Q* = 2.54 L/s, Level 3 mesh).

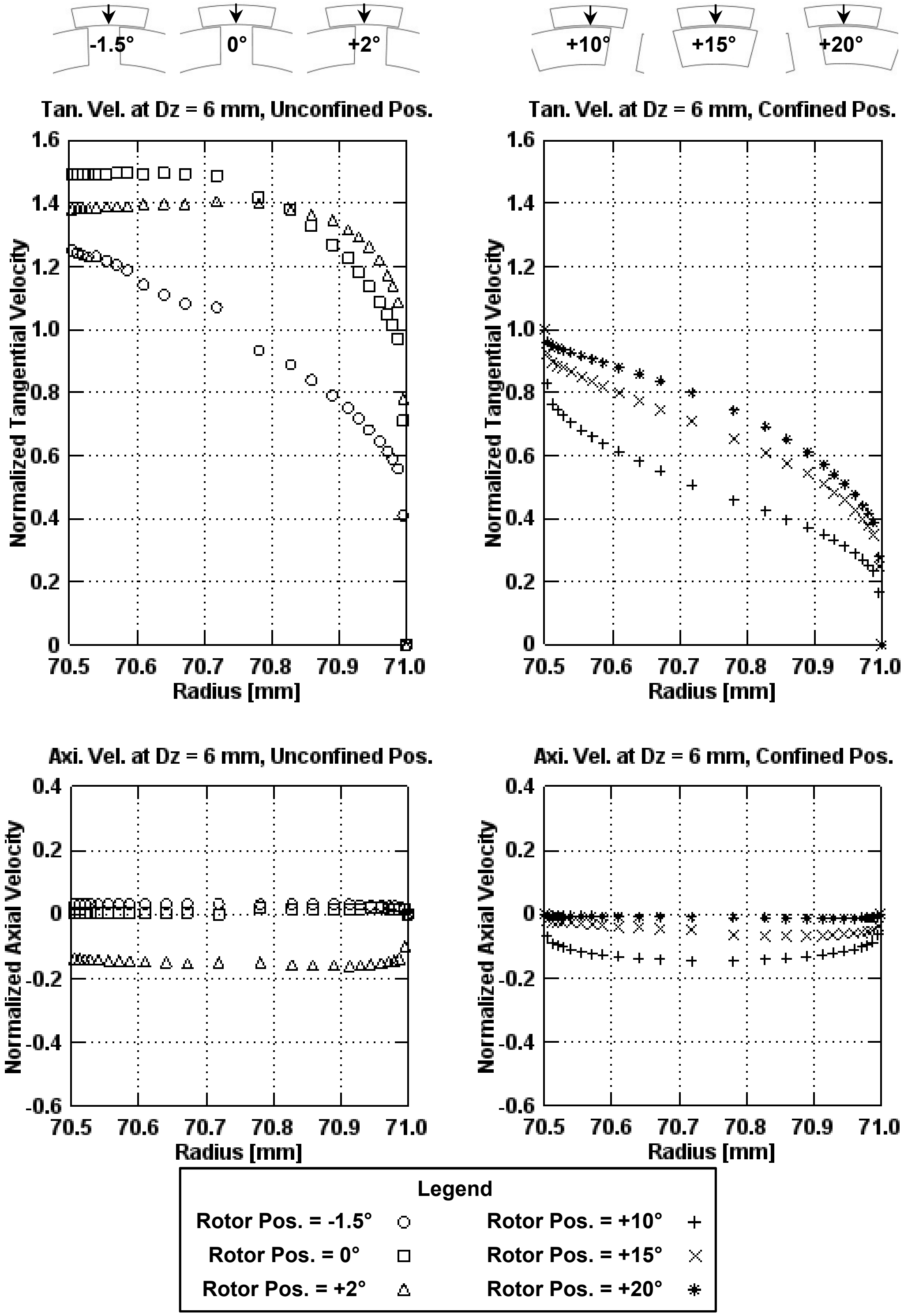

Figure B.8: Tangential and axial velocity profiles across shear gap at a depth of 6 mm for the high operating scenario ($N = 1800$ rpm, $Q = 2.54$ L/s, Level 3 mesh).

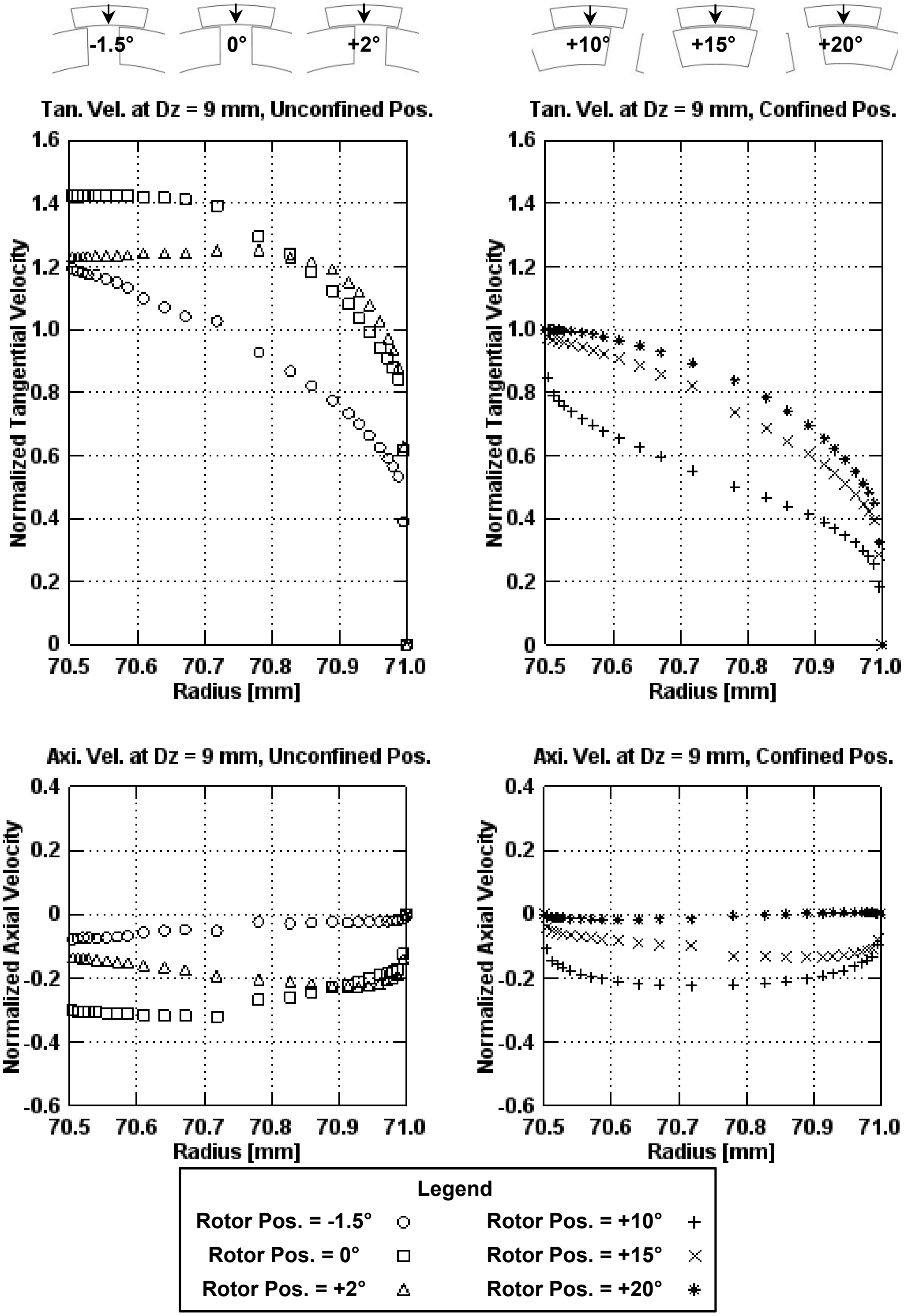

Figure B.9: Tangential and axial velocity profiles across shear gap at a depth of 9 mm for the high operating scenario (N = 1800 rpm, Q = 2.54 L/s, Level 3 mesh).

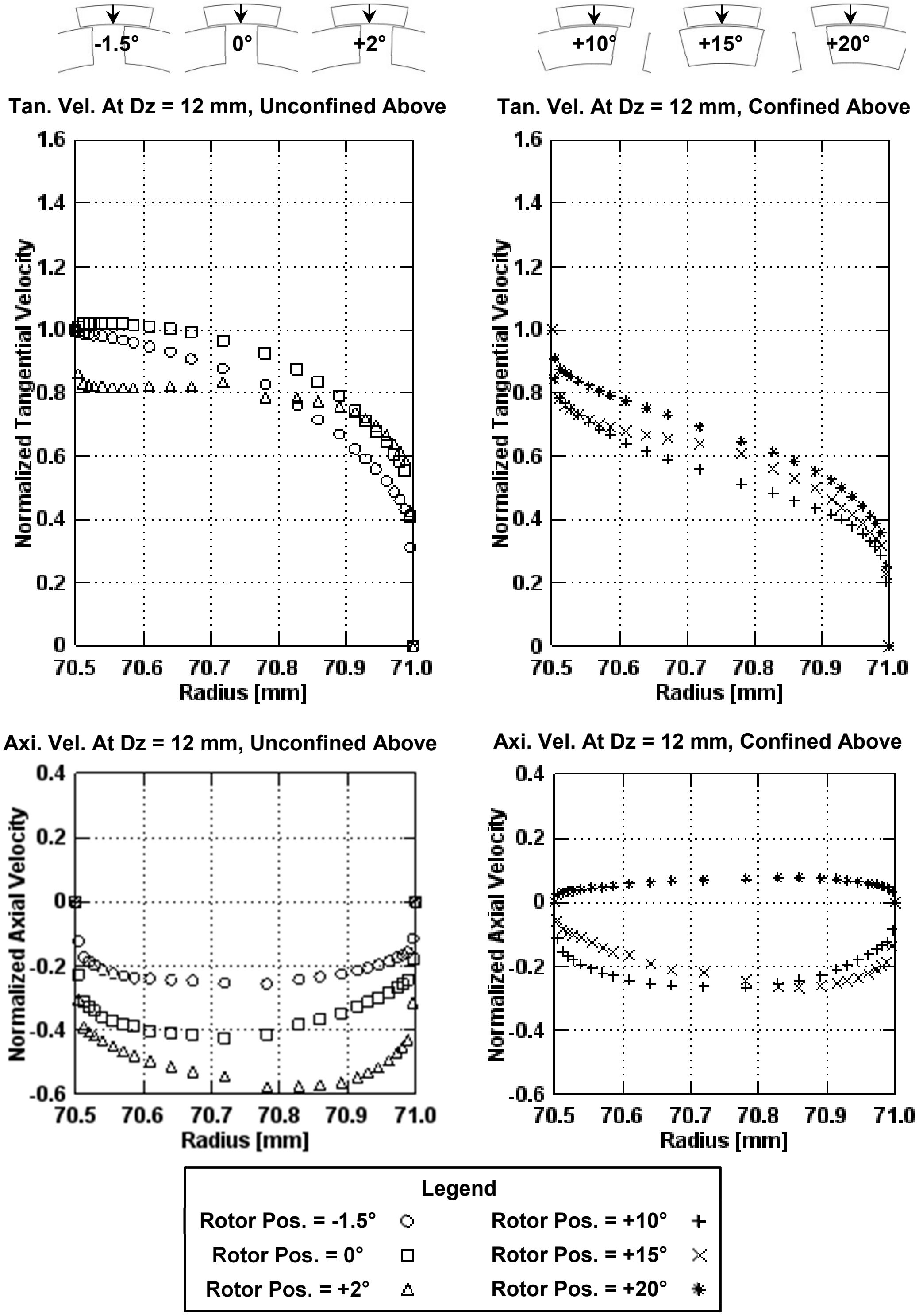

Figure B.10: Tangential and axial velocity profiles across shear gap at a depth of 12 mm for the high operating scenario ($N = 1800$ rpm, $Q = 2.54$ L/s, Level 3 mesh).

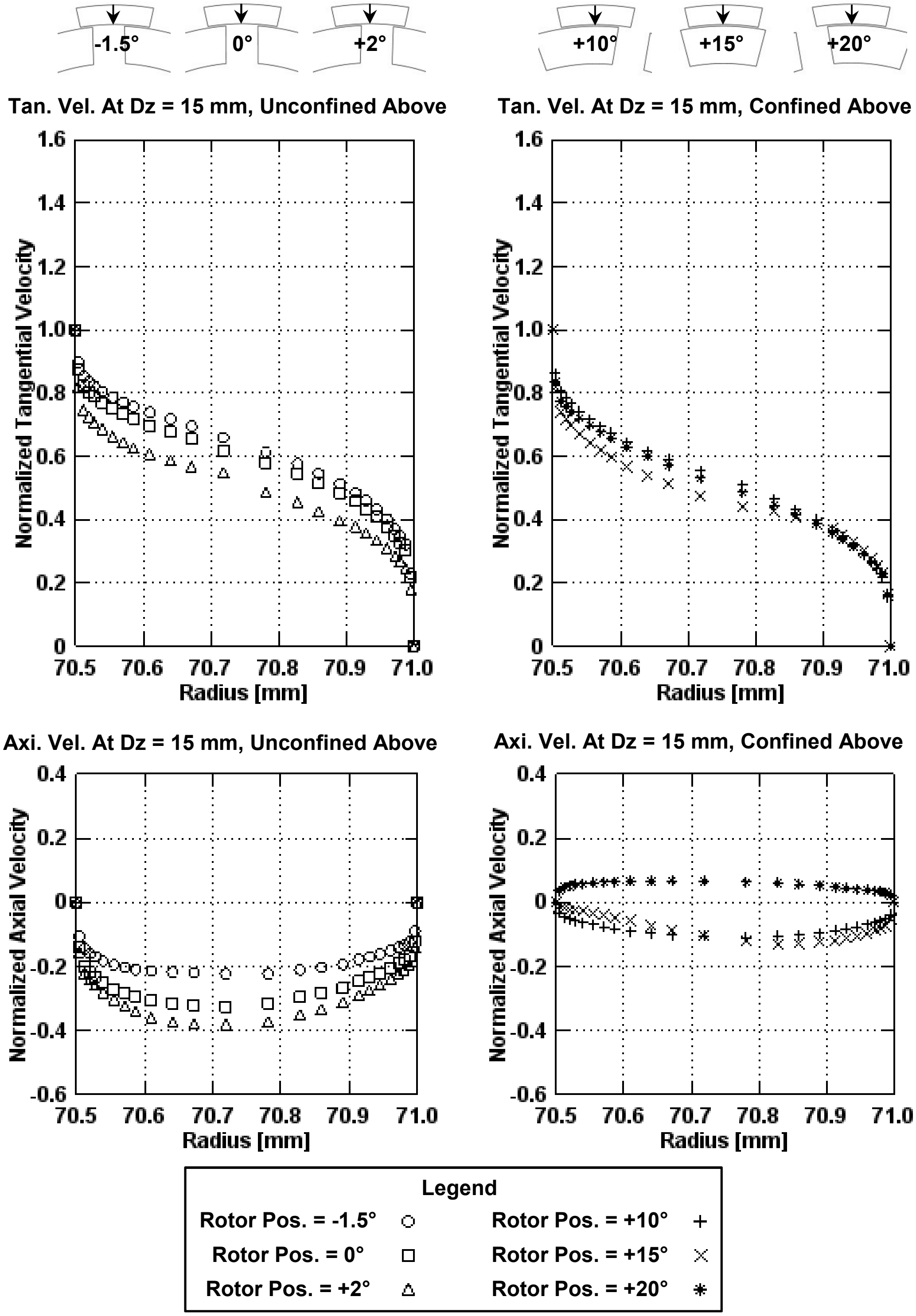

Figure B.11: Tangential and axial velocity profiles across shear gap at a depth of 15 mm for the high operating scenario (N = 1800 rpm, Q = 2.54 L/s, Level 3 mesh).

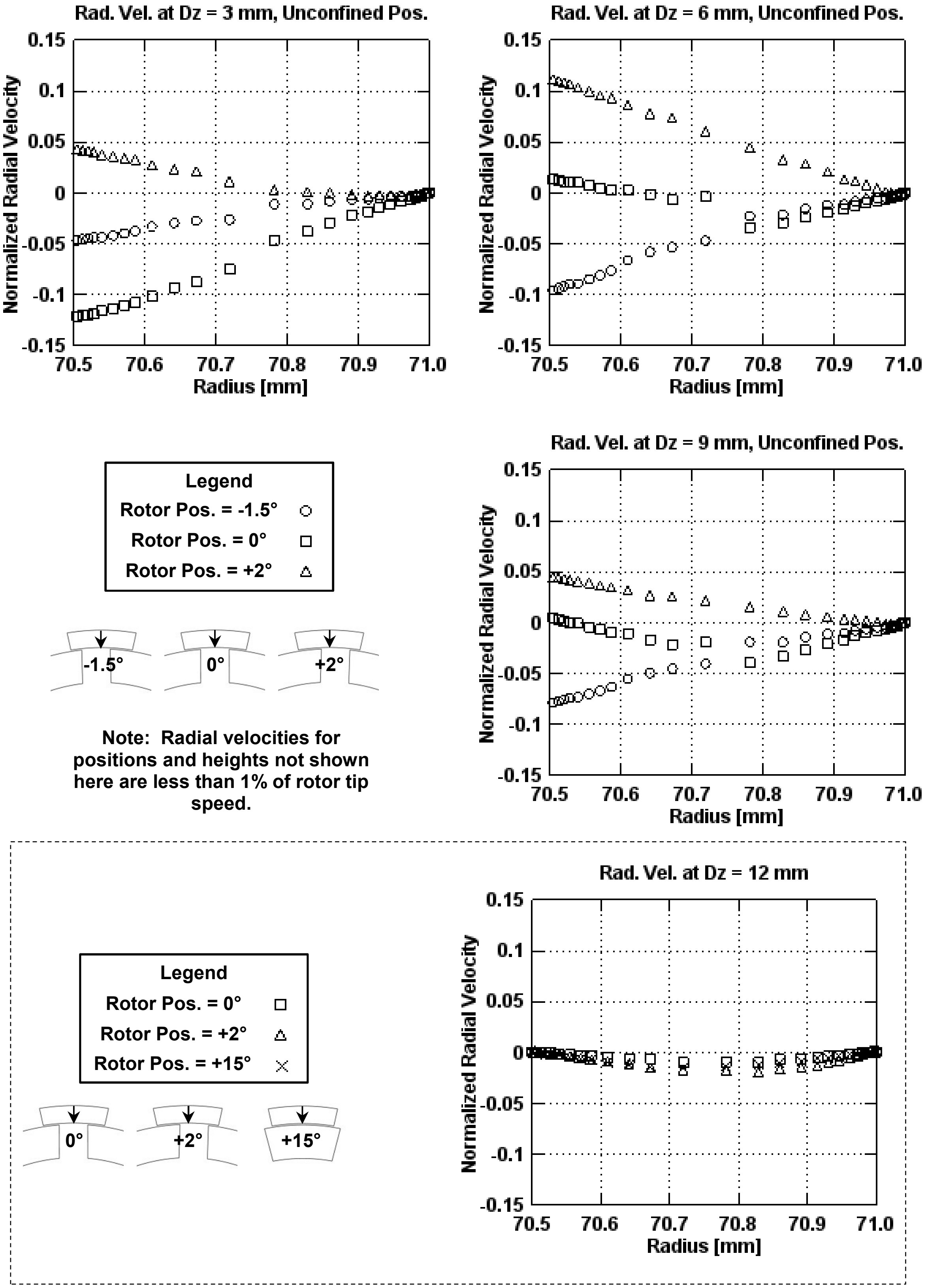

Note: Radial velocities for positions and heights not shown here are less than 1% of rotor tip speed.

Figure B.12: Radial velocity profiles across shear gap at depths of 3, 6, 9, and 12 mm for the high operating scenario ($N = 1800$ rpm, $Q = 2.54$ L/s, Level 3 mesh).

References

1. Atiemo-Obeng VA and Calabrese RV (2004). Rotor-Stator Mixing Devices. In EL Paul, VA Atiemo-Obeng, and SM Kresta (Eds.), Handbook of Industrial Mixing: Science and Practice (pp.). Hoboken, NJ: Wiley.

2. Bakker A, Laroche RD, Wang MH, and Calabrese RV (1997). Sliding Mesh Simulation of Laminar Flow in Stirred Reactors. *Chem Eng Res Des*, Vol. 75, pp. 42-44.

3. Barailler F, Heniche M, Tanguy PA (2006). CFD Analysis of a Rotor-Stator Mixer with Viscous Fluids. *Chem Eng Sci*, Vol. 61, pp. 2888-2894.

4. Doucet L, Ascanio G, Tanguy PA (2005). Hydrodynamics Characterization of Rotor-Stator Mixer with Viscous Fluids. *Chem Eng Res Des*, Vol. 83, pp. 1186-1195.

5. Hartmann H, Derksen JJ, Montavon C, Pearson J, Hamill IS, and van der Akker HEA (2004). Assessment of Large Eddy and RANS Stirred Tank Simulations by Means of LDA. *Chem Eng Sci*, Vol. 59, pp. 2419-2432.

6. Jaworski Z, Wyszynski ML, Moore IPT, and Nienow AW (1997). Sliding Mesh Computational Fluid Dynamics – A Predictive Tool in Stirred Tank Design. *P I Mech Eng E-J Pro*, vol. 211, pp. 149-156.

7. Kevala KR (2001). Sliding Mesh Simulation of a Wide and Narrow Gap Inline Rotor-Stator Mixer. M.S. Thesis, University of Maryland, College Park, MD.

8. Kevala KR (unpublished). Personal communication.

9. Kim SE and Choudhury D (1995). A Near-Wall Treatment Using Wall Functions Sensitized to Pressure Gradient. *ASME-FED Separated and Complex Flows*, Vol. 217, pp. 273-279.

10. Launder BE and Spalding DB (1974). The Numerical Computation of Turbulent Flows. *Comput Method Appl M*, Vol. 3, pp. 269-289.

11. Le Clair ML (1995). Optimize Rotor-Stator Performance Using Computational Fluid Dynamics. *PCI*, Vol. 11, pp. 46-48.

12. Murthy BN and Joshi JB (2008). Assessment of Standard k-ε, RSM and LES Turbulence Models in a Baffled Stirred Vessel Agitated by Various Impeller Designs. *Chem Eng Sci*, Vol 63, pp. 5468-5495.

13. Ng K, Fentiman NJ, Lee KC, and Yianneskis M (1998). Assessment of Sliding Mesh CFD Predictions and LDA Measurements of the Flow in a Tank Stirred by a Rushton Impeller. *Chem Eng Res Des*, Vol. 76, pp.737-747.

14. Pacek AW, Baker M, and Utomo AT (2007). Characterisation of Flow Pattern in a Rotor Stator High Shear Mixer. *Proc. 6th European Congress on Chemical Engineering*, Copenhagen, Denmark, Sept.

15. Patankar SV (1980). Numerical Heat Transfer and Fluid Flow. Hemisphere, Washington, DC.

16. Sheng J, Meng H, and Fox RO (1998). Validation of CFD Simulations of a Stirred Tank Using Particle Image Velocimetry Data. *Can J Chem Eng*, Vol. 76, pp. 611-625.

17. Utomo A, Baker M, and Pacek AW (2009). The Effect of Stator Geometry on the Flow Pattern and Energy Dissipation Rate in a Rotor-Stator Mixer. *Chem Eng Res Des*, Vol. 87, pp. 533-542.

18. Yang M (2011). CFD Simulations for Scale-up of Wet Milling in High Shear Mixers. Ph.D. Dissertation, University of Maryland, College Park, MD.